ELECTROLYTE NEGATIVE DIFFERENTIAL RESISTANCE, NANOPARTICLE DYNAMICS IN NANOPORES, AND NANOBUBBLE GENERATION AT NANOELECTRODES

by

Long Luo

A dissertation submitted to the faculty of
The University of Utah
in partial fulfillment of the requirements for the degree of

Doctor of Philosophy

Department of Chemistry

The University of Utah

May 2014

The University of Utah Graduate School

STATEMENT OF DISSERTATION APPROVAL

The dissertation of **Long Luo**

has been approved by the following supervisory committee members:

Henry S. White	, Chair	**Dec. 10, 2013** Date Approved
Cynthia J. Burrows	, Member	**Dec. 10, 2013** Date Approved
Joel M. Harris	, Member	**Dec. 10, 2013** Date Approved
Marc D. Porter	, Member	**Dec. 10, 2013** Date Approved
Rebecca M. Brannon	, Member	**Dec. 10, 2013** Date Approved

and by **Cynthia J. Burrows**, Chair/Dean of

the Department of **Chemistry**

and by David B. Kieda, Dean of The Graduate School.

ABSTRACT

This dissertation presents experimental and computational investigations of electrolyte negative differential resistance, nanoparticle dynamics in nanopores, and nanobubble formation at nanoelectrodes. Chapter 1 provides an introduction to negative differential resistance and other nonlinear electrical responses in nanopores, an overview of resistive pulse analysis of nanoparticles using nanopores, and current nanobubble research.

Chapter 2 describes the first example of electrolyte negative differential resistance (NDR) discovered in nanopores, where the current decreases as the voltage is increased. The NDR turn-on voltage was found to be tunable over a ~1 V window by adjusting the applied external pressure. Finite-element simulations yielded predictions of the NDR behavior that are in qualitative agreement with the experimental observations.

Chapter 3 presents the extension of NDR to an aqueous system and demonstrates the potential for chemical sensing based on NDR behavior. Solution pH and Ca^{2+} in the solution were separately employed as the stimulus to investigate the surface charge density dependence of the NDR behavior. The NDR turn-on voltage was found to be exceedingly sensitive to the nanopore surface charge density, suggesting possible analytical applications in detecting as few as several hundred of molecules.

Chapter 4 discusses the technique of controlling the dynamics of single 8 nm diameter gold nanoparticles in nanopores, which is extended from traditional resistive

pulse analysis of nanoparticles. A pressure was applied to balance electrokinetic forces acting on the charged Au nanoparticles as they translocate through a ~10 nm diameter orifice at an electric field. This force balance provides a means to vary the velocity of nanoparticles by three orders of magnitude. Finite-element simulations yielded predictions in semiquantitative agreement with the experimental results.

Chapter 5 reports the electrochemical generation of individual H_2 nanobubbles at Pt nanodisk electrodes immersed in a H_2SO_4 solution. A sudden drop in current associated with the transport-limited reduction of protons was observed in the *i-V* response at Pt nanodisk electrodes of radii less than 50 nm. Finite element simulation based on Fick's first law, combined with the Young-Laplace equation and Henry's Law, were employed to investigate the bubble formation and its stabilization mechanism.

TABLE OF CONTENTS

LIST OF ABBREVIATIONS

2D – two-dimensional

A.C. – alternating current

AFM – atomic force microscope

Ag/AgCl – silver/silver chloride

Au – gold

$CaCl_2$ – calcium chloride

D.C. – direct current

eq – equation

GNM – glass nanopore membrane

h – hour

H^+ – proton

H_2 – hydrogen

H_2SO_4 – sulfuric acid

i – current

ICR – ion current rectification

K_2HPO_4 – potassium phosphate dibasic

KH_2PO_4 – potassium phosphate monobasic

kHz – kilohertz

KCl – potassium chloride

M – moles per liter

mC – millicoulomb

mM – millimolar

mmHg – millimeter mercury

ms – millisecond

MΩ – megaohm

nA – nanoampere

NaCl – sodium chloride

NaCN – sodium cyanide

NDR – negative differential resistance

nm – nanometer

nM – nanomolar

O_2 – oxygen

pA – picoampere

pm – picometer

Pt – platinum

rms – root mean square

SEM – scanning electron microscope

TEM – transmission electron microscopy

V – voltage

μm – micrometer

μs – microsecond

LIST OF FIGURES

Figure Page

ACKNOWLEDGEMENTS

First of all, I would like to thank my PhD advisor, Dr. Henry S. White. He has been really helpful and supportive throughout my PhD study. His integrity, hard-working attitude, thoughtful guidance and extensive knowledge have been and will always be an inspiration to me. I also want to thank my committee members, Dr. Joel M. Harris, Dr. Marc D. Porter, Dr. Cynthia J. Burrows and Dr. Rebecca M. Brannon for their thoughtful suggestions. I feel grateful to the White group members and really enjoyed my stay with them during the past two and a half years. I will cherish the memories in my entire life.

I also want to thank my parents for their continuous love and encouragement. I deeply apologize for not being able to go back to China and visit them in the past three and a half years. And last but not least, I want to say thank you to my beloved fiancé, Yi-Ju Tsai. It is because of you that I never feel lonely when I am alone in this foreign country.

CHAPTER 1

INTRODUCTION

1.1 Negative differential resistance

Negative differential resistance (NDR) is a technologically important electrical phenomenon in which electrical current *decreases* as an applied voltage is increased. NDR behavior was first found in a semiconductor device, Esaki diode or tunnel diode, by Leo Esaki in 1958.[1] In 1973, Leo Esaki was awarded the Nobel Prize in Physics for this discovery. Figure 1.1a shows the NDR electrical response of a tunnel diode (highlighted in blue), recorded by an oscilloscope. A tunnel diode is a heavily doped p-n junction, and therefore, the conduction band of the n+ part overlaps with the valence band of p+ part in terms of energy. Under a voltage bias, the free electron in the conduction band of the n+ region can tunnel through the band gap to the valence band of the p+ region and conduct current, as shown in Figure 1.1b. As the voltage bias is further increased, the energy level of the conduction band of the n+ region becomes higher, resulting in fewer electrons on the n+ side having the same energy as the hole states in the valence band of the p+ region. Under these conditions, the tunneling current starts decreasing and NDR occurs.

NDR in nanopores exhibits a similar electrical response as tunnel diode, but the mechanism is completely different. The discovery of NDR response in nanopores

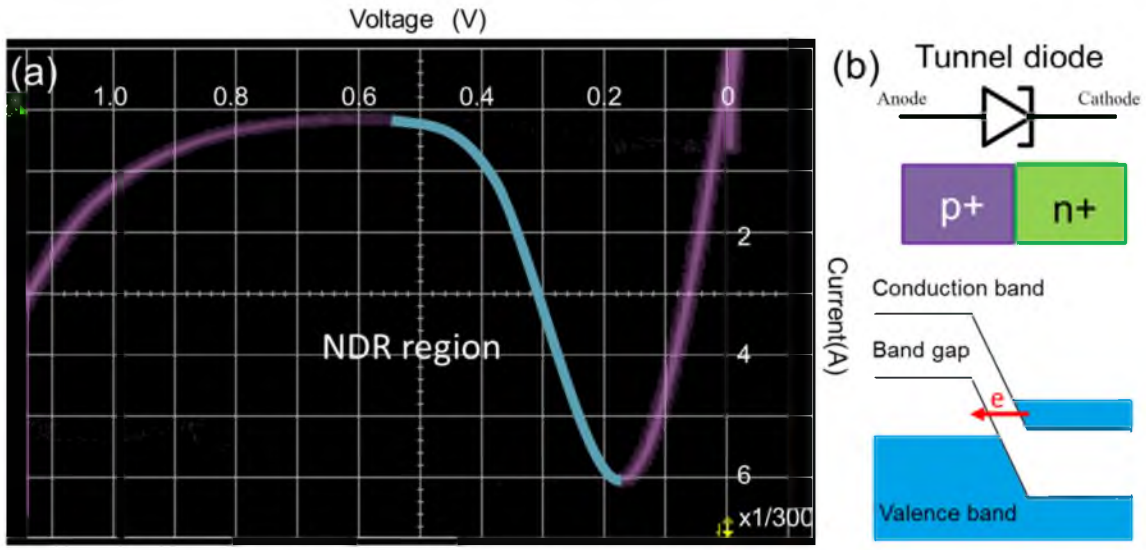

Figure 1.1. (a) *i-V* response of an Esaki diode or tunnel diode recorded by an oscilloscope. The negative differential resistance (NDR) region is highlighted in blue. (b) Schematic symbol of a tunnel diode. Tunnel diodes are heavily doped p-n junctions. The heavy doping results in a broken band gap, in which the conduction band of the n+ part aligns with the valence band of the p+ part. A small voltage bias can drive the electrons on the n+ part to tunnel through the band gap to the p+ part. A further increased voltage bias elevates the energy level of the conduction band of n+ part, and therefore, fewer electrons in the conduction band on the n+ part can tunnel to the hole states on the p+ part due to the energy mismatch.

originates from the study of another widely investigated nonlinear electrical response in nanopores, *i.e.*, ion current rectification (ICR).

ICR is defined as the experimental departure of the current-voltage (*i-V*) responses of nanopores or nanochannels from the linear ohmic behavior, *i.e.*, the magnitude of the current flowing through a nanopore between two electrodes at negative potentials is greater or smaller than the current at the same positive potentials.[2] The blue line in Figure 1.2 schematically illustrates a typical ICR response. In 1997, Wei, Bard, and Feldberg first discovered ICR in quartz conical-shaped nanopipets.[3] They demonstrated that the ICR behavior depends on the size of the nanopipet orifice and the ionic strength of the solution in contact with the conical-shaped nanopipets. Since then, there has been great interest in exploring ICRs in different nanopores.[4-8] Martin and co-workers reported in 2004 that ICR relies primarily on the surface characteristics of the inner walls of the nanopore.[9] For example, conical Au nanotubes modified with chemisorbed thiol mercapto-propionic acid exhibit ICR in a 0.1 M KF solution. They observed rectification at pH = 6.6 where the –COOH group is deprotonated to yield negative surface charge; at pH = 3.5, the surface charge is removed and rectification is eliminated. Similarly, adding positive surface charge to the nanotubes leads to rectifiers with polarity opposite that of the anionic nanotubes.

It has been generally accepted that rectification behavior is strongly related to the pore size, pore surface properties, and the ionic strength of the bulk solution. For a glass conical nanopore, the surface is negatively charged at neutral pH due to the dissociation of the surface silanol groups. The electric field associated with the charged surface extends to a distance of $\sim 5\kappa^{-1}$,

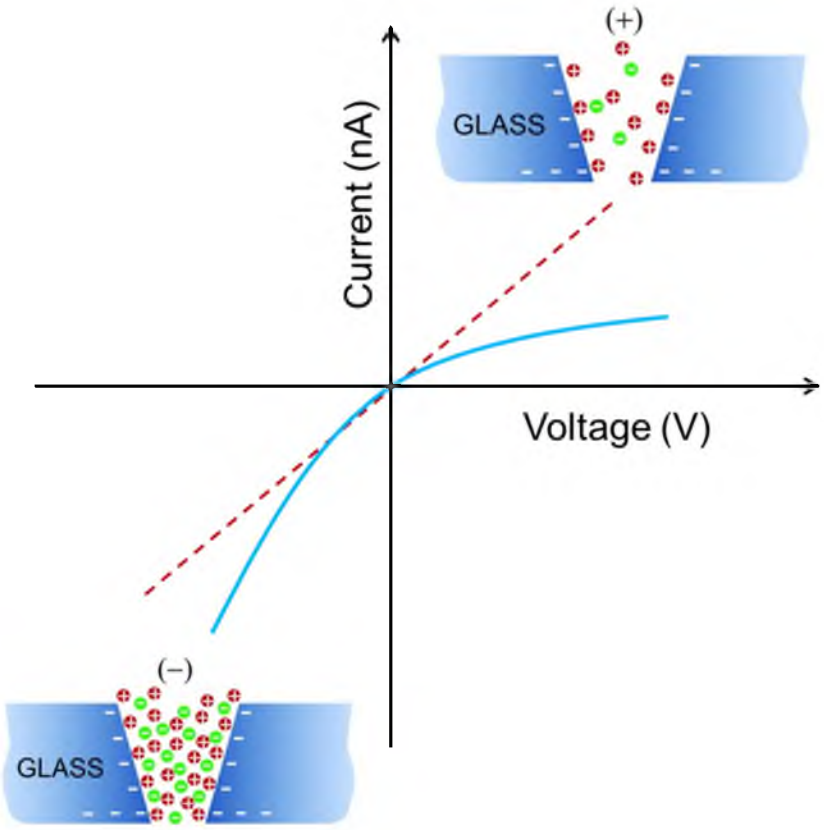

Figure 1.2. Schematic representation of ion current rectification in conical-shaped glass nanopores.

$$\kappa^{-1} = \sqrt{\frac{\varepsilon_r \varepsilon_0 RT}{2z^2 F^2 c}} \tag{1.1}$$

where κ^{-1} is the Debye screening length, ε_r is the relative permittivity, ε_0 is the permittivity in a vacuum, R is the gas constant, T is the absolute temperature, z is the electrolyte valence, F is the Faraday constant, and c is the electrolyte concentration.[10] The Debye length is ~3 and 0.3 nm for a 0.01 M and a 1 M KCl solution, respectively.

Qualitatively, when the orifice size of a conical-shaped pore approaches nanometer scale and is of the order of magnitude of $5\kappa^{-1}$, the electric field produced by the surface charge covers a great fraction of the orifice and the volume of solution in the pore orifice becomes cation selective due to the electrostatic attraction and repulsion. As a negative potential (we define all potentials and pressures reported hereinafter as values in the pore interior relative to those in the external solution) is applied across the membrane, the potassium ion (K^+) flux is directed from external solution to the pore interior, while the chloride ions (Cl^-) move in the opposite direction. A consequence of the cation selectivity at the pore orifice is that Cl^- ions are rejected by the glass surface, resulting in an accumulation of Cl^- within the pore interior, and a greater conductivity inside the pore orifice than the bulk KCl solution, as shown in Figure 1.2. As the negative potential is increased, a higher Cl^- concentration and conductivity will be present and an increased conductivity will be achieved. Because the conical nanopore is characterized by the localized mass transfer resistance in the vicinity of the portion of the pore that is immediately adjacent to the pore orifice (the sensing zone),[11] the greater conductivity in the sensing zone results in a higher overall conductivity of the nanopore, reflected as an increase in the slope of the *i-V* curves. Conversely, when a positive potential is applied,

the transport of Cl^- from the external solution to the pore interior is repelled by the surface charges and Cl^- is depleted within the pore. This depletion decreases the nanopore conductivity and the experimentally measured ion current, represented as a decrease in the slope of the *i-V* curves. Different conductivities at positive and negative voltages results in a departure from the linear ohmic behavior, or ion current rectification (ICR). White and coworkers verified this mechanism using finite element simulations which involved solving the coupled Nernst-Planck, Poisson's, and Navier-Stokes equations in a simplified 2D axial symmetric system (cylindrical coordinate) that represents the actual 3D geometry of a conical-shaped nanopore.[12]

In a recent article, Yusko and Mayer reported a new method to generate the ICR response in borosilicate glass nano- and micropores.[13] In their experiment, two solutions with different conductivities were placed inside and outside a nano-/micropore, as illustrated in Figure 1.3b and c. At positive voltages, a voltage-induced electro-osmosis flow (EOF, red arrows in Figure 1.3b) in a nanopore is generated to push the internal high-conductive solution (KCl aqueous solution) out of the sensing zone. The EOF is caused by the electromigration of counter ions (cations) accumulating near the negatively charged glass surface in an electric field, which drags the solution through momentum transfer. At negative voltages, conversely, an oppositely-directed EOF (red arrows in Figure 1.3c) is generated to pull the external low-conductive solution (KCl in DMSO/water mixture) into the sensing zone. As a result, an ICR response was achieved (Figure 1.3a) due to different conductivities of the solutions occupying the sensing zone at positive and negative voltages. Following a similar route, Jiang and coworkers[14] produced ICR response in nanopores by placing two KCl solutions with different

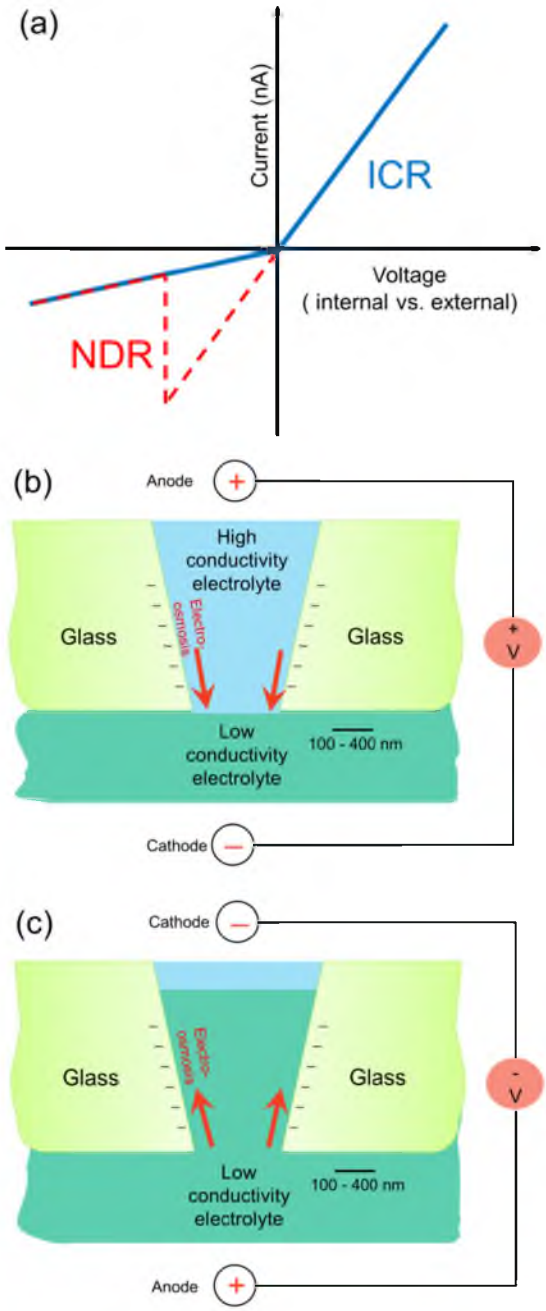

Figure 1.3. (a) Ion current rectification (ICR, blue line) and negative differential resistance (NDR, red dash line). (b) and (c) Schematic representation of ion current rectification in a conical glass nanopore. At a positive voltage (internal *vs.* external), the nanopore is occupied by high-conductive solution due to the electro-osmosis (red arrows) pushing the internal solution outwards. Conversely, at a negative voltage, low-conductive solution fills the nanopore, resulting from an oppositely directed electro-osmosis.

concentrations inside and outside a nanopore. This type of ICR response can also be regarded as the transition between two conductive states at zero volts (high-conductive state at positive voltages and low-conductive state at negative voltages). The shift of this transition voltage to a negative value results in an NDR response (red dash line in Figure 1.3a), due to the need to return to the low conductivity state at more negative voltages. Chapter 2 and 3 describe how to achieve this shift in transition voltage and discuss the numerical models used to qualitatively capture the mechanism of NDR behaviors in nanopores.

The highly nonlinear *i-V* characteristics of ICR and its strong dependence on surface properties have inspired researchers to construct biosensors by tuning the local surface charge at the pore orifice *via* binding of analytes. Martin *et al.* first demonstrated a highly sensitive and selective protein biosensor based on the permanent blockage of the ionic current through biofunctionalized conical Au nanotubes.[15] The Siwy group then described a new type of biosensing system for avidin, streptavidin, and the capsular polypeptide from *Bacillus anthracis*, by monitoring the rectification ratio (defined as currents at voltages of one polarity over currents at voltages of the opposite polarity) for the detection of an analyte.[16] Ali and co-workers described another sensing paradigm of ICR in a nanochannel contained in an ion-tracked polymer membrane.[17] The inner walls of the channel are decorated with horseradish peroxidase (HRP) enzyme using carbodiimide coupling chemistry for repeatedly detecting nanomolar concentrations of hydrogen peroxide (H_2O_2) with 2, 20-azino-bis (3-ethylbenzothiazoline-6-sulfonate) (ABTS) as the substrate. Azzaroni and Ali also reported a pH-dependent ICR by integrating polymer brushes into single conical nanochannels.[18] A layer-by-layer assem-

bly technique was developed by the same group to deposit multilayered films of poly (allylamine hydrochloride) (PAH) and poly (styrenesulfonate) (PSS) on the pore surface.[19] The nanopores can then be switched reversibly between different rectifying states. In another report, Wang and Jiang attempted to attach a pH-sensitive DNA molecular motor to a synthetic poly (ethylene terephthalate) (PET) nanopore, bestowing nanopores with various pH-determined conductive states.[20] Jiang and Zhu also built a biomimetic asymmetric responsive single nanochannel system in which the ICR is both pH- and temperature-sensitive.[21]

Based on the mechanism study, we found that NDR in nanopores was also extremely sensitive to the surface properties of nanopores. Inspired by these studies on ICR based sensing, we demonstrate the sensing applications of NDR in nanopores in this dissertation. Instead of the rectification ratio in current, the shift in the transition voltage where the NDR occurs becomes the indicator of the change of nanopore surface properties and analytes in solution.

1.2 Resistive pulse analysis of nanoparticles

The resistive pulse counter, also called the Coulter counter, was invented by Dr. Wallace Coulter in 1953 to analyze micrometer size objects such as bacteria, cells, and clay particles [22] and has been extensively applied in biomedical applications and fundamental science, such as measuring the dissolution rate of air bubbles.[23] A traditional Coulter counter contains two compartments separated by a 20 μm to 2 mm diameter aperture. Particles in the solution are driven through the aperture by a voltage bias or pressure gradient. Two Ag/AgCl electrodes on either side of the aperture continuously

record ion current changes during the particle translocation. A single resistive pulse (a drop in current) is generated due to the replacement of conductive electrolyte solution by a transolcating nonconductive solid particle. The frequency, width and height of these pulses provide insight into the particle size distribution, concentration, shape, and surface charge properties. The development of nanopore fabrication techniques during the past ten years has enabled a resurgence of the Coulter counter paradigm as an alternate way to quickly analyze individual nanoparticles. Solid-state[24-35] and biological[36-38] nanopores with diameters ranging from several hundred to a few nanometers have been developed, enabling scientists to count particles in a similar size range, and to analyze the structure of biopolymers, *e.g.*, DNA.[37]

In the 1970s, DeBlois *et al.*[39-41] reported, for the first time, the extension of Coulter counting to nanoparticles, including viruses about 60 nm in diameter and polystyrene spheres 90 nm in diameter using individual submicron pores etched in plastic sheets. Recently, the Crooks group[26,42-44] reported the application of Si_3N_4 and PDMS membranes containing an individual multiwalled carbon nanotube (~130 nm diameter) as a nano-Coulter counter. Their experimental setup is schematically shown in Figure 1.4a. Negatively charged nanoparticles were driven through the carbon nanotube by a voltage bias (E_M) while the ion current was continuously recorded. Figure 1.4b to d show current-time traces at different E_M between the two Ag/AgCl electrodes. Each pulse, or current drop, represents a single particle translocation through the nanochannel. The magnitude of one pulse, Δi_c, can be related to particle size, the pulse duration, Δt, can be used to determine the charge carried by the particle, and the pulse frequency provides information about the concentration of particles in solution. This experiment clearly

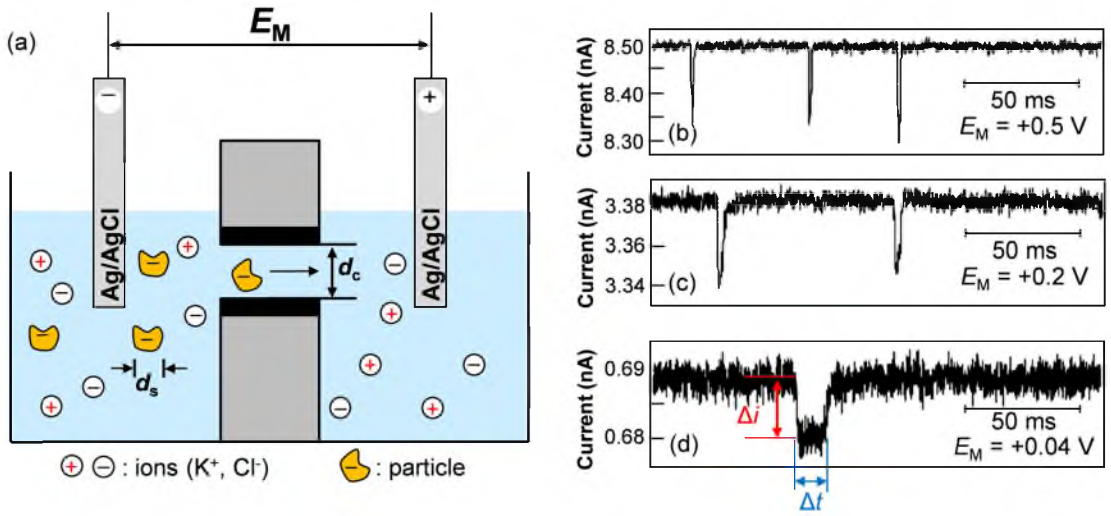

Figure 1.4. (a) Schematic illustration of electric field-driven resistive pulse analysis of nanoparticles. A voltage bias (E_M) is applied across the membrane containing a single carbon nanotube channel, driving ions and charged particles through the nanopore. (b)-(d) show the typical current-time traces at different E_M. Each pulse or decrease of current represents a single nanoparticle translocation. Particle size and surface charge are calculated based on the duration time Δt and pulse height Δi. Reprinted with permission from Reference 26 Ito, T.; Sun, L.; Henriquez, R. R.; Crooks, R. M. *Acc. Chem. Res.* **2004,** *37*, 937-945. Copyright, 2004 American Chemical Society.

identified the potential value of Coulter counting in modern analysis, and led to a resurgence of interest in the resistive pulse analysis of nanoparticles.

The replacement of electrolyte solution within the channel by a nanoparticle causes an increase of solution resistance, ΔR, and therefore a decrease in current, Δi. This process is completely reversible, so when the particle exits the channel the current level recovers to the baseline level, $i_o = E_M / R_o$, where R_o is the constant open channel solution resistance. With and without a nanoparticle in the channel, the solution resistance can be always calculated by eq 1.2 using different geometry factors, S(x).

$$R = \int_0^{l_c} \frac{\kappa}{S} dx + R_{end} \tag{1.2}$$

where κ is the solution conductivity and R_{end} is the spreading resistance at the ends of a nanochannel due to the partially blocked mass transport.[45] κ is generally assumed to be constant in the nanochannel, although there are exceptions when the width of the channel or the diameter of the pore approaches the length scale of the electrical double layer.

The ratio of current change during the translocation $\Delta i / i_o$ is equal to the ratio of resistance change $\Delta R / R_o$. As a result, $\Delta i / i_o$ is a function of the shape of nanoparticles (*e.g.*, the diameter d_s of a nanosphere) and the topology of the corresponding nanochannel (*e.g.*, the diameter d_c and length l_c of a nanocylinder). For example, $\Delta i / i_o$ for a nanosphere translocating through a nanocylinder, derived by DeBlois,[39] is

$$\frac{\Delta i}{i_o} = S(d_c, d_s)\frac{d_s^3}{(l_c + 0.8d_c)} \tag{1.3}$$

where $S(d_c, d_s)$ is a correction factor that depends on the nanoparticle to nanochannel diameter ratio, d_s/d_c. When $d_s / d_c < 0.8$, $S(d_c, d_s)$ is ~1 (± 2%).[26a] Similar expressions of $\Delta i / i_o$ were derived for conical nanopores[46-48] and short cylindrical nanopores (where, $l_c \leq d_s$).[49] Nanoparticle size d_s is then calculated based on experimentally measured $\Delta i / i_o$ using eq 1.3.

The duration time, Δt, is inversely proportional to the average translocation velocity, v. In the absence of particle/channel interactions, there are three types of external driving forces contributing to v: electrophoretic forces (EPF), electro-osmotic forces (EOF) and applied pressure. Figure 1.5 schematically illustrates these three forces exerted on a negatively charged 8 nm nanoparticle when a positive voltage and negative pressure are applied (inside *vs.* outside the nanopore). The EPF stems from the influence of the external electric field on a charged particle while the EOF arises from the transport of the counterions in the electrical double layer of the nanopore wall that drags water with them through viscous interactions.[50] Researchers usually isolate the electrophoretic velocity component experimentally and mathematically from the other two. Then, the nanoparticle surface charge is estimated from the electrophoretic velocity, $v_{electrophoresis}$, in terms of its zeta potential, ζ, using the Helmholtz-Smoluchowski equation,

$$\mu_e = A\frac{\varepsilon_r \varepsilon_o \zeta}{\eta} = \frac{v_{electrophoresis}}{E} \tag{1.4}$$

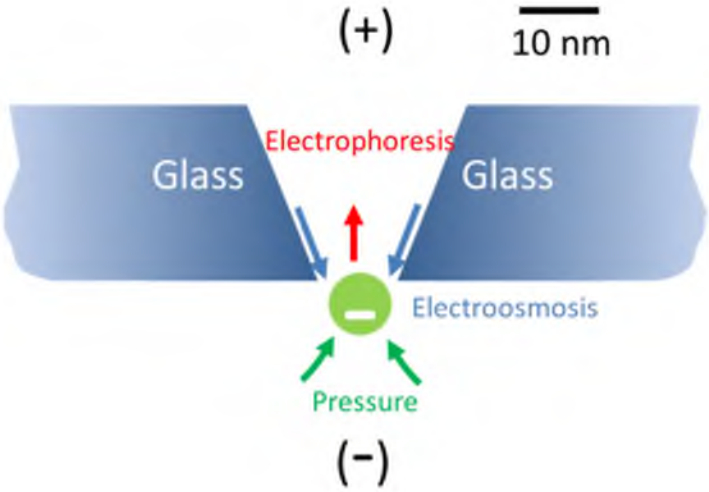

Figure 1.5. A schematic drawing of the driving forces acting on a negatively charged 8-nm-diameter nanoparticle as the nanoparticle translocates through a conical-glass nanopore at a positive voltage and negative pressure. The sign is defined by the difference between internal and external potentials or pressures.

where μ_e is the nanoparticle electrophoretic mobility, E is the electric field gradient, ε_r is the solution dielectric constant, η is the solution viscosity, ε_o is the vacuum permittivity, and A is a correction factor which depends upon the ratio of the particle diameter, d_s, and the Debye length, κ^{-1} (when $d_s / \kappa^{-1} >> 1$, $A = 1$; when $d_s / \kappa^{-1} << 1$, $A = 2/3$).

Previous studies on the resistive pulse analysis of nanoparticles indicate that these three external driving forces (EPF, EOF and pressure) are of similar order of magnitude. Most recently, Lan *et al.*[51] demonstrated that fine control of a single nanoparticle translocation direction and speed is possible by adjusting the applied pressure in an electric field. By accurately adjusting all three forces, we achieved more adequate control of particle speed and moving direction through the sensing zone, which enables us to obtain more detailed information about particle size, charge, shape, and even chemical interactions. Chapter 4 reports the experimental details about controlling the dynamics of individual 8-nm-diameter gold nanoparticles, and the numerical models that semiquantitatively predicted the experimental observations.

1.3 Nanobubbles

Nanobubbles are gas-containing cavities with a nanometer size in the liquid solution. The pressure difference (Δp) between inside and outside a bubble, which is caused by the surface tension (γ) at the liquid-gas interface minimizing their surface area and therefore the volume, is governed by Young-Laplace equation (eq 1.5). Eq 1.5 predicts that the internal pressure of nanobubbles (p_{nb}) is extremely high due to its nano-scale curvature (r_{nb}). For example, a 200-nm radius air bubble in water has an internal

pressure of ~ 10 atm. The theoretical prediction of nanobubble internal pressure as a function of radius is shown in Figure 1.6.

$$\Delta p = p_{nb} - p_{out} = \frac{2\gamma}{r_{nb}} \tag{1.5}$$

The increased pressure within the nanobubble leads to an increase of the concentration of the gas in the liquid. According to Henry's law,[52] at a constant temperature, the amount of a given gas that dissolves in a given type and volume of liquid is directly proportional to the partial pressure of that gas in equilibrium with that liquid. For example, the solubility of the gas contained in 20-nm-radius bubbles is 100 fold higher than the solubility in ambient conditions. In other words, the bubbles should dissolve into the solution as soon as they are formed if the solution is not saturated with such high concentration gas. Researchers have not reached an agreement about whether these nanobubbles are able to survive in solution. A few research groups in Japan claimed that they have successfully produced solutions containing gas nanobubbles with radii less than 50 nm.[53-56]

In the past decade, the majority of research on nanobubbles has been on interfacial gas nanobubbles. Interfacial nanobubbles attach to a solid substrate instead of being suspended in solution. They have been successfully observed and characterized by tapping mode atomic force microscopy (TMAFM).[57-66] The development of new methods of generating[67-70] and detecting interfacial gas nanobubbles,[57-72] as well as the development of the theory and mechanism of nanobubble formation and stabilization [73-77]

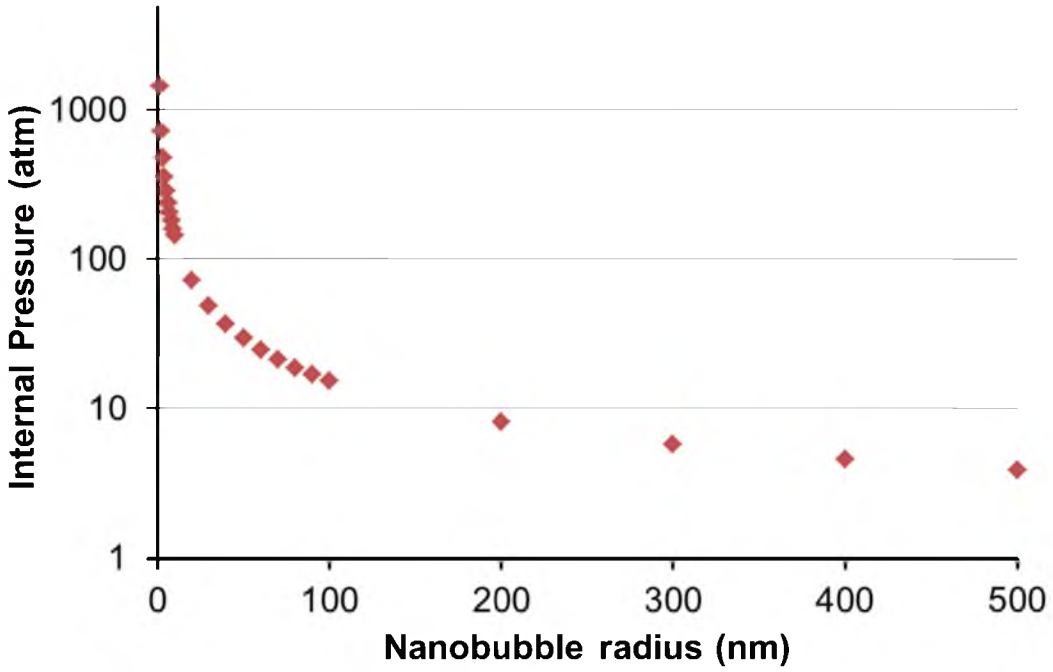

Figure 1.6. Theoretical prediction of the internal pressure of a nanobubble as a function of nanobubble radius using the Young-Laplace equation.

have greatly advanced. At present, it is possible to generate large ensembles of nanobubbles of different gas types at hydrophobic surfaces (*e.g.*, perfluorodecyltrichlorosilane (PFDTS) and highly orientated hydrophobic pyrolytic graphite (HOPG)) using the solvent exchange technique[57] or by the electrolysis of water.[67]

Previous studies by other researchers have shown that interfacial nanobubbles exist for hours or days, in contrast to the theoretical short lifetime due to rapid gas dissolution.[78] Several mechanisms have been proposed to explain the observed long lifetime of nanobubbles, such as the role of impurities at the interface,[75, 79, 80] dynamic steady-state,[69, 74] and contact line pinning,[73,77] but still no general agreement has been yet reached on the actual mechanism. Not only is the stabilization mechanism under debate, but also the mechanism of nanobubble formation remains unclear. It has been proposed that interfacial nanobubbles result from a supersaturation of gas at the interface.[73,81] However, Seddon *et al.*[82] and Dong *et al.*[83] recently reported the formation of surface nanobubbles in solutions that were not supersaturated by the corresponding gas. How nanobubbles form at the interface and why they remain stable are still open questions. Chapter 5 presents a new electrochemical approach for investigating the formation and stability of a single H_2 nanobubble at the solid substrate.

1.4 References

(1) Esaki, L. *Phys. Rev.* **1958**, 603-604.

(2) Siwy, Z. S. *Adv. Funct. Mater.* **2006**, *16*, 735–746.

(3) Wei, C.; Bard, A. J.; Feldberg, S. W. *Anal. Chem.* **1997,** *69*, 4627-4633.

(4) Siwy, Z. S.; Howorka, S. *Chem. Soc. Rev.* **2010**, *39*, 1115–1132.

(5) Guo, W.; Tian, Y.; Jiang, L. *Acc. Chem. Res.* **2013**, Article ASAP.

(6) Hou, X.; Guo, W.; Jiang, L. *Chem. Soc. Rev.* **2011**, *40*, 2385–2401.

(7) Cheng, L.-J.; Guo, L. J. *Chem. Soc. Rev.* **2010**, *39*, 923–938.

(8) Zhou, K. M.; Perry, J. M.; Jacobson, S. C. *Annu. Rev. Anal. Chem.* **2011**, *4*, 321–341.

(9) Siwy, Z.; Heins, E.; Harrell, C. C.; Kohli, P.; Martin, C. R. *J. Am. Chem. Soc.* **2004**, *126*, 10850–10851.

(10) Bard, A. J.; Faulkner, L. R. *Electrochemical Methods: Fundamentals and Applications*, 2nd ed.; John Wiley & Sons: New York, 2001; p548.

(11) Lee, S.; Zhang, Y.; Harrell, C. C.; Martin, C. R.; White, H. S. *Anal. Chem.* **2004**, *76*, 6108–6115.

(12) White, H. S.; Bund, A. *Langmuir* **2008**, *24*, 2212–2218.

(13) Yusko, E. C.; An, R.; Mayer, M. *ACS Nano* **2010**, *4*, 477–487.

(14) Cao, L.; Guo, W.; Wang, Y.; Jiang, L. *Langmuir* **2011,** *28* (4), 2194-2199.

(15) Siwy, Z. S.; Trofin, L.; Kohli, P.; Baker, L. A.; Trautmann, C.; Martin, C. R. *J. Am. Chem. Soc.* **2005**, *127*, 5000–5001.

(16) Vlassiouk, I.; Kozel, T. R.; Siwy, Z. S. *J. Am. Chem. Soc.* **2009**, *131*, 8211–8220.

(17) Ali, M.; Tahir, M. N.; Siwy, Z.; Neumann, R.; Tremel, W.; Ensinger, W. *Anal. Chem.* **2011**, *83*, 1673–1680.

(18) Yameen, B.; Ali, M.; Neumann, R.; Ensinger, W.; Knoll, W.; Azzaroni, O. *J. Am. Chem. Soc.* **2009**, *131*, 2070–2071.

(19) Ali, M.; Yameen, B.; Cervera, J.; Ramirez, P.; Neumann, R.; Ensinger, W.; Knoll, W.; Azzaroni, O. *J. Am. Chem. Soc.* **2010**, *132*, 8338–8348.

(20) Xia, F.; Guo, W.; Mao, Y.; Hou, X.; Xue, J.; Xia, H.; Wang, L.; Song, Y.; Ji, H.; Ouyang, Q.; Wang, Y.; Jiang, L. *J. Am. Chem. Soc.* **2008**, *130*, 8345–8350.

(21) Hou, X.; Yang, F.; Li, L.; Song, Y.; Jiang, L.; Zhu, D. *J. Am. Chem. Soc.* **2010**, *132*, 11736–11742.

(22) Coulter, W. H., Means of Counting Particles Suspended in a Fluid. *US Patent No. 2,656,508* **1953**.

(23) Berge, L. I. *J. Colloid Interface Sci.* **1990,** *134* (2), 548-562.

(24) Li, J.; Stein, D.; McMullan, C.; Branton, D.; Aziz, M. J.; Golovchenko, J. A. *Nature* **2001,** *412*, 166-9.

(25) Martin, C. R. *Science* **1994,** *266* (5193), 1961-6.

(26) (a) Ito, T.; Sun, L.; Henriquez, R. R.; Crooks, R. M. *Acc. Chem. Res.* **2004,** *37*, 937-945. (b) Sun, L.; Crooks, R. M. *J. Am. Chem. Soc.* **2000,** *122* (49), 12340-12345.

(27) Saleh, O. A.; Sohn, L. L. *Rev. Sci. Instrum.* **2001,** *72* (12), 4449-4451.

(28) Yu, S.; Lee, S. B.; Martin, C. R. *Anal. Chem.* **2003,** *75* (6), 1239-44.

(29) Martin, C. R.; Siwy, Z. S. *Science* **2007,** *317* (5836), 331-2.

(30) Sexton, L. T.; Horne, L. P.; Martin, C. R. *Mol. Biosyst.* **2007,** *3* (10), 667-85.

(31) Zhang, B.; Galusha, J.; Shiozawa, P. G.; Wang, G.; Bergren, A. J.; Jones, R. M.; White, R. J.; Ervin, E. N.; Cauley, C. C.; White, H. S. *Anal. Chem.* **2007,** *79* (13), 4778-87

(32) Willmott, G. R.; Vogel, R.; Yu, S. S. C.; Groenewegen, L. G.; Roberts, G. S.; Kozak, D.; Anderson, W.; Trau, M. *J. Phys.: Condens. Matter* **2010,** *22* (45), 454116;

(33) Liu, S.; Yuzvinsky, T. D.; Schmidt, H. *ACS Nano* **2013,** *7* (6), 5621-7;

(34) Zhang, B.; Wood, M.; Lee, H. *Anal. Chem.* **2009,** *81* (13), 5541-8

(35) Gao, C.; Ding, S.; Tan, Q.; Gu, L. Q. *Anal. Chem.* **2009,** *81*, 80-86.

(36) Bezrukov, S. M.; Vodyanoy, I.; Parsegian, V. A. *Nature* **1994,** *370*, 279-281.

(37) Kasianowicz, J. J.; Brandin, E.; Branton, D.; Deamer, D. W. *Proc. Natl. Acad. Sci. U.S.A.* **1996,** *93*, 13770-13773;

(38) Gu, L. Q.; Braha, O.; Conlan, S.; Cheley, S.; Bayley, H. *Nature* **1999,** *398* (6729), 686-90.

(39) DeBlois, R. W.; Wesley, R. K. A. *J. Virol.* **1977,** *23*, 227-233.

(40) DeBlois, R. W.; Bean, C. P.; Wesley, R. K. A. *J. Colloid Interface Sci.* **1977,** *61*, 323-335.

(41) DeBlois, R. W.; Bean, C. P. *Rev. Sci. Instrum.* **1970,** *41* (7), 909-916.

(42) Ito, T.; Sun, L.; Bevan, M. A.; Crooks, R. M. *Langmuir* **2004,** *20*, 6940-6945.

(43) Henriquez, R. R.; Ito, T.; Sun, L.; Crooks, R. M. *Analyst* **2004,** *129* (6), 478-82.

(44) Ito, T.; Sun, L.; Crooks, R. M. *Anal. Chem.* **2003,** *75* (10), 2399-2406.

(45) Zhang, B.; Zhang, Y.; White, H. S. *Anal. Chem.* **2004,** *76* (21), 6229-38.

(46) Willmott, G. R.; Parry, B. E. T. *J. Appl. Phys.* **2011,** *109* (9), 094307-13.

(47) Kozak, D.; Anderson, W.; Vogel, R.; Chen, S.; Antaw, F.; Trau, M. *ACS Nano* **2012,** *6* (8), 6990-7

(48) Lan, W. J.; Holden, D. A.; Zhang, B.; White, H. S. *Anal. Chem.* **2011,** *83* (10), 3840-7.

(49) Davenport, M.; Healy, K.; Pevarnik, M.; Teslich, N.; Cabrini, S.; Morrison, A. P.; Siwy, Z. S.; Letant, S. E. *ACS Nano* **2012,** *6* (9), 8366-80.

(50) Schoch, R. B.; Han, J.; Renaud, P. *Rev. Mod. Phys.* **2008,** *80* (3), 839-883

(51) Lan, W.-J.; White, H. S. *ACS Nano* **2012,** *6* (2), 1757-1765.

(52) Henry, W. *Phil. Trans. R. Soc. Lond.* **1803**, *93*, 29-42.

(53) Ohgaki, K.; Khanh, N. Q.; Joden, Y.; Tsuji, A.; Nakagawa, T. *Chem. Eng. Sci.* **2010**, *65*, 1296-1300.

(54) Kikuchi, K.; Ioka, A.; Oku, T.; Tanaka, Y.;Saihara, Y.; Ogumi, Z. *J. Colloid Interface Sci.* **2009**, *329*, 306-309.

(55) Kikuchi, K.; Nagata, S.; Tanaka, Y.; Saihara, Y.; Ogumi, Z. *J. Electroanal. Chem.***2007,** *600*, 303-310.

(56) Ushikubo, F.Y.; Furukawa, T.; Nakagawa, R.; Enari, M.; Makino, Y.; Kawagoe, Y.; Shiina, T.;Oshita, S. *Colloid Surf, A*, **2010**, *361*, 31-37.

(57) Lou, S. T.; Ouyang, Z. Q.; Zhang, Y.; Li, X. J.; Hu, J.; Li M. Q.; Yang, F. J. *J. Vac. Sci. Technol., B*, **2000**, *18*, 2573-2575.

(58) Lou, S. T.; Gao, J. X.; Xiao, X. D.; Li, X. J.; Li, G. L.; Zhang, Y.; Li, M. Q.; Sun, J. L.; Li,X. H.; Hu, J. *Mater. Charact.*, **2002**, *48*, 211-214.

(59) Yang, J. W.; Duan, J. M.; Fornasiero. D.; Ralston, J. *J. Phys. Chem. B*, **2003**, *107*, 6139-6147.

(60) Zhang, X. H.; Maeda, N.; Craig, V. S. J. *Langmuir*, **2006**, *22*, 5025-5035.

(61) Switkes, M.; Ruberti, J. W. *Appl. Phys. Lett.*, **2004**, *84*, 4759-4761.

(62) Zhang, J.; Yoon, R.-H.; Mao, M.; Ducker, W. A. *Langmuir*, **2005**, *21*, 5831-5841.

(63) Zhang, X. H.; Li, G.; Maeda, N.; Hu, J. *Langmuir*, **2006**, *22*, 9238-9243.

(64) Zhang, X. H.; Zhang, X. D.; Sun, J. L.; Zhang, Z. X.; Li, G.; Fang, H. P.; Xiao, X. D.; Zeng, X. C.; Hu, J. *Langmuir*, **2007**, *23*, 1778-1783.

(65) van Limbeek, M. A. J.; Seddon, J. R. T. *Langmuir* **2011**, 27, 8694-8699.

(66) Zhang, L.; Zhang, X.; Zhang, Y.; Hu, J.; Fang, H. *Soft Matter* **2010**, *6*, 4515-4519.

(67) Zhang, L. J.; Zhang, Y.; Zhang, X. H.; Li, Z. X.; Shen, G. X.; Ye, M.; Fan, C. H.; Fang; H. P.; Hu, J. *Langmuir* **2006**, *22*, 8109-8113.

(68) Liu, G. M.; Wu, Z. H.; Craig, V. S. J. *J. Phys. Chem. C*, **2008**, *112*, 16748-16753.

(69) Yang, S. J.; Tsai, P. C.; Kooij, E. S.; Prosperetti, A.; Zandvliet, H. J. W.; Lohse, D. L*angmuir*, **2013**, *29* , 5937–5937.

(70) Yang, S. J.; Tsai, P. C.; Kooij, E. S.; Prosperetti, A.; Zandvliet, H. J. W.; Lohse, D. *Langmuir* **2009**, *25*, 1466-1474.

(71) Zhang, X. H.; Quinn, A.; Ducker, W. A. *Langmuir* **2008**, *24*, 4756−4764.

(72) Karpitschka,S.; Dietrich, E.; Seddon, J.R.T.; Zandvliet, H. J. W.;, Lohse, D.; Riegler, H.; *Phys. Rev. Lett.* **2012**, *109*, 066102.

(73) Zhang, X.; Chan, D. Y. C.; Wang, D.; Maeda, N. *Langmuir* **2013**, 29, 1017-1023.

(74) Brenner, M. P.; Lohse, D. *Phys. Rev. Lett.* **2008**, *101*, 214505.

(75) Ducker, W. A. *Langmuir* **2009**, *25*, 8907- 8910.

(76) Weijs, J. H.; Lohse, D. *Phys. Rev. Lett.* **2013**,*110*, 054501.

(77) Liu, Y.; Zhang, X. *J. Chem. Phys.* **2013**, *138*, 014706.

(78) Ljunggren, S.; Eriksson, J. C. *Colloids Surf. A* **1997**, *130*, 151-155.

(79) Das, S. *Phys. Rev. E* **2011**, *83*, 066315.

(80) Das, S.; Snoeijer, J. H.; Lohse, D. *Phys. Rev. E* **2010**, 82, 056310.

(81) Craig, V. S. J. *Soft Matter* **2011**, *7*, 40-48.

(82) Seddon, J. R. T.; Kooij, E. S.; Poelsema, B.; Zandvliet, H. J. W.; Lohse, D. *Phys. Rev. Lett.* **2011**, *106*, 056101.

(83) Guan, M.; Guo, W.; Gao, L.; Tang, Y.; Hu, J.; Dong, Y. *ChemPhysChem* **2012**, *13*, 2115-2118.

CHAPTER 2

TUNABLE NEGATIVE DIFFERENTIAL ELECTROLYTE RESISTANCE IN A CONICAL NANOPORE IN GLASS

2.1 Introduction

Negative differential resistance (NDR) is a technologically important electrical phenomenon in which electrical current *decreases* as an applied voltage is increased. This behavior is different from most electrical devices in which current is observed to increase with increasing driving force. Various NDR behaviors have been observed in solid-state devices, being primarily associated with contact or junction phenomena,[1] among which the Esaki or tunnel diode[2] is especially well known. NDR investigations recently extend far beyond traditional solid-state devices to include single-molecule based electronic junctions, and graphene/carbon nanotube based electronics.[3-15]

In this chapter, a simple and general method to produce NDR phenomena based on solution ion conductivity within confined nanoscale geometry is demonstrated. Our device is based on an ~50 μm thick glass membrane containing a single, electrically charged, conical shaped nanopore, which has been developed in our laboratory for nanoparticle detection,[16-18] as well as for the investigations of microgel[19] and liposome[20] translocation in porous media. In the NDR investigation reported here, the membrane separates two electrolyte solutions that possess significantly different ionic conductivities,

as shown in Figure 2.1a. The external solution is a mixed DMSO/H_2O solution (*v:v* 3:1) containing 5 mM KCl that has a relatively low conductivity; the internal solution is a 5 mM KCl aqueous solution which has an electrical conductivity approximately 4 times larger than the external solution.

To observe the NDR behavior, a positive constant pressure is applied inside the capillary to which the membrane nanopore is attached, resulting in the high conductivity internal solution being driven outward through the pore. Simultaneously, a voltage is applied across the membrane to induce electro-osmotic flow of the external solution in the direction opposite of the pressure driven flow, a consequence of the negative surface charge of the glass. Although the internal and external solutions are completely miscible, the radius of the nanopore orifice is sufficiently small (~300 nm) to result in *steady-state* convergent/divergent ion fluxes and flows on the internal/external sides of the orifice. Consequently, a well-defined and relatively sharp interfacial zone is established whose position is determined by the balance of the constant pressure force and voltage-dependent electro-osmotic force. As demonstrated herein, by varying the applied voltage at a constant applied pressure, the steady-state interfacial zone can be positioned outside of the nanopore (Figure 2.1b, in the external solution), within the nanopore (Figure 2.1d, in the internal solution), or directly at the nanopore orifice (Figure 2.1c). Because the mass-transfer resistance of the nanopore is largely localized to the volume of solution immediately adjacent to the sides of the pore orifice, the voltage-dependent electro-osmotic force results in the interfacial zone passing through the region of space most sensitive to the electrolyte conductivity (the "sensing zone") as the voltage is varied; this movement of the transition zone results in a sharp increase in the nanopore resistance

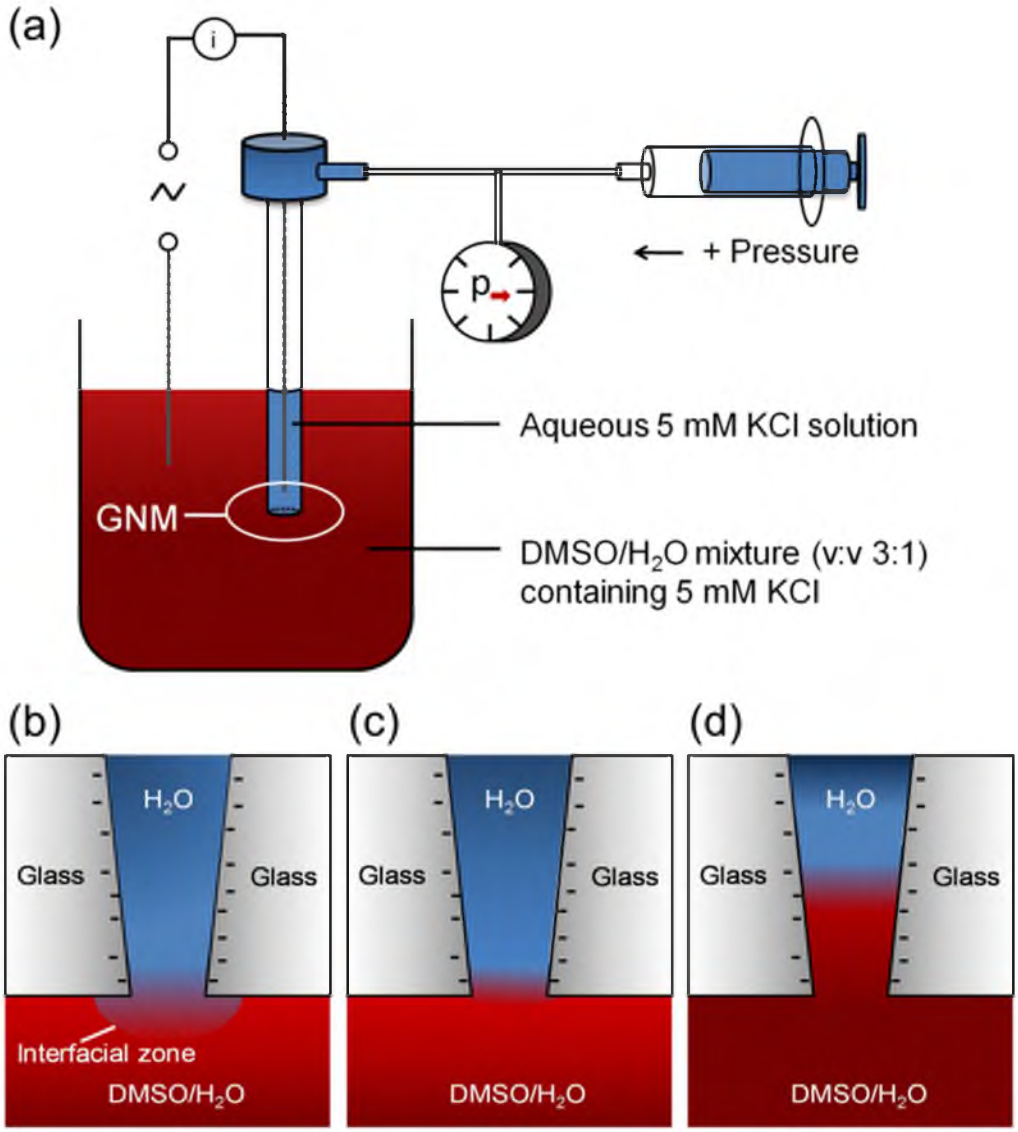

Figure 2.1. a) Schematic illustration of the NDR experiment and the glass nanopore membrane (GNM). A potential difference is applied between the two Ag/AgCl electrodes. The internal solution is an aqueous 5 mM KCl solution and the external solution is a 3:1 (*v/v*) DMSO/H_2O mixture containing 5 mM KCl. b), c) and d) show the interfacial zone outside, right on the orifice and inside the nanopore orifice.

when the low conductivity solution enters this region, which is reflected as a sudden decrease in the current in *i-V* traces. Experimental results and computer simulations demonstrating these principles are presented in this chapter.

Since the discovery of ion current rectification (ICR) in a conical shaped nanopore by Wei, Feldberg and Bard,[21] the current-voltage response of asymmetric charged nanopores and nanochannels has received significant attention due to its departure from classic linear ohmic behavior. Extensive research on the experimental and theoretical aspects of ion current rectification (ICR) associated with nanopores with asymmetric geometry or asymmetric charge distribution has been reported over the past two decades.[22 - 46] ICR in a charged conical-shaped nanopore results from the accumulation and depletion of ions near the orifice of the nanopore, and has been detailed elsewhere.[23,30,32,42] Siwy and coworkers reported NDR gating behavior in a conical nanopore upon surface charge reversal due to voltage dependent binding of Ca^{2+} to the nanopore surface.[47,48] The NDR phenomenon reported here builds on this research base. Specifically, in a recent article, Yusko and Mayer described a borosilicate glass membrane containing a single nanopore that separated the same DMSO/H_2O and aqueous electrolyte compositions employed in this report; these researchers reported that the degree of ICR could be enhanced by drawing the external low conductivity solution into the nanopore by electro-osmosis.[49] Conversely, our laboratory recently demonstrated that ICR can be eliminated by pressure driven flow.[50] These two results are combined to create a nanopore exhibiting NDR.

Similar to the use of NDR based solid-state switches in electronics, a nanopore exhibiting NDR can potentially be employed to amplify small electrical perturbations. In

this chapter, we also demonstrate that a small change in the voltage across the nanopore (a few mV) can result in large change (~80%) in the electrical current. Such highly nonlinear electrical responses may be especially suitable for solution phase chemical sensing.

2.2 Experimental section

2.2.1 Chemicals and materials

KCl (99.8%, Mallinckrodt) and DMSO (99.9%, EMD Chemical) were used as received. All aqueous solutions were prepared using water (18 MΩ·cm) from a Barnstead E-pure H_2O purification system.

2.2.2 Glass nanopore membranes (GNMs) fabrication

GNMs were fabricated according to previous reports from our laboratory.[51] Briefly, a Pt wire attached to the tungsten fiber was electrochemically sharpened in a NaCN solution and then sealed in a glass capillary (Dagan Corp., Prism glass capillaries, SB16, 1.65 mm outer diameter, 0.75 mm inner diameter, softening point 700 °C) using a H_2/air flame. The capillary was then polished until a Pt nanodisk was exposed, as indicated by an electronic feedback circuit. Optical images of the capillary showing the polishing process are presented in 2.5 Appendix. The Pt nanodisk was then partially etched in a 20% $CaCl_2$ solution by applying a 6 V A. C. voltage between the Pt nanodisk and a large Pt wire counter electrode, and then the remaining Pt wire was gently removed by pulling out the tungsten fiber. The orifice radius of the resulting conical nanopore was determined from the resistance of the pore in 1.0 M KCl solution as previously described.

(See 2.5 Appendix.) Experimental results were obtained using three GNMs with orifice radii ranging from 240 to 380 nm. However, the NDR phenomena described in this report have been reproduced using other nanopores with similar size orifice radii. A GNM with a much larger orifice radius (857 nm) did not exhibit NDR, as reported in 2.5 Appendix.

2.2.3 Cell configuration and data acquisition

A Dagan Cornerstone Chem-Clamp potentiostat and a Pine RDE4 (used as the waveform generator) were interfaced to a computer through a PCI data acquisition board (National Instruments). Current-voltage (*i-V*) curves were recorded by in-house virtual instrumentation written in LabVIEW (National Instrument) at a data acquisition rate of 10 kHz. A 3-pole Bessel low-pass filter was applied at a cut-off frequency of 1 kHz. The GNM was filled and immersed in a 5 mM KCl aqueous solution and the *i-V* curve measured to ensure the cleanness of the nanopore by checking the dependence of ICR response on applied pressure driven flow. Clean nanopores showed agreement with expectations that ICR disappears with pressure applied, based on the results in ref. 50. The GNM was then removed from solution, and excess surface liquid was wiped off. The GNM was then immersed in the 5 mM KCl DMSO/water mixture (*v:v* 3:1) containing 5 mM KCl and *i-V* measurements were recorded. Electrical contact to the solutions was made using Ag/AgCl electrodes. Pressure was applied across the GNM, Figure 2.1, using a 10 mL gastight syringe (Hamilton Co., Reno, Nevada) and measured with a Marshalltown-Tempco, Inc. pressure gauge with a sensing range between 0 to 300 mmHg.

2.2.4 Finite-element simulations

The finite-element simulations were performed to investigate the NDR mechanism using COMSOL Multiphysics 4.1 (Comsol, Inc.).

2.3 Results and discussion

2.3.1 Negative Differential Resistance (NDR)

Figure 2.2a shows the *i-V* response of a 380 nm radius GNM containing an aqueous internal solution and immersed in a mixed DMSO/H_2O (*v:v* 3:1) external solution; both solutions contained 5 mM KCl. The family of curves corresponds to different constant positive pressures applied inside the capillary, ranging between 0 and 50 mmHg. The applied voltage corresponds to the potential of the internal Ag/AgCl electrode *vs.* the external Ag/AgCl electrode.

At nonzero applied pressures, a large *reversible* decrease in the current occurs as the potential is scanned to negative values, Figure 2.2a. The decrease in current, as the electrical driving force is increased, corresponds to a region of NDR. Prior to and following the potential at which NDR occurs (referred to as the "turning point"), the nanopore exhibits quasi-ohmic behavior, but the conductance of the nanopore at potentials positive of the turning point (~2×10^{-8} Ω^{-1}) is approximately one order of magnitude larger than at negative potentials (~2×10^{-9} Ω^{-1}) (determined from the slopes of the *i-V* curves). As the applied pressure is increased, the turning point shifted to more negative voltages. The NDR *i-V* curve was reversible and repeatable as the voltage was swept between -2 to 2 V, as shown in Figure 2.2b. The *i-V* response of a 330 nm radius GNM exhibiting nearly identical NDR behavior as a function of pressure, is presented in

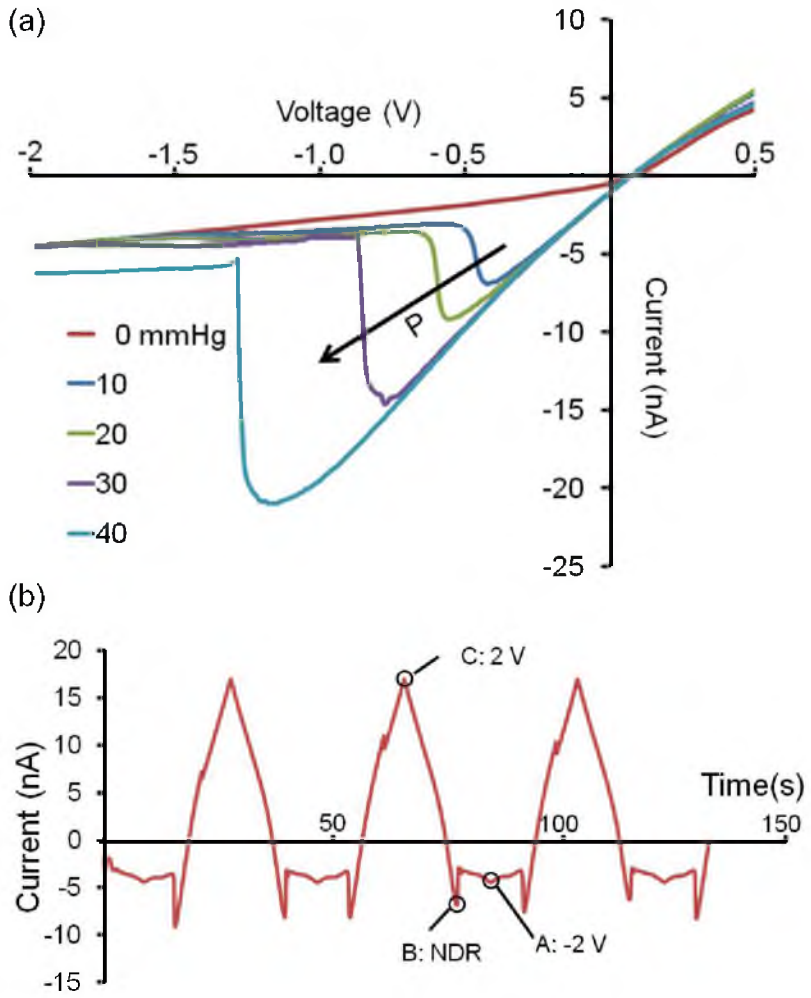

Figure 2.2. *i-V* response of the 380 nm radius GNM as a function of the applied positive pressure (internal *vs.* external). The voltage was scanned from 2 to -2 V at a rate of 200 mV/s. Internal and external solutions were an aqueous 5 mM KCl solution and a DMSO/water (*v:v* 3:1) mixture containing 5 mM KCl, respectively. (b) *i-t* recording of the 380 nm radius GNM when a 20 mmHg positive pressure was applied across the nanopore, and the voltage was cycled between -2 V (Point A) and 2 V (Point C) at a scan rate of 200 mV/s. Point B is the voltage where NDR occurs.

2.5 Appendix and includes both forward and reverse scans which give some indication of the hysteresis in the NDR turning point (10 to 100 mV at different pressures for the data in 2.5 Appendix. The degree of hysteresis observed in the NDR turning point varied from nanopore to nanopore, and increased with increasing scan rates, but has not been fully explored. Presumably the hysteresis arises from the relatively slow redistribution of solvent and ions.[37, 38]

The NDR phenomenon can be qualitatively understood by considering the position of the interfacial zone between the internal high-conductivity solution and external low-conductivity solution, *relative* to the location of the electric potential drop at the nanopore orifice. First, it is important to note that because the pore is conical shaped, the fluxes of ions and solvent molecules are radially convergent (or divergent, depending on the direction of the current and applied pressure), resulting in a steady-state *i-V* response at slow scan rates and a steady-state distribution of ions and molecules. Consequently, a well-defined and relatively sharp interfacial zone exists between the solutions, with a location that is determined by the balance of the constant pressure force and the voltage-dependent electro-osmotic force. Conversely, the location of electric potential drop across the nanopore is largely voltage independent, and is distributed over a region of solution on both sides of the orifice; the width of this sensing zone is of the same order of magnitude as the pore radius, as previously demonstrated [52] (see 2.5 Appendix for an example of the potential distribution across a 400 nm nanopore). By varying the applied voltage at a constant applied pressure, the variable electro-osmotic force can be used to scan the position the interfacial zone between the internal and external solutions across the sensing zone. Qualitatively, a high nanopore conductance

state exists at low negative voltages or at high applied pressures, corresponding to the interfacial zone located on the external side of the orifice, and the internal aqueous 5 mM KCl solution occupying the sensing zone; conversely, a low nanopore conductance state exists at high negative voltages or at low applied pressures, corresponding to the interfacial zone located on the internal side of the orifice, and the external DMSO/H_2O 5 mM KCl solution occupying the sensing zone. For a particular combination of applied pressure and voltage, the NDR turning point occurs when interfacial zone passes through the orifice.

2.3.2 Finite-element simulations of the nanopore NDR phenomenon

Steady-state finite element simulations using COMSOL Multiphysics were performed to provide a more quantitative description of the experimental results. The internal solution was modeled as a 5 mM KCl aqueous solution and the external as a 5 mM KCl in DMSO/H_2O mixture (volume fraction of DMSO = 0.8). DMSO is treated as a solute that is transported from the external DMSO/H_2O solution to the internal aqueous solution. The 2D axial-symmetric geometry and boundary conditions are provided in 2.5 Appendix. The radius of the nanopore opening was set as 400 nm and the thickness of the GNM as 20 μm, corresponding approximately to the nanopore geometry used in the experiments. A surface charge of -26 mC/m^2 was assumed (see 2.5 Appendix for details).[41, 50]

A description of ion and solvent transport in the nanopore begins with the Navier-Stokes equation, describing pressure and electric force driven flow.

$$\mathbf{u}\nabla\mathbf{u} = \frac{1}{\rho}(-\nabla p + \eta\nabla^2\mathbf{u} - F(\sum_i z_i c_i)\nabla\Phi) \tag{2.1}$$

In eq 2.1, **u** and Φ are the local position-dependent fluid velocity and potential, ρ and η are the density and viscosity of the fluid, respectively, c_i and z_i are concentration and charge of species i in solution, p is the pressure and F is the Faraday's constant. For computational simplicity, we assume a constant value for ρ of 1000 kg/m^3. However, ion diffusivities and mobilities are strongly dependent on η; thus, literature values of η for DMSO/H_2O mixtures[53] were used in the simulation, as detailed in 2.5 Appendix.

The ion fluxes are modeled by the Nernst-Planck equation, including the diffusion, migration and convection terms.

$$\mathbf{J}_i = -D_i\nabla c_i - \frac{Fz_i}{RT}D_i c_i\nabla\Phi + c_i\mathbf{u} \tag{2.2}$$

In eq 2.2, $\mathbf{J}_i$ and D_i, are, respectively, the ion flux vector and diffusion coefficient of species i in solution and T is the absolute temperature. The ion diffusion coefficients D_i in DMSO/water mixtures were estimated by Stokes-Einstein equation, eq 2.3, using the composition-dependent value of η (see 2.5 Appendix).

$$D_i = \frac{k_B T}{6\pi\eta r} \tag{2.3}$$

In eq 2.3, k_B is Boltzmann's constant and r is the solvated radius of the species i. A value of $r = 1.5 \times 10^{-10}$ m was employed for both K^+ and Cl^-.

The relationship between the local ion distributions and potential is described by Poisson's equation, eq 2.4,

$$\nabla^2\Phi = -\frac{F}{\varepsilon}\sum_i z_i c_i \tag{2.4}$$

Here, ε is the dielectric constant of medium, which is also dependent on the molar fraction of DMSO in the DMSO/water mixture (see 2.5 Appendix).[54]

Eqs 2.1 to 2.4 are coupled with an additional equation describing the flux of DMSO.

$$\mathbf{J}_{DMSO} = D_{DMSO}\nabla c_{DMSO} + c_{DMSO}\mathbf{u} \tag{2.5}$$

In this model, to simplify the computations, we assumed D_{DMSO} to be independent of the solution composition (1.25×10^{-9} m^2/s), and the interfacial tension[55] between the external and internal solution was not taken into consideration. The interface between the external and internal solutions was initially set at the nanopore orifice.

Figure 2.3a shows the simulated *i-V* response of the nanopore in absence of an applied pressure across the GNM. The simulation captures the electro-osmosis-induced enhancement of ICR, first reported by Yusko and Mayer *et al.*[49] (We also verified the experimental results of Yusko and Mayer, see 2.5 Appendix) As seen in Figure 2.3a, at

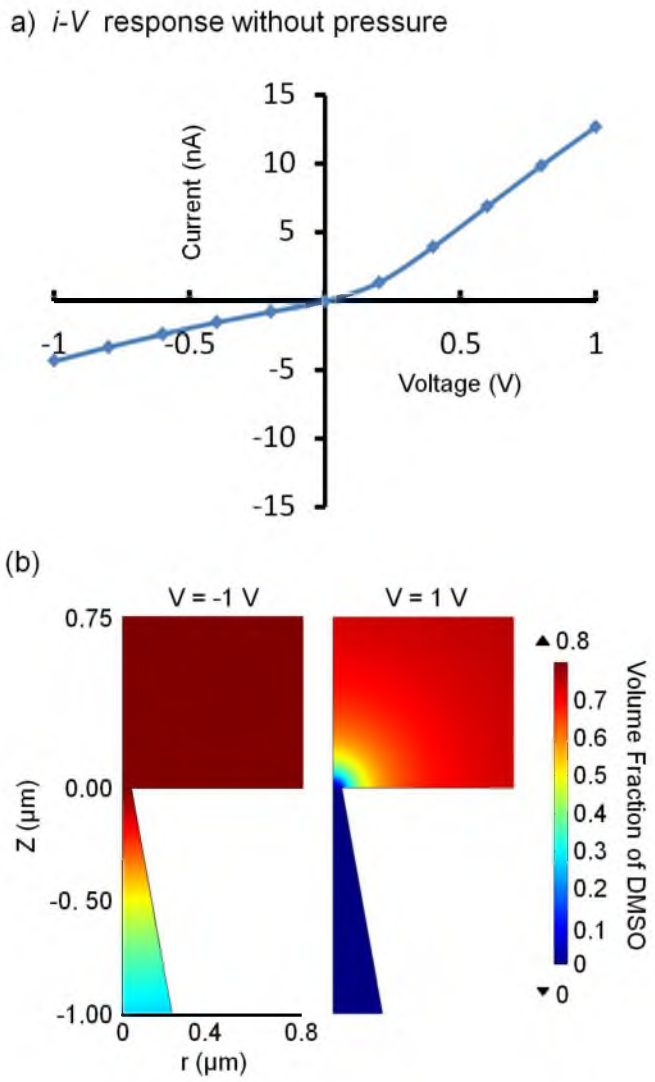

Figure 2.3. Simulation of electro-osmosis induced ICR behavior. (a) Simulated steady-state *i-V* response of a 400 nm radius GNM in the absence of an applied pressure. In the simulation, the external solution ($z > 0$) initially contained a solution of 5 mM KCl in DMSO/water mixture (volume fraction of DMSO = 0.8), while the internal aqueous solution ($z < 0$) initially contained 5 mM KCl. The surface of nanopore is negatively charged (-26 mC/m^2). (b) is simulated steady-state volume fraction distributions of DMSO at -1 V and 1 V (internal *vs.* external). $r = 0$ is the symmetry axis of the GNM geometry, while $z = 0$ corresponds to the nanopore orifice.

potentials more positive than ~0.2 V and at negative potentials, the *i-V* responses are approximately ohmic. Between these two zones, there is a short transition range where nonlinear *i-V* behavior is observed. Figure 2.3b shows plots of the simulated DMSO volume fraction distribution at 1 V and -1 V. At V = 1 V, the DMSO distribution gradient is pushed out of the nanopore, resulting in the high conductivity internal solution occupying the sensing zone of nanopore. At V = -1 V, the DMSO/H_2O solution is driven into the nanopore by electro-osmosis, forming an interfacial zone below the orifice; the solution at the sensing zone has essentially the same composition as the external bulk solution, resulting in a low conductivity state. In summary, the finite-element simulations are in good agreement with the experimental results of Yusko and Mayer and indicate that the enhanced ICR results from electro-osmosis driven positioning of the interfacial zone below (negative potentials) or above (positive potentials) the nanopore orifice.

Figure 2.4a shows the numerically simulated *i-V* response in the absence (blue line) and presence of 5 mmHg applied pressure (red line), for the same GNM as described above. The simulation qualitatively captures the existence of the nanopore NDR phenomenon at negative potentials when a pressure is applied across the GNM. A sudden decrease in the current is observed between -0.770 and -0.778 V, similar in shape, albeit smaller, than that observed in the experiments. Given the several approximations employed in the simulation, e.g., the surface tension between the two solutions not taken into account and the immediate mixing of two solutions, the qualitative agreement between these preliminary simulations and experiment is considered to be reasonable. Figure 2.4b shows the distribution of DMSO across the nanopore as a function of the applied potential. Similar to the results presented in the preceding section, the interfacial

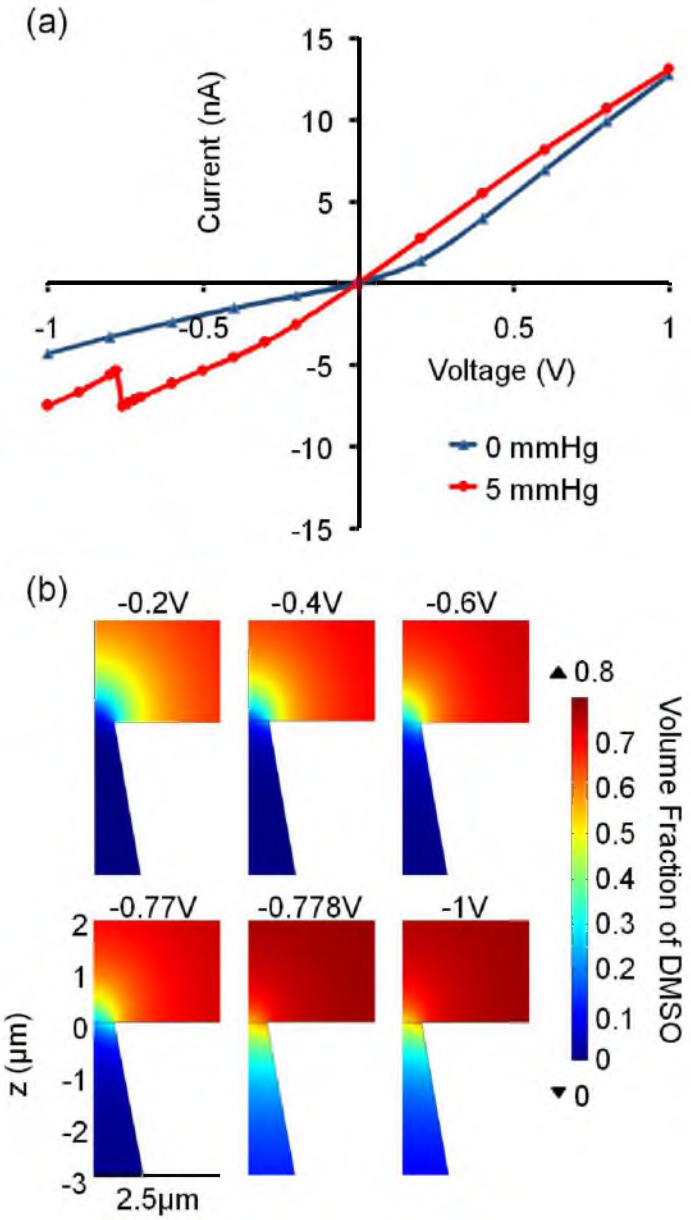

Figure 2.4. Simulation of NDR behavior in a nanopore. (a) Simulated *i-V* curves of a 400 nm radius nanopore at 5 mmHg pressure (red line) and in the absence of pressure (blue line).The other initial settings are the same as Figure 2.3. (b) The volume fraction distributions of DMSO at selected voltages ranging from -0.2 to -1 V.

zone between the external DMSO/H_2O and internal H_2O solutions is a function of the applied potential, a consequence of the electro-osmotic forces driving the external solution inward through the nanopore. However, as the potential is varied from -0.770 to -0.778 V in the simulated *i-V* curve (Figure 2.4a), the results in Figure 2.4b show that the onset of NDR is accompanied by a discontinuous jump due to the positioning of the interfacial zone from the external solution to a position within the nanopore. This abrupt change in position results in the nanopore switching from a high conductivity state to a low conductivity state.

Ion and solvent diffusion, electro-osmosis and pressure driven flow each contribute to the position of the interfacial zone. A complete understanding of how these highly coupled factors lead to the NDR behavior is beyond the scope of this report. However, the following discussion presents our preliminary understanding of the phenomenon. Figure 2.5 shows the simulated *steady-state* DMSO convective and diffusive flux vectors at the orifice of the nanopore at -0.770 V, just prior to the nanopore entering the low conductivity state. This figure shows that the convective flux (black arrows) due to the applied pressure engendered force is largest across the central region of the nanopore orifice and is directed outward, while the diffusive flux of DMSO (red arrows) and the convective flux due to electro-osmosis is directed inward along the circumference of the orifice. At steady-state, the outward directed pressure-driven convective flux must balance the inward directed diffusive flux and electro-osmosis-driven convective flux, resulting in a stationary interfacial zone that is located external to the nanopore (Figure 2.4b, -0.770 V). As the voltage is shifted to a slightly more negative value, the electro-osmotic force increases resulting in a larger inward electro-

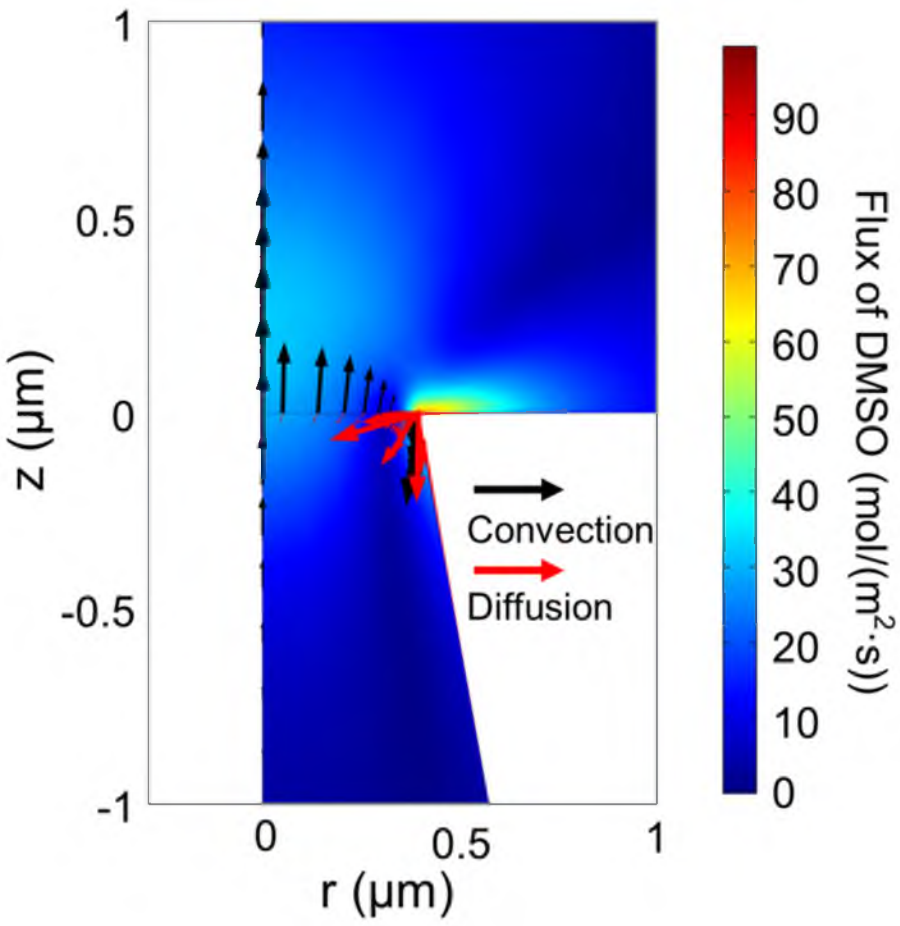

Figure 2.5. Simulated steady-state DMSO flux in the 400 nm radius GNM at an applied voltage of -0.77 V (internal *vs.* external). The color surface indicates the net DMSO flux magnitude. The flux vectors at the opening of nanopore indicate the directions and relative magnitudes of the convective (black arrows) and diffusive DMSO fluxes (red arrows).

osmosis-driven convective DMSO flux and the movement of the interfacial zone towards the nanopore interior. We speculate that the very nonlinear NDR behavior results from the increase in the viscosity of the solution as the DMSO concentration increases at the orifice, resulting in a further decrease in the outward convective flow. The resulting decrease in outward flow would result in even higher DMSO concentrations within the nanopore, and the process would continue until the nanopore entered the low conducting state; at that point, the electro-osmotic forces would decrease and a new steady state interfacial zone between the external and internal solutions would be established. Additional numerical simulations of this system are required to better understand the positive feedback process that leads to NDR.

The computational results indicate that the transition between high and low conductivity states in the nanopore can occur over a very narrow potential range (< 8 mV). This behavior corresponds to a nanopore electrical switch and has potentially interesting applications in chemical sensing. For instance, because the NDR behavior is a function of the electro-osmotic force generated within the nanopore, the potential at which the turning point is observed will be a function of the electrical charge density on the nanopore surface. Thus, by modifying the nanopore surface with receptors that bind charged analytes, it appears plausible to build a nanopore "on/off" switch that allows detection of the presence of a small amount of analyte. In a preliminary experiment, we constructed a GNM with a smaller orifice (230 nm radius) and measured the *i-V* response at a slow scan rate (10 mV/s) to estimate how sharp of a conductivity transition can be realized, and whether or not the simulated prediction of an 8 mV wide transition window is reasonable. Figure 2.6 shows the *i-V* response for this experiment, recorded under the

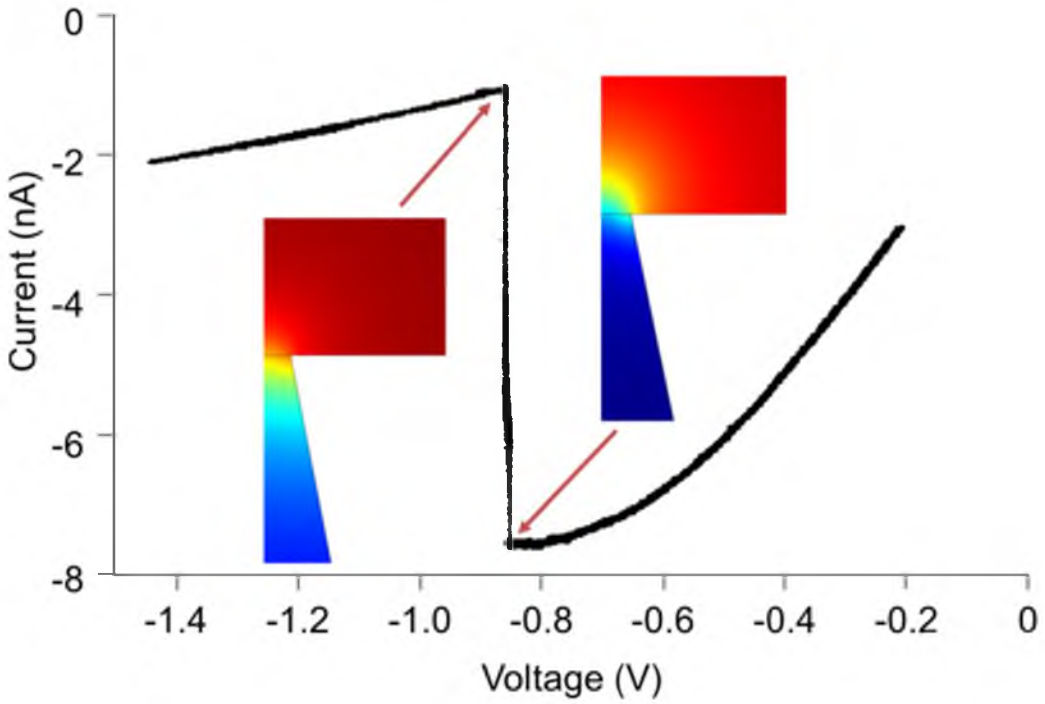

Figure 2.6. Experimental NDR behavior for a 230 nm radius GNM with a scan rate of 10 mV/s and 20 mmHg pressure applied across the membrane. NDR behavior occurs over a potential difference of ~7 mV (from -0.852 to -0.859 V). Internal and external solutions were an aqueous 5 mM KCl solution and a DMSO/water (*v:v* 3:1) mixture containing 5 mM KCl, respectively. The volume fraction distributions of DMSO before and after the NDR point are taken from Figure 2.4 (-0.770 and -0.778V) to reiterate the origin of the NDR behavior.

same conditions as in previous experiments. The current decreases by ~80% over a 7 mV range, demonstrating that very sharp NDR transitions can be obtained using smaller nanopores and slow scan rates.

Finally, we note that the NDR behavior reported here can, in principle, be realized using solvents other than DMSO and water. The only requirements of our proposed mechanism are that the external and internal solutions are miscible, and that they have significantly different ionic conductivities. Thus, it is likely that charged nanopores employed with other appropriate solution compositions will also exhibit NDR behavior.

2.4 Conclusions

We have demonstrated that liquid-phase NDR was observed in the *i-V* behavior of a negatively charged conical nanopore in a glass membrane that separates an external *low-conductivity* solution from an internal *high-conductivity* aqueous solution. NDR results from the voltage-dependent electro-osmotic force opposing an externally applied pressure force, continuously moving the location of the interfacial zone between the two miscible solutions through the nanopore orifice until a potential of interfacial instability is reached. The NDR curve is reversible and can be tuned by adjusting the pressure across the GNM. Preliminary numerical simulations support the proposed mechanism and are able to semiquantitatively capture the NDR response. Current work is being directed towards developing a better understanding of the NDR behavior, as well as applying this phenomenon in chemical analyses.

2.5 Appendix

In this appendix, optical microscopy images of the GNM during polishing, *i-V* response of 330 and 800 nm radii GNM, simulated potential profile in a 400 nm GNM, details of the finite-element simulation (parameters setting, geometry, mesh, *etc.*), the value of diffusion coefficient, viscosity and relative permittivity for DMSO/H_2O mixture, and electro-osmosis-induced ICR curve for 380 nm radius GNM are shown in Figure 2.7-2.14, respectively.

Figure 2.7 shows optical microscope images of a sharpened Pt wire sealed at the end of a glass capillary at different stages during the polishing process to expose a Pt disk. After removal of the Pt, the size of the nanopore was measure from the nanopore *i-V* response in an aqueous 1 M KCl solution. The relationship between the membrane resistance R_p and the small orifice radius is given by:

$$R_p = \frac{1}{\kappa a_p}\left(\frac{1}{\pi \tan\theta} + \frac{1}{4}\right) \tag{2.6}$$

where θ is half cone angle of the nanopore, κ is conductivity of the aqueous 1 M KCl solution, R_p is the resistance of the nanopore and a_p is the radius of the orifice of nanopore. [56] Herein, $\kappa = 0.1119\ \Omega^{-1}\text{cm}^{-1}$, θ is ~ 10^o and R_p is obtained from the slope of *i-V* response (Figure 2.8). The radius of the nanopore in Figure 2.8 was calculated to be 379 nm with a relative uncertainty of ~10%. *i-V* response for an 857 nm radius GNM (Figure 2.9) using the same experimental conditions as in Figure 2.1. NDR is not observed for the larger nanopore, most likely due to the larger pressure driven flow. Thus,

Figure 2.7. Optical microscope images of a sharpened Pt wire sealed at the end of a glass capillary at different stages during the polishing process to expose a Pt disk. (Note: the "two wires" in the third photo corresponds to a single folded wire.)

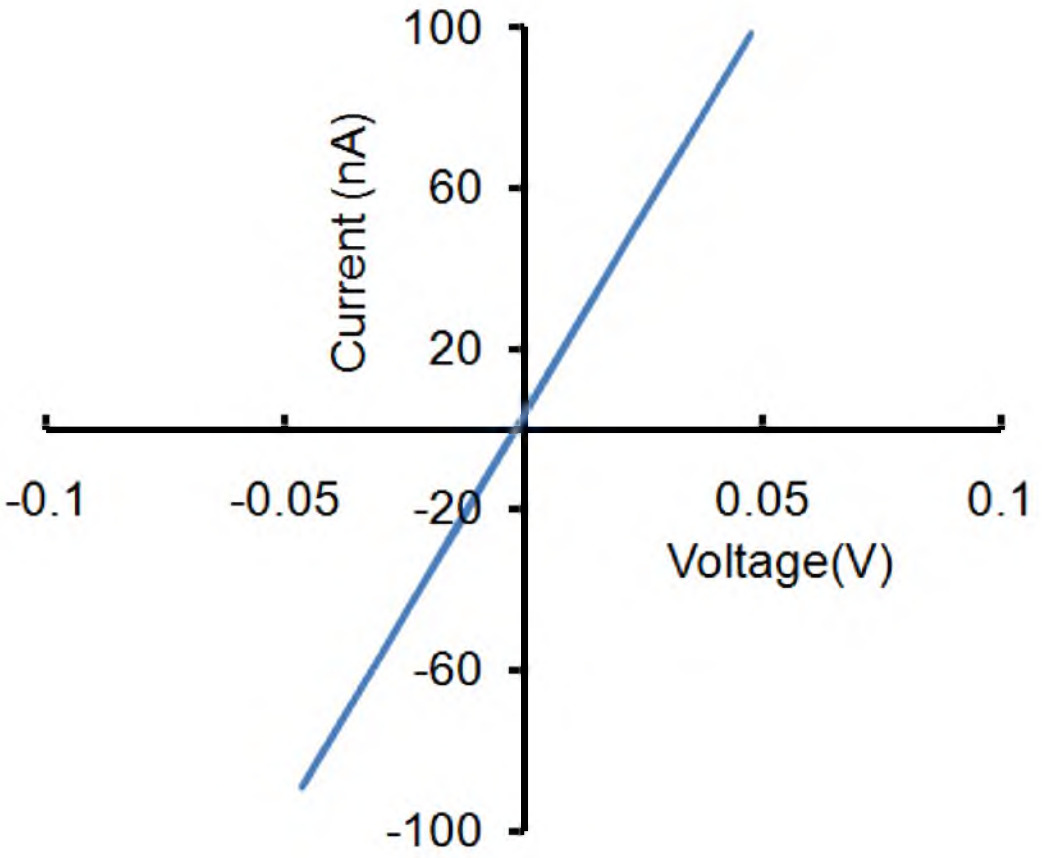

Figure 2.8. *i-V* response of the nanopore filled with and immersed in an aqueous 1 M KCl solution. The *i-V* response exhibits ohmic behavior in the 1 M KCl solution.

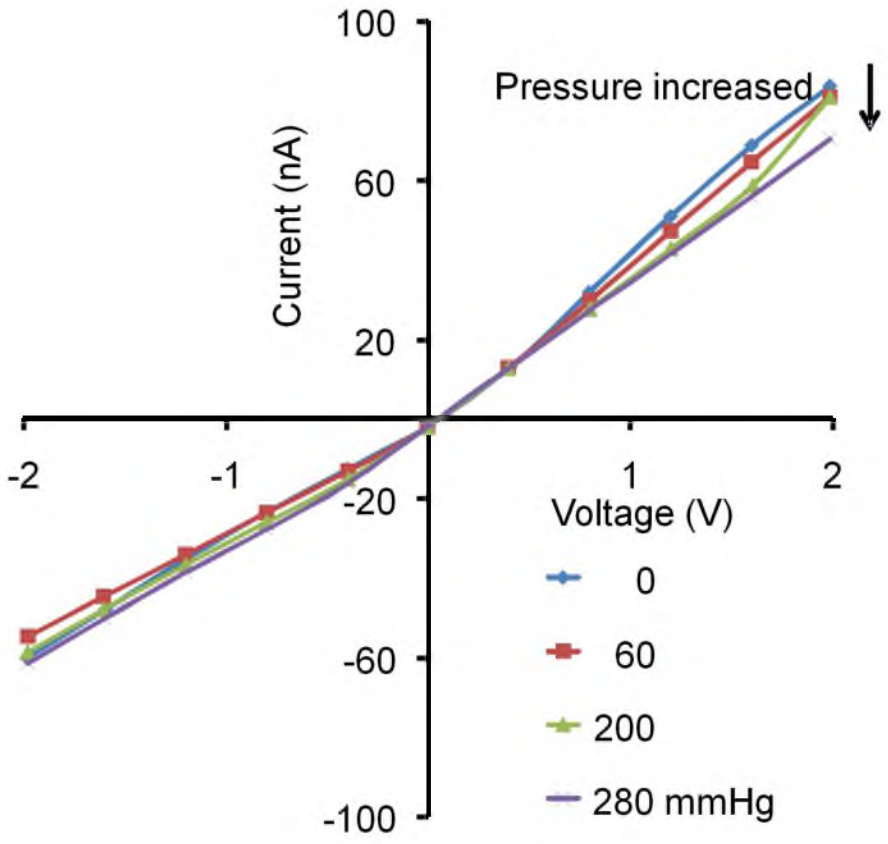

Figure 2.9. Experimental *i-V* responses of an 857 nm radius nanopore using an internal aqueous 5 mM KCl solution and an external DMSO/H_2O mixture (*v:v* 3:1) containing 5 mM KCl. Positive pressures were applied from 0 mmHg to 280 mmHg.

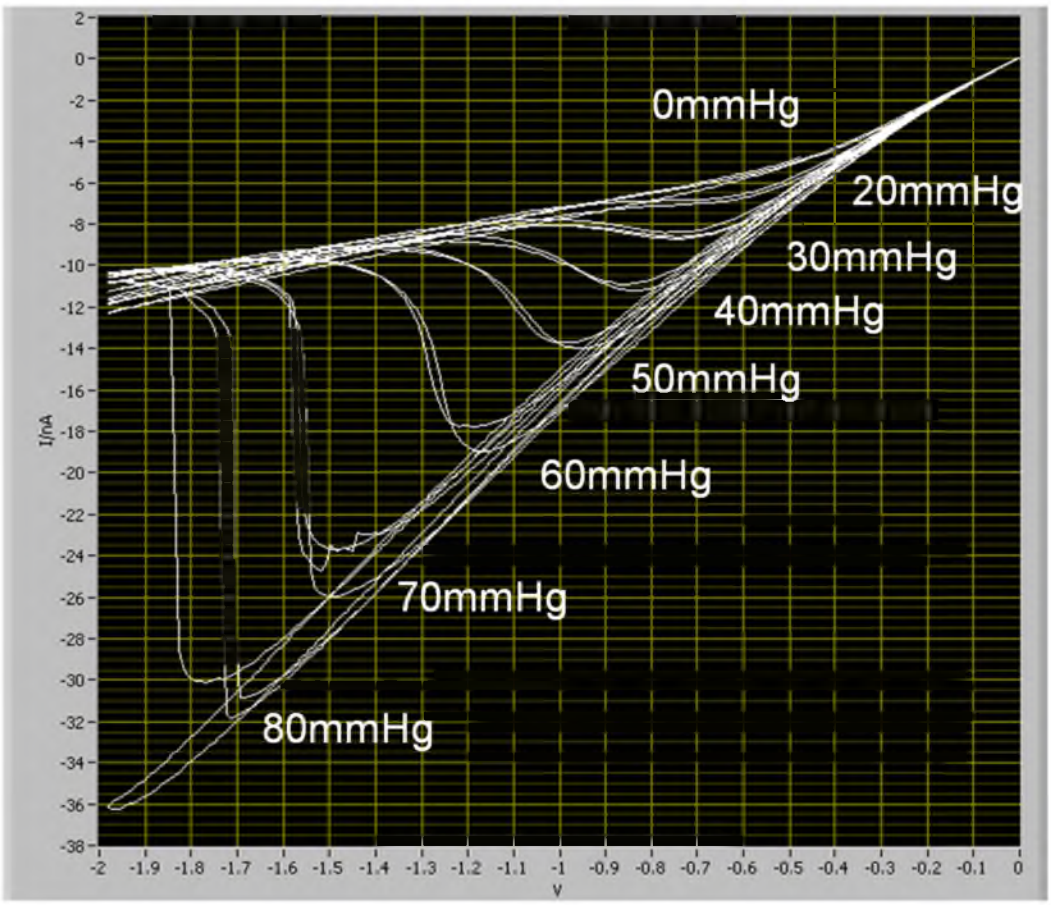

Figure 2.10. Experimental *i-V* responses of a 330 nm radius GNM with an internal aqueous 5 mM KCl solution and an external DMSO/water mixture (*v:v* 3:1) containing 5 mM KCl. A positive pressure (internal *vs.* external) ranging from 20 mmHg to 80 mmHg was applied across the GNM. Scan rate = 200 mV/s. The *i-V* curves show the forward and reverse scan responses at each pressure.

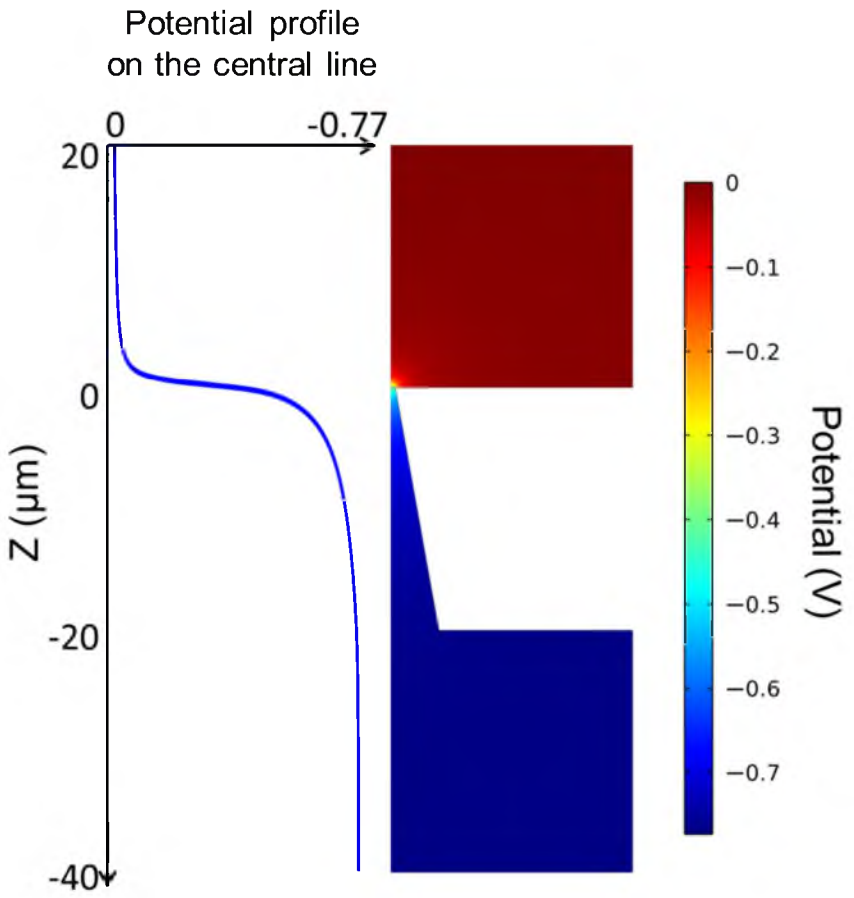

Figure 2.11. The steady-state potential profile along the center axis (left) and potential distribution (right) when -0.77 V is applied across a 400 nm radius GNM. Internal solution: 5 mM KCl in H_2O; external solution: 5 mM KCl in DMSO/H_2O.

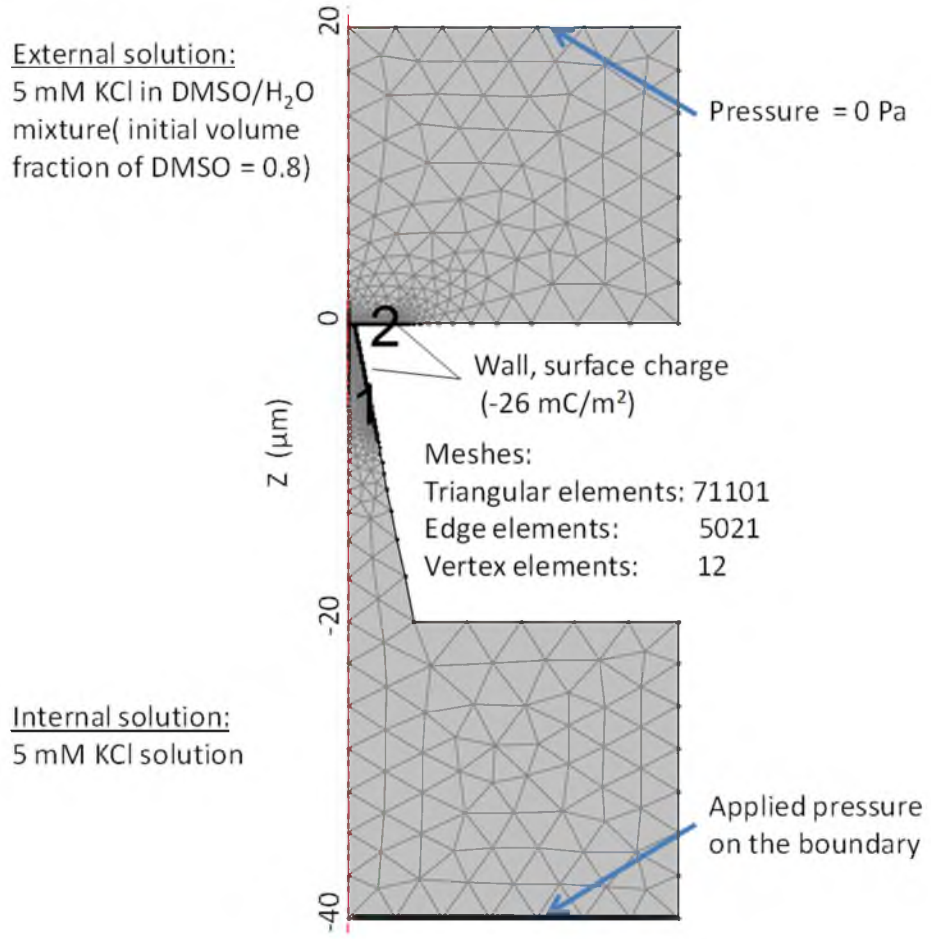

Figure 2.12. The 2D axial-symmetric geometry of the GNM and the mesh for the finite-element simulation (red dash line: the symmetry axis). The initial interface between the internal 5 mM KCl aqueous solution and the 5 mM KCl external DMSO/H_2O solution is located at the pore orifice, z = 0.

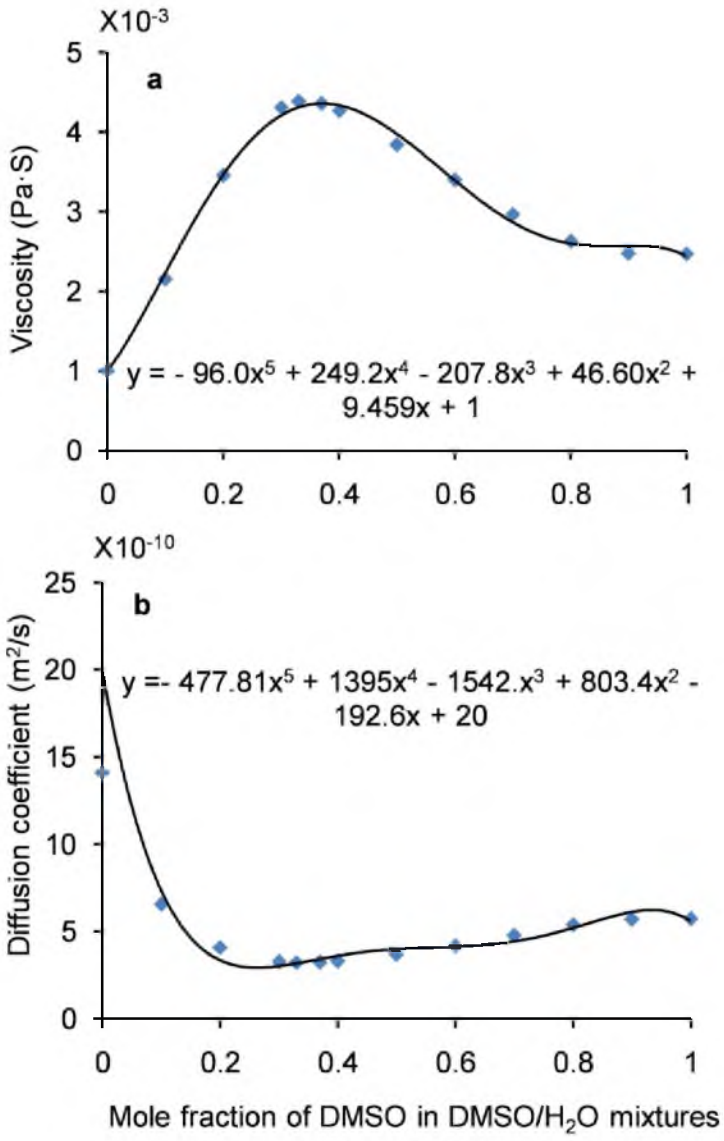

Figure 2.13. (a) Viscosity and (b) diffusion coefficients of K^+ and Cl^- in DMSO/H_2O mixtures. The diffusion coefficients of K^+ and Cl^- were calculated based on Stokes-Einstein equation (eq 2.3) using the values of viscosity reported in ref. 53 and are plotted. The polynomial fittings of data points shown on the graphs were used in the finite element simulation. In addition, in computing the potential and ion distributions, a linear relation between dielectric constant of the DMSO/H_2O mixture and the mole fraction of DMSO in the mixture was assumed, as described in ref. 54.

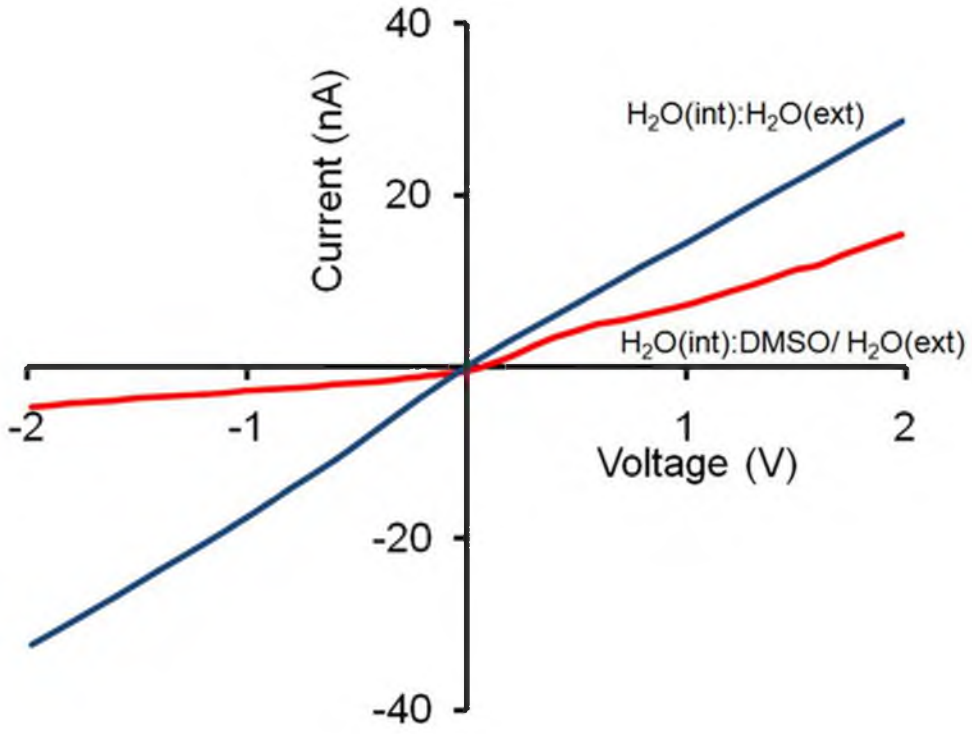

Figure 2.14. *i-V* responses of a 380 nm radius GNM at zero applied pressure. (A) Blue curve: internal and external aqueous solutions containing 5 mM KCl; (B) red curve: internal aqueous solution containing 5 mM KCl and external 3:1 (*v/v*) DMSO/H_2O mixed solution containing 5 mM KCl. The voltage was scanned from -2 to 2 V at a rate of 200 mV/s.

the external DMSO/H_2O solution is not driven into the nanopore and NDR behavior is not observed. Figure 2.10 shows the reproduction of NDR in a 330 nm radius GNM.

2.6 References

(1) Ridley, B.K. *Proc. Phys. Soc.* **1963**, *82*, 954-966.

(2) Esaki, L. *Phys. Rev.* **1958**, 603-604.

(3) Chen, J.; Reed, M.A.; Rawlett, A.M.; Tour, J.M. *Science* **1999**, *286*, 1550-1552.

(4) Quek, S.Y.; Neaton, J.B.; Hybertsen, M.S.; Kaxiras, E.; Louie, S.G. *Phys. Rev. Lett.* **2007,** *98*, 066807.

(5) Kannan, V.; Kim, M. R.; Chae, Y.S.; Ramana, C.V.; Rhee, J. K. *Nanotechonology* **2011**, *22*, 025705.

(6) Khoo, K. H.; Neaton, J. B. ; Son, Y.W.; Cohen, M.L; Louie, S.G. *Nano Lett.* **2008**, *8*, 2900-2905.

(7) Pickett, M. D.; Borghetti, J.; Yang, J. J.; Medeiros-Ribeiro, G.; Williams, R. S. *Adv. Mater.* **2011**, *23*, 1730-1733.

(8) Zeng, C.; Wang, H.; Wang, B.; Yang, J.; Hou, J. G. *Appl. Phys. Lett.* **2000**, *77*, 3595-3597.

(9) Buchs, G.; Ruffieux, P.; Groning, P.; Groning, O. *Appl. Phys. Lett.* **2008**, *93*, 073115.

(10) Lee, S. W.; Kornblit, A.; Lopez, D.; Rotkin, S. V.; Sirenko, A. A.; Grebel, H. *Nano Lett.* **2009**, *9*, 1369-1373.

(11) Li, J.; Zhang, Q. *Carbon* **2005**, *43*, 667-671.

(12) Pop, E.; Mann, D.; Cao, J.; Wang, Q.; Goodson, K.; Dai, H. *Phys. Rev. Lett.* **2005**, *95*, 155505.

(13) Kuznetsov, A. M. *J. Chem. Phys.* **2007**, *127*, 084710.

(14) Wu, Y.; Farmer, D. B.; Zhu, W.; Han, S.; Dimitrakopoulos, C.D.; Bol, A. A.; Avouris, P.; Lin, Y. *ACS Nano* **2012**, *6*, 2610-2616

(15) Migliore, A.; Nitzan, A. *ACS Nano*, **2011**, *5*, 6669-6685.

(16) Lan, W. J.; Holden, D. A.; Liu, J.; White, H. S. *J. Phys. Chem. C* **2011**,*115*, 18445-18452.

(17) Lan, W. J.; Holden, D. A.; Zhang, B.; White, H. S. *Anal. Chem.* **2011**, *83*, 3840-3847.

(18) Lan, W. J.; White, H. S. *ACS Nano* **2012**, *6*, 1757-1765.

(19) Holden, D. A.; Hendrickson, G. R.; Lan, W. J.; Lyon, L. A.; White, H. S. *Soft Matter.* **2011**, *7*, 8035-8040.

(20) Holden, D. A.; Watkins, J.J.; White, H. S. *Langmuir* **2012**, *28*, 7572-7577.

(21) Wei, C.; Bard, A. J.; Feldberg, S. W. *Anal. Chem.* **1997**, *69*, 4627-4633.

(22) Vlassiouk, I.; Kozel, T. R.; Siwy, Z. S. *J. Am. Chem. Soc.* **2009**,*131*, 8211-8220.

(23) Cervera, J.; Schiedt, B.; Ramirez, P. *Europhys. Lett.* **2005**, *71*, 35-41.

(24) He, Y.; Gillespie, D.; Boda, D.; Vlassiouk, I.; Eisenberg, R. S.; Siwy, Z. S. *J. Am. Chem. Soc.* **2009**, *131*, 5194-5202.

(25) Hou, X.; Guo, W.; Jiang, L. *Chem. Soc. Rev.*, **2011**, *40*, 2385-2401.

(26) Cheng, L.; Guo, L. J. *Chem. Soc. Rev.*, **2010**, *39*, 923-938.

(27) Perry, J. M.; Zhou, K.; Harms, Z. D.; Jacobson, S. C. *ACS Nano* **2010**, *4*, 3897-3902.

(28) Kovarik, M. L.; Zhou, K.; Jacobson, S. C. *J. Phys. Chem. B* **2009**, *113*, 15960-15966.

(29) Jin, P.; Mukaibo, H.; Horne, L. P.; Bishop, G. W.; Martin, C. R. *J. Am. Chem. Soc.* **2010**, *132*, 2118-2119.

(30) Woermann, D. *Phys. Chem. Chem. Phys.* **2003**, *5*, 1853-1855.

(31) Siwy, Z. S. *Adv. Funct. Mater.* **2006**, *16*, 735-746.

(32) Siwy, Z.; Heins, E.; Harrell, C. C.; Kohli, P.; Martin, C. R. *J. Am. Chem. Soc.* **2004**, *126,* 10850-10851.

(33) Vlassiouk, I.; Siwy, Z. S. Nanofluidic Diode. *Nano Lett.* **2007**, 7, 552-556.

(34) Yameen, B.; Ali, M.; Neumann, R.; Ensinger, W.; Knoll, W.; Azzaroni, O. *J. Am. Chem. Soc.* **2009**, *131*, 2070-2071.

(35) Ali, M.; Yameen, B.; Cervera, J.; Ramirez, P.; Neumann, R.; Ensinger, W.; Knoll, W.; Azzaroni, O. *J. Am. Chem. Soc.* **2010**, *132*, 8338-8348.

(36) Ali, M.; Nguyen, Q. H.; Neumann, R.; Ensinger, W. *Chem. Commun.* **2010**, *46*, 6690-6692.

(37) Guerrette, J. P.; Zhang, B. *J. Am. Chem. Soc.* **2010**, *132*, 17088-17091.

(38) Momotenko, D. and Girault, H. H. *J. Am. Chem. Soc.* **2011**, *133*, 14496-14499.

(39) Sa, N. Y.; Baker, L. A. *J. Am. Chem. Soc.* **2011**,*133*, 10398-10401.

(40) Sa, N. Y.; Fu, Y. Q.; Baker, L. A. *Anal. Chem.* **2010**, *82*, 9963-9966.

(41) Kubeil, C.; Bund, A. *J. Phys. Chem. C* **2011**, *115*, 7866-7873.

(42) White, H. S.; Bund, A. *Langmuir* **2008**, *24*, 2212-2218.

(43) Daiguji, H.; Yang, P.; Majumdar, A. *Nano Lett.* **2004**, *4*, 137-142.

(44) Daiguji, H.; Oka, Y.; Shirono, K. *Nano Lett.* **2005**, *5*, 2274-2280.

(45) Umehara, S.; Pourmand, N.; Webb, C. D.; Davis,R. W.; Yasuda, K.; Karhanek, M. *Nano Lett.* **2006**, *6*, 2486-2492.

(46) Karnik, R.; Duan, C.; Castelino, K.; Daiguji, H.; Majumdar, A. *Nano Lett.* **2007**, *7*, 547- 551.

(47) Siwy, Z. S.; Powell, M. R.; Kalman, E.; Astumian, R. D.; Eisenberg, R. S. *Nano Lett.* **2006**, *6,* 473-477.

(48) Siwy, Z. S.; Powell, M. R.; Petrov, A.; Kalman, E.; Trautmann, C.; Eisenberg, R. S. *Nano Lett.* **2006**, *6*, 1729-1734.

(49) Yusko, E. C.; An, R.; Mayer, M. *ACS Nano* **2010**, *4*, 477-487.

(50) Lan, W. J.; Holden, D. A.; White, H. S. *J. Am. Chem. Soc.* **2011**,*133*, 13300-13303.

(51) Zhang, B.; Galusha, J.; Shiozawa, P. G.; Wang, G.; Bergren, A. J.; Jones, R. M.; White, R. J.; Ervin, E. N.; Cauley, C. C.; White, H. S. *Anal. Chem.* **2007**, *79*, 4778-4787.

(52) Lee, S.; Zhang, Y.; White, H. S.; Harrell. C.C.; Martin, C. R. *Anal. Chem.*, **2004**, *76*, 6108-6115.

(53) Miao, W.; Ding, Z.; Bard, A. J. *J. Phys. Chem. B* **2002**, *106*, 1392-1398.

(54) Yang, L.; Yang, X.; Huang, K; Jia, G.; Shang, H. *Int. J. Mol. Sci.* **2009**, *10*, 1261-1270.

(55) Joseph, D.D.; Renardy, Y.Y. *Fundamentals of Two-Fluid Dynamics Part II: Lubricated Transport, Drops and Miscible Liquids*; Spring-Verlag: New York, **1992**, 324.

(56) White, R. J.; Zhang, B.; Daniel, S.; Tang, J. M.; Ervin, E. N.; Cremer, P. S.; White, H. S. *Langmuir* **2006**, *22*, 10777.

CHAPTER 3

CHEMICAL SENSING BASED ON NEGATIVE DIFFERENTIAL ELECTROLYTE RESISTANCE IN A SOLID-STATE NANOPORE

3.1 Introduction

Negative differential resistance (NDR) is used to describe electrical behavior where current decreases with an increasing applied voltage. One well-known NDR device is the Esaki or tunnel diode, where electron tunneling between the valence and conduction bands of a heavily doped p-n junction leads to a decrease of conductivity as the voltage is increased.[1] In this report, we describe NDR associated with a solid-state nanopore immersed in an aqueous solution. We describe the mechanism for this unusual electrolyte behavior, and demonstrated how NDR can be applied in chemical sensing.

The nonlinear current-voltage (*i-V*) behavior of geometrically asymmetric and electrically charged nanopores has been extensively investigated since the initial report of ion current rectification in glass pipettes by Wei, Bard and Feldberg.[2-1620] More recently, electro-osmotic and pressure-driven flows have been used to control electrolyte [21-24] or solvent flux[9, 25] and, thus, alter the nanopore conductance, with applications in the resistive-pulse detection of nanoparticles or macromolecules.[26 - 34] A solution flow-engendered NDR response in a conical shaped glass nanopore separating aqueous and

dimethylsulfoxide (DMSO) solutions containing equal concentrations of dissolved KCl was previously demonstrated by our laboratory.[35] A decrease in the electrical current in the nanopore was observed with increased applied voltage, a result of the voltage-dependent electro-osmotic flow (EOF) driving the external DMSO solution into the nanopore; the ion mobilities are lower in DMSO than water due to the much higher viscosity of DMSO. By varying the applied pressure across the nanopore, the voltage where NDR occurs was found tunable over a ~1 V range. An NDR-like response with ion current fluctuations was also reported by Siwy and coworkers for a polymer nanopore when a divalent cation (Ca^{2+}, Mn^{2+}) was present in solution and adsorbed to the interior nanopore surface. In contrast to EOF flow-induced NDR phenomenon described herein, this latter behavior was tentatively ascribed to voltage-dependent fluctuations in the local electrostatic potential resulting from transient binding of the dication.[36, 37]

In the chapter, NDR in a purely aqueous system is reported. A conical nanopore in a ~25 μm-thick glass membrane was used to separate aqueous solutions with two different KCl concentrations. In a typical experiment, the radius of the small orifice of the nanopore is ~300 nm; the internal solution within the nanopore contains 50 mM KCl and the external solution contains 5 mM KCl, as shown schematically in Figure 3.1a. After a pressure and a negative voltage are applied across the nanopore, a force balance is established, resulting in a steady-state electro-osmotic flow (white arrow) driving the lower concentration KCl solution into the nanopore while the pressure-driven flow (red arrow) pushes the higher concentration KCl solution out of the nanopore. At steady-state, the opposing pressure and electro-osmotic forces, along with the nanopore surface charge, determine the distribution of K^+ and Cl^- within the nanopore and, thus, the nanopore

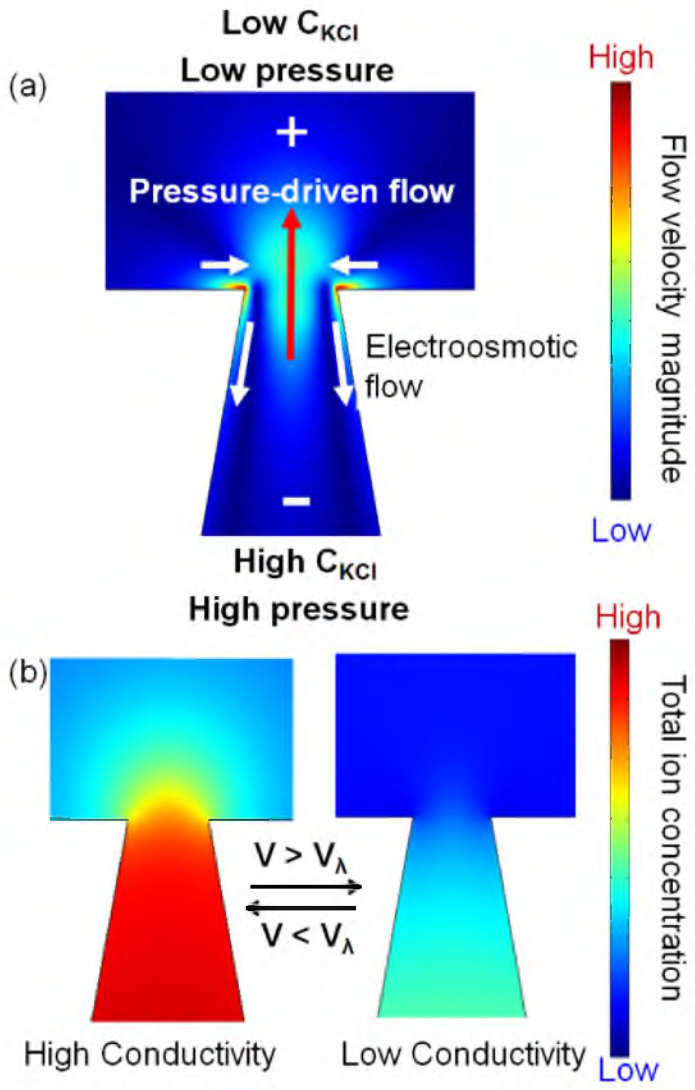

Figure 3.1.(a) Illustration of pressure-driven and voltage-engendered electro-osmotic flows that give rise to negative differential resistance (NDR) in the *i-V* response of a negatively charged, conical nanopore that separates high and low ionic strength solutions. The color surface indicates the magnitude of the net flow velocity; red and blue denote higher and lower velocities, respectively. Pressure-driven flow *out of the pore* occurs along the central axis of the nanopore (red arrow), while an opposing electro-osmotic flow (EOF) *into the pore* occurs along the negatively charged nanopore surface (white arrows). NDR observed in the *i-V* response of the nanopore results from positive feedback associated with an increase in EOF as the voltage is increased: an increased flux of the external low-conductivity solution into the nanopore orifice results in a decreased ionic conductivity of solution in the nanopore causing a further increase in EOF and a sudden drop in the nanopore conductivity at a critical voltage, V_λ. (b) Profiles of the total ion concentration (K^+ plus Cl^-) in the nanopore for applied voltages above ($V > V_\lambda$, high conductivity state) and below ($V < V_\lambda$, low conductivity state) the conductivity switching potential, V_λ.

conductivity. Qualitatively, and as shown in Figure 3.1b, by holding the pressure constant while increasing the applied voltage, the balance in flow within the nanopore shifts from an outward pressure-driven dominated flow at low voltages to an inward electro-osmotic dominated flow at high voltages. The change in flow direction results in a decrease of total ion (K^+ and Cl^-) concentration near the nanopore orifice, which further enhances the electro-osmotic flow into the pore. We demonstrate that the dependence of EOF on ion concentration creates a strong positive feedback mechanism between the nanopore flow and ion distributions, generating a bistability in the nanpore conductace. The switch from a high-conductance to low-conductance state at a critical potential, V_λ, occurs over a very narrow voltage range (< 2 mV) as demonstrated by the experimental results and finite element simulations described below. Because electro-osmotic flow depends strongly on the surface electrical charge density, V_λ is also very sensitive to the binding of charged analytes to the nanopore. This property of nanopore-based NDR is used to develop a new method of chemical detection.

3.2 Experimental section

3.2.1 Chemicals and materials

KCl, K_2HPO_4, KH_2PO_4, and $CaCl_2$ (all from Mallinckrodt chemicals) were used as received. All aqueous solutions were prepared using water (18 MΩ·cm) from a Barnstead E-pure H_2O purification system. Solution pH was buffered to a selected value with an appropriate ratio of K_2HPO_4 and KH_2PO_4, present at a combined concentration equal to 10% of the KCl concentration. For example, 100 mM KCl contains 10 mM K_2HPO_4 and KH_2PO_4 in total. All solution pHs were measured using a pH meter.

3.2.2 Glass nanopore membrane (GNM)

GNM preparation and sizing followed the procedures reported in Chapter 2. Four GNMs with orifice radii ranging from 260 to 470 nm were used in the experiments described herein.

3.2.3 Experimental set-up and data acquisition

A schematic diagram of the experimental set-up is presented in Figure 3.2. A glass capillary containing a glass nanopore membrane (GNM) at one end was used, as illustrated in the insert of Figure 3.2. The fabrication and sizing of GNMs followed procedures previously reported.[38] Four GNMs with orifice radii ranging from 260 to 470 nm were used in the experiments described herein. Pressure was applied across the nanopore using an airtight syringe connected to the capillary. A voltage was applied across the nanopore using two Ag/AgCl electrodes; one electrode is placed in the internal solution of the capillary, and the other in the external solution. The voltage between the two electrodes was scanned at a constant rate (10 mV/s) while measuring the current using a Dagan 2-electrode Voltammeter/Amperometer with a 10 kHz bandpass. A LabVIEW program was used to sample the current at a frequency of 10 kHz, and every 500 data points were averaged and used to construct D.C. *i-V* curves. For A.C. conductance measurements, a 1 kHz small-amplitude (10 mV) sine wave was superimposed on the slowly-varying D.C. voltage, and a Stanford Research Systems SR830 lock-in amplifier was used to separate the A.C. component from the total current. The root mean square (RMS) amplitude of the A.C. component was simultaneously recorded by the same LabVIEW program described above.

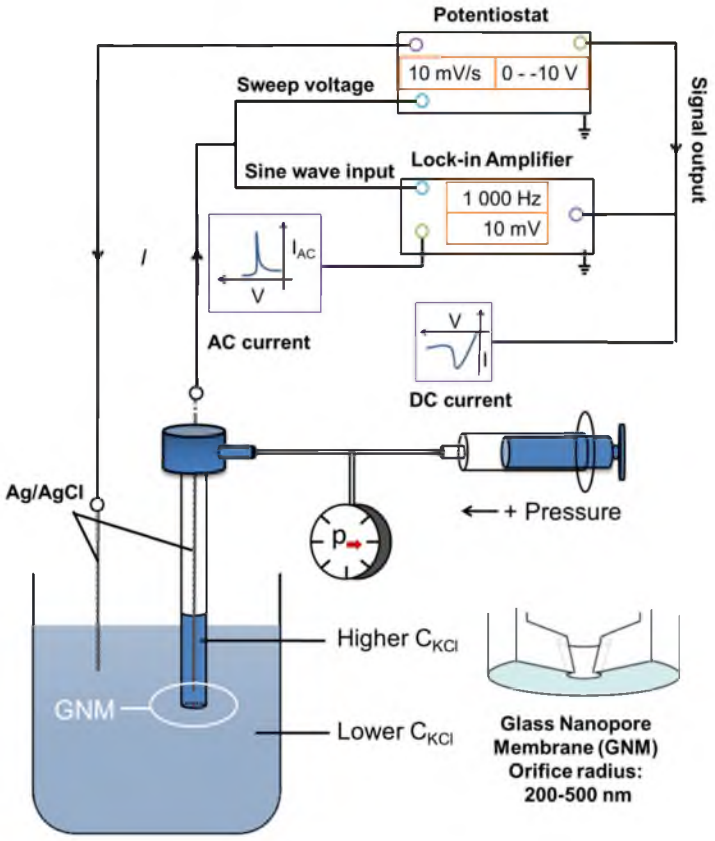

Figure 3.2. Schematic drawing of the experimental set-up. A glass nanopore membrane (GNM) at the end of a glass capillary separates the high (internal) and low (external) concentration KCl solutions. A positive pressure (inside *vs.* outside nanopore) is applied across the GNM to generate an outward pressure-driven flow. A 1 kHz, 10 mV (rms) sine wave superimposed on a slowly varying voltage (10 mV/s) is applied between the two Ag/AgCl electrodes located on opposite sides of the nanopore. The lock-in amplifier is used to analyze the A.C. component of the current.

3.2.4 Finite-element simulations

The finite-element simulations were performed using COMSOL Multiphysics 4.1 (Comsol, Inc.) to study the mechanism of NDR response as well as its sensitivity to surface charge density. Simulation details are provided in 3.5 Appendix.

3.3 Results and discussion

3.3.1 Negative Differential Resistance (NDR) in aqueous solutions

Glass membranes, ~25 μm-thick and containing a single conical nanopore with a half-cone angle of ~10°, as schematically shown in Figure 3.2, were synthesized at the end of a glass capillary. Aqueous solutions with different KCl concentrations were placed inside and outside the capillary, and a constant positive pressure and varying negative voltage were applied across the glass membrane. All values of applied pressure and applied voltage reported herein correspond to the values measured within the capillary relative to the external solution and are designated below as "internal *vs.* external." A lock-in amplifier interfaced to the potentiostat enables simultaneous recording of the A.C. and D.C. currents while slowly scanning the voltage across the nanopore, as discussed in a later section. Details of nanopore synthesis, instrumentation and data acquisition are provided in the Experimental section. Figure 3.3a shows a series of typical *i-V* curves exhibiting NDR for a 260-nm-radius nanopore containing a 50 mM KCl internal solution while varying the KCl concentration in the external solution between 5 and 25 mM. A constant pressure of 10 mmHg was applied across the nanopore while the voltage was scanned slowly in the negative direction at a rate of 10 mV/s. In general, the NDR switching potential is a strong function of the solution pH (*vide infra*); thus, the solutions

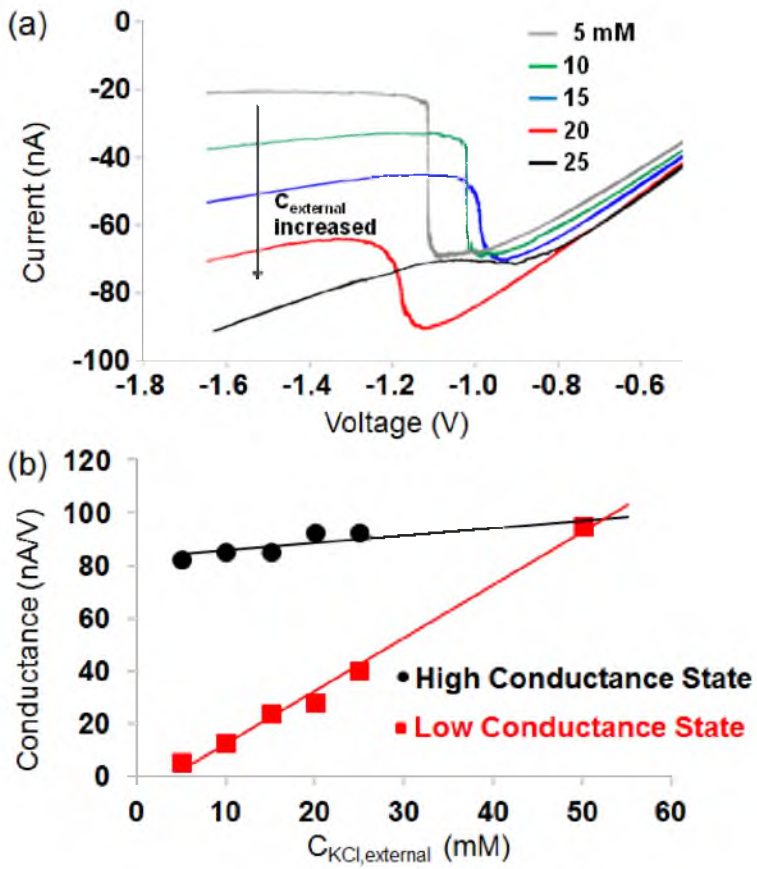

Figure 3.3. NDR behaviors in a nanopore. (a) A series of NDR curves as a function of the external KCl concentration measured using a 260-nm-radius nanopore. The KCl concentration of the external solution was varied between 5 and 25 mM KCl, while the internal KCl concentration (50 mM) was held constant; pH = 7.0. A 10 mmHg pressure (internal *vs.* external) was applied. (b) Conductance values measured from the slopes of *i-V* responses at voltages positive and negative of the NDR switching potential as a function of the external solution KCl concentration.

were buffered to 7.0 with an appropriate ratio of K_2HPO_4 and KH_2PO_4, present at a combined concentration equal to 10% of the KCl concentration. For example, the 50 mM KCl solution contains 5 mM K_2HPO_4 and KH_2PO_4 in total. All solution pHs were measured using a pH meter. As shown in Figure 3.3a, NDR behavior in the *i-V* response occurs between -1.0 and -1.1 V, approximately independent of the KCl concentration in the external solution. However, the width of the potential range of the transition between high and low conductance states increases from less than 10 mV when the external solution contained 5 mM KCl, to ~100 mV at 20 mM, and to ~200 mV at 25 mM.

The conductance of the nanopore, as measured from the slopes of the *i-V* curves in the *high* ($V > V_\lambda$) and *low conductance states* ($V < V_\lambda$) (abbreviated hereafter as HCS and LCS, respectively) is plotted in Figure 3.3b. The data indicate a HCS conductance of ~90 nA/V, approximately independent of the external KCl concentration. Conversely, the conductance of the LCS increases linearly with the concentration of external KCl bulk solution with a proportionality constant of ~1.8 nA/(V·mM).

Steady-state finite element simulations were performed in order to explore and understand the mechanism of NDR and its dependence on the KCl concentrations in the internal and external solutions, pore geometry, and nanopore surface charge density. The Nernst-Planck equation governing the diffusional, migrational and convective fluxes of K^+ and Cl^-, the Navier-Stokes equation for low-Reynolds number flow engendered by the external pressure and electro-osmosis, and Poisson's equation relating the ion distributions to the local electric field were simultaneously solved to obtain local values of the fluid velocity, ion concentrations, electric potential, and ion fluxes. The electrical current in the nanopore was obtained by integrating the ion fluxes over a cross-sectional

area of the nanopore. Simulation details including boundary conditions, mesh, parameter and constant setting are provided in 3.5 Appendix.

A simulated *i-V* response for a 260-nm-radius nanopore is shown in Figure 3.4, along with the volumetric flow rate (m^3/s) at the orifice and the total ion concentration profiles ($C_{K+} + C_{Cl-}$) for applied voltages between -0.4 and -1.4 V, while holding the pressure constant at 10 mmHg. The internal and external solution KCl concentrations were initially set to 50 mM and 5 mM, corresponding to the experimental *i-V* result (gray line) shown in Figure 3.3a. The simulation predicts an NDR switch at -1.256 V for a 5 mM KCl external solution, in a reasonable agreement with the experimental measurement (V_λ = -1.11 V). Figure 3.4c shows that the total ion concentration in the nanopore decreases from ~70 mM at -0.4 V to ~35 mM at -1.4 V, dropping suddenly within a narrow potential range between -1.256 and -1.258 V. Finite-element simulations of the nanopore system failed to converge within this narrow voltage window, suggesting that a stable fluid-flow and conductance state does not exist between the HCS and LCS.

The simulated *i-V* curve suggests that NDR represents a sudden transition between high and low conductance states that is associated with a bistability in the electrolyte flow within the nanopore. As schematically illustrated in Figure 3.1, the ion concentration distribution is determined by the combination of the constant outward pressure-driven flow and the voltage-dependent inward electro-osmotic flow. The simulated flow rate at the orifice shown in Figure 3.4b provides a more quantitative view of the voltage dependent flow within the nanopore. At potentials positive of ~-1.1 V, the flow is directed outward from the nanopore (represented by a positive sign) and its magnitude is linearly correlated with the potential, a consequence of increasing electro-

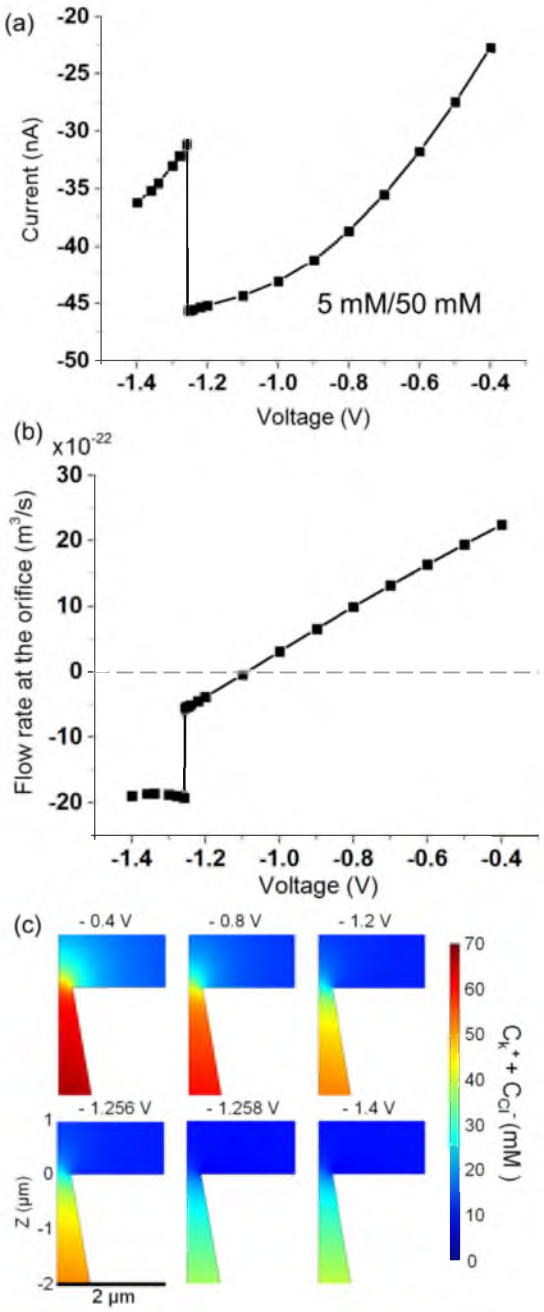

Figure 3.4. Simulation of NDR behavior in a nanopore. (a) Simulated *i-V* curve of the 260-nm-radius nanopore with an external KCl concentration of 5 mM and an internal KCl concentration of 50 mM (corresponding to the experimental data (gray line) in Figure 3.3a). A pressure of 10 mmHg and a surface charge density of -12.5 mC/m^2 were used in the simulation. (b) The corresponding solution volumetric flow rate at the orifice as a function of the applied voltage. Negative values of flow rate correspond to solution flow from the bulk solution into the nanopore. (c) The total ion concentration profiles ($C_{K^+} + C_{Cl^-}$) as a function of applied voltage.

osmotic flow offsetting pressure driven flow. Between -1.1 V and -1.256 V (the latter potential corresponding to the NDR switching potential, V_λ), the flow switches direction and the external solution flows into the nanopore at a low flow rate. In this range, the ion concentration at the orifice decreases gradually while the current continues to increase (Figure 3.4a and Figure 3.4c). A further increase of voltage beyond -1.256 V, however, results in a sudden and significant decrease in the ion concentration, and a large sudden increase and decrease, respectively, in the inward electro-osmotic flow and electrical current.

We propose that the discrete jumps in flow and current result from a feedback mechanism between the ion concentrations and electro-osmotic flow, as qualitatively depicted in Figure 3.5. At potentials positive of the NDR switching potential, V_λ, scanning the applied voltage to more negative potentials results in elecroosmotic flow bringing in external solution, resulting in a decrease in the ion concentration within the nanopore orifice. This decrease in ion concentration results in an increased thickness of the electrical double layer, generating a more negative potential of the nanopore surface if the surface charge density σ remains constant, as described by the Grahame equation.[39]

$$\sigma = \sqrt{8c_0 \varepsilon RT}\sinh\left(\frac{e\psi_d}{2k_B T}\right) \tag{3.1}$$

In eq 3.1, ψ_d is the diffuse layer potential near the charged surface, c_0 is the bulk concentration of a symmetric monovalent electrolyte, e is the absolute value of elementary charge (-1.60×10^{-19} C), R is the gas constant, ε is the solution permittivity, T is the absolute temperature of 298 K, and k_B is the Boltzmann constant.

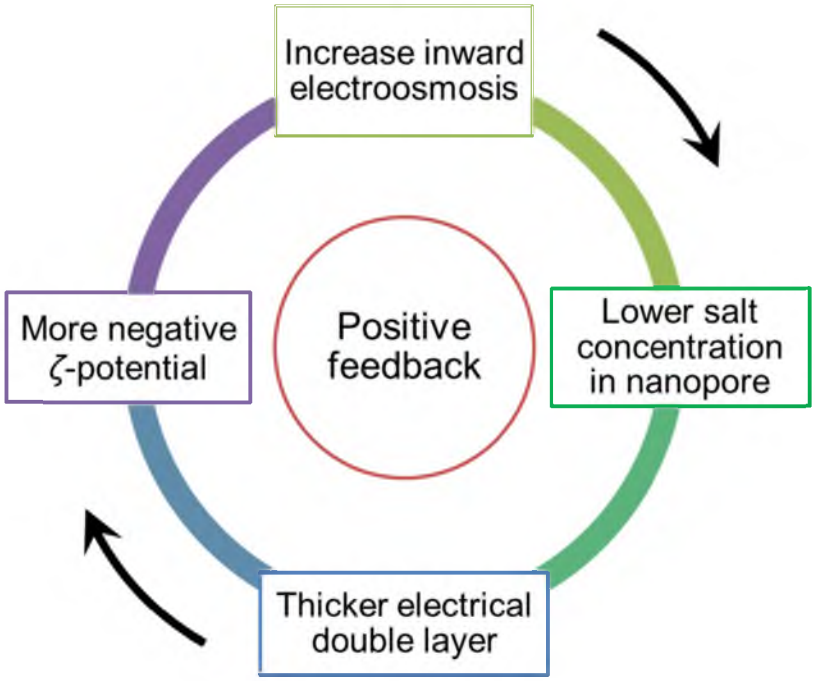

Figure 3.5. Positive feedback mechanism associated with the NDR switch.

The electro-osmotic velocity, u, in turn, is proportional to the value of zeta potential, ζ, at the velocity slip plane located adjacent to the nanopore surface. The Helmholtz-Smoluchowski equation relates the effective slip electro-osmotic velocity to ζ,

$$u = -\frac{\varepsilon \zeta E}{\eta} \tag{3.2}$$

where E is the electric field parallel to the surface, and η is the viscosity of the fluid. The parameters ψ_d and ζ have slightly different physical interpretations as discussed by Probstein,[40] but approximately similar values and a similar dependence on electrolyte concentration. Thus, the increase in ζ (and ψ_d) resulting from the decrease in ion concentration at the orifice (resulting from the inward electro-osmotic flow) further enhances the inward electro-osmotic flow of the low conductivity solution into the nanopore. This dependence of the inward electro-osmotic flow on the ion concentration, *via* the electrical double layer structure, forms a positive feedback loop between conductance and electro-osmotic flow (Figure 3.5), leading to a sudden increase of flow rate (from -5×10^{-22} m^3/s to -20×10^{-22} m^3/s), a drop of concentration (from ~50 mM to ~30 mM), and a decrease in current (-46 nA to -30 nA) between -1.256 and -1.258 V, as shown in Figure 3.4. We note that the use of the Helmholtz-Smoluchowski equation to describe electro-osmotic flow in a conical nanopore is, of course, approximate, and is used here as a semiquantitative prediction of the dependence of flow velocity on ion concentration.

For an external KCl concentration of 25 mM, the ion concentration gradient at the nanopore orifice is smaller, and the total ion concentration decreases gradually, resulting in a slightly curved *i-V* response rather than exhibiting a sharp NDR response (experimental: black line in Figure 3.3a; the corresponding simulated result is provided in 3.5 Appendix). For extremely low external KCl solution concentrations (*e.g.*, < 1 mM), an NDR switch was not consistently observed. The reason remains unclear, and a similar finite element simulation was conducted to investigate this scenario, also given in 3.5 Appendix. These results indicate that an appropriate concentration difference between the external and internal solutions is essential to generate a sudden NDR switch between high and low conductance states.

3.3.2 Chemical sensing based on NDR

As described above, the NDR conductivity switch originates from the interdependence of ion concentration and electro-osmotic flow at the nanopore orifice. Thus, the electro-osmotic flow in a nanopore is a function of ζ-potential or surface charge density of the glass nanopore (σ), suggesting a dependence of the NDR switching voltage (V_λ) on the surface charge density. Figure 3.6 shows simulated NDR curves for different surface charge densities, σ, demonstrating that V_λ is indeed strongly dependent on σ, shifting to more positive voltages with increasing negative charge density. Physically, a larger negative charge density leads to stronger electro-osmotic flow at less negative voltages, leading to the shift in NDR. Experimentally, the nanopore surface charge density can be adjusted by adsorption of ions, *e.g.*, the addition of multivalent ions to the solution, or by adjusting the pH of the solutions due to the acid/base equilibrium of the

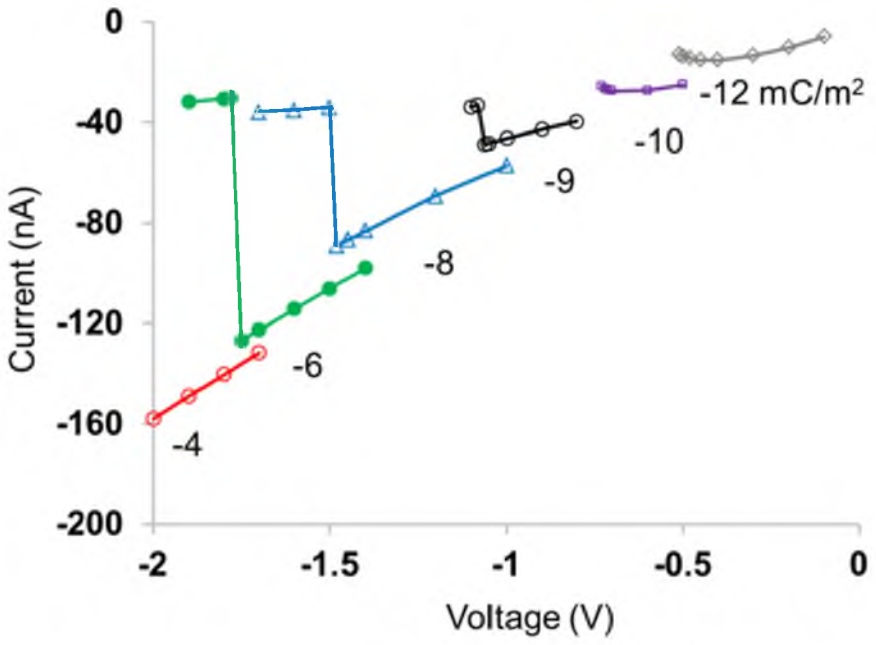

Figure 3.6. Simulated NDR curves for a 260-nm-radius nanopore at 5 mmHg pressure as a function of nanopore surface charge density. The simulation corresponds to 50 (internal) and 5 mM (external) KCl solutions.

silanol groups at the glass surface. These chemistries will be employed to demonstrate potential applications of solid state nanopore NDR in chemical sensing.

Because Ca^{2+} binds more strongly than K^{+} to the dissociated silanol group,[37, 41] the addition of Ca^{2+} to the KCl solutions reduces the negative surface charge density at the glass nanopore surface, resulting in a predicted shift of the NDR curve to a more negative voltage based on Figure 3.6. To rule out any interference from the change in the electrolyte concentration as Ca^{2+} is added to the solution, both the internal and external solutions contained relatively high concentrations of KCl (1 M and 100 mM, respectively). When 2 mM $CaCl_2$ was added to the external 100 mM KCl solution, the NDR curve shifted ~1 V to a more positive potential as shown in Figure 3.7. The NDR curve recovered to the original position when the solution containing Ca^{2+} was replaced by the original solution containing only KCl. The shift recorded with and without Ca^{2+} was reproduced over several cycles. Although the addition of Ca^{2+} results in a slight decrease in the solution pH from 7.8 to 7.5 due to the hydrolysis of Ca^{2+}, the shift in the NDR switching potential is mainly caused by the Ca^{2+} binding and not to the small change in solution pH; as shown, NDR is weakly dependent on the solution pH in neutral or slightly basic solutions.

Similarly, as the pH of the solution increases, the silanol acid-base equilibrium shifts toward the dissociated state leading to an increase of surface charge density. This increase in surface charge density results in a stronger electro-osmotic flow and, thus, should cause a negative shift in V_{λ}.

Phase-sensitive detecting using a lock-in amplifier was used to measure the change in A.C. conductivity of the pH-dependent NDR curves and locate the V_{λ}.[42-46] A 1

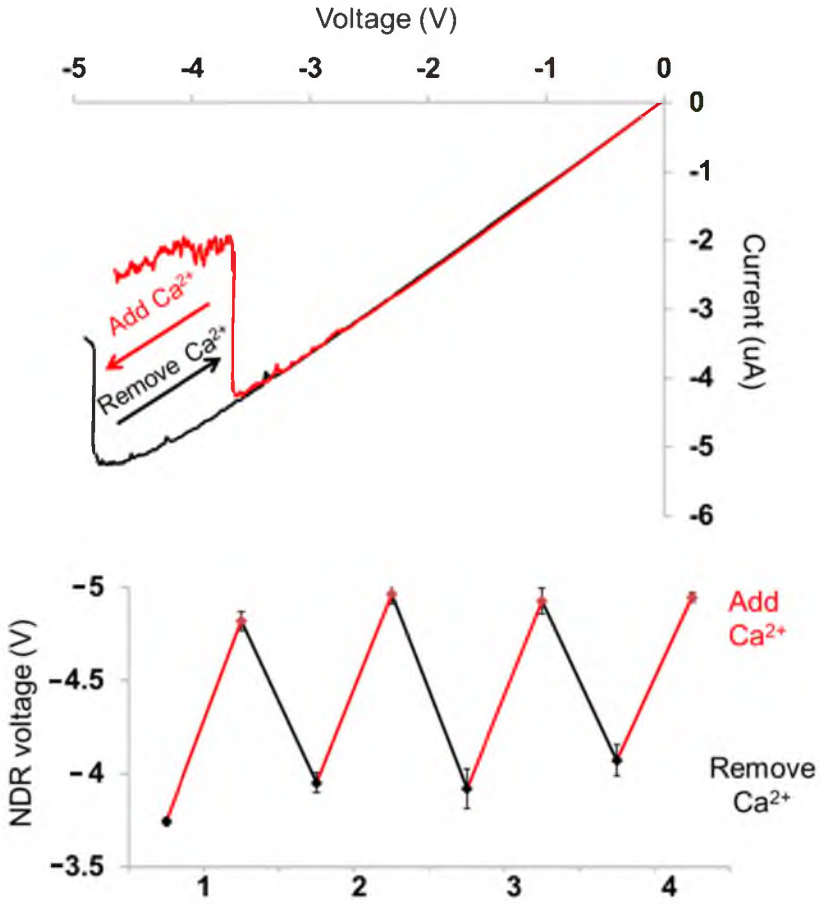

Figure 3.7. Reversible NDR response to Ca^{2+} in the external electrolyte solution for a 270-nm-radius nanopore. Experimental conditions: 54 mmHg; 1 M internal and 100 mM external KCl solutions; pH = 7.8; Ca^{2+} concentration (when present in solution) = 2 mM; scan rate: 100 mV/s.

kHz low amplitude (rms = 10 mV) sine wave was applied to the slowly varying D.C. voltage (10 mV/s), and the A.C. component i_{AC} at 1 kHz was recorded. Figure 3.8 shows the A.C. and D.C. NDR signal simultaneously recorded for a 470-nm radius nanopore at 8 mmHg pressure. Physically, i_{AC} corresponds to the magnitude of the differential change in conductance, yielding a sharp peak in the A.C. conductivity at the NDR switching potential of ~3.7 V as shown in Figure 3.8. The i_{AC} peak current of 4500 nA is approximately equal to the decrease of ~4200 nA observed in the D.C. NDR *i-V* response, indicating that the redistribution of the ion concentrations between a high conductivity state and a low conductivity state tracks the 1 kHz modulation.

Figure 3.9a shows the A.C. conductance of the nanopore at different solution pHs. The NDR switching potential (V_λ) shifts from -2.83 ± 0.03 V at pH = 8.9 to -6.1 ± 0.5 V at pH = 4.9 (standard deviation of V_λ is based on more than three measurements at each specific pH). As seen from the data, the conductivity switching potential V_λ is extremely sensitive to pH, obtaining a sensitivity of ~4 V per pH in slightly acidic solutions.

To quantify the relation between V_λ and pH, the interfacial model of Behrens and Grier's was used to estimate the glass surface charge density based on solution pH.[47] Surface charge density was obtained by solving eq 3.3, which was derived from the Stern layer's phenomenological capacity, the Poisson-Boltzmann equation and the surface silanol dissociation equilibrium, and the Grahame equation (eq 3.1).

$$\psi_d(\sigma) = \frac{RT}{F}\ln\left(\frac{-\sigma}{e\Gamma + \sigma}\right) - (pH - pK)\frac{RT}{F}\ln 10 - \frac{\sigma}{C} \qquad (3.3)$$

ψ_d, as defined in eq 3.1, is the diffuse layer potential which is a function of

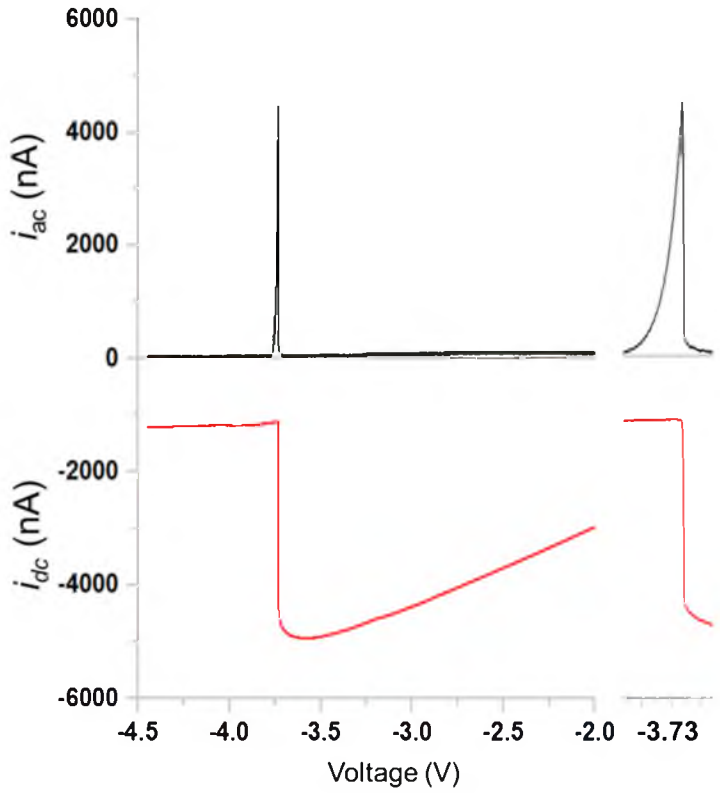

Figure 3.8. D.C. and A.C. NDR signals recorded simultaneously using a potentiostat and lock-in amplifier for a 470-nm-radius glass nanopore at pH 7.2, 8 mmHg and a scan rate of 10 mV/s. KCl solution concentrations: 0.1 M external and 1 M internal. On the right is the expansion of the NDR switching region.

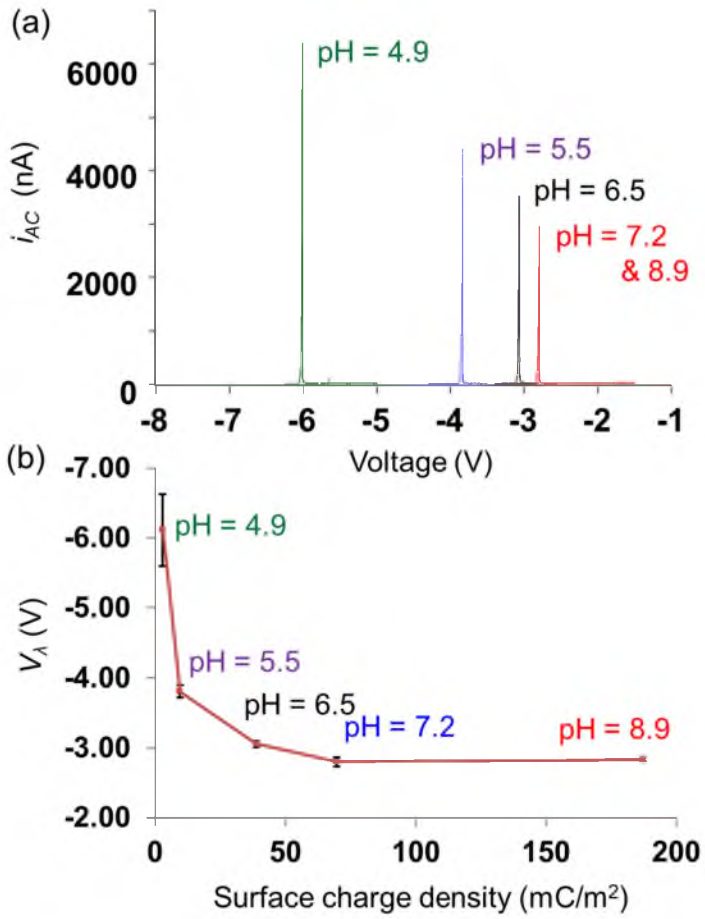

Figure 3.9. pH-dependence study. (a) pH-dependent NDR behavior for a 370-nm-radius nanopore. Pressure: 80 mmHg; KCl solution concentrations: 0.1 M external and 1 M internal; 10 mV/s scan rate; 1 kHz and 10 mV (rms) sine wave. (b) Dependence of conductivity switching potential on surface charge density, estimated from eqs 3.1 and 3.3.

surface charge density σ, Γ is the surface concentration of silanol groups on the glass chosen as 8 per nm^2. pK is the dissociation constant of 7.5, C is the Stern layer's phenomenological capacity of 2.9 F/m^2, F is the Faraday's constant. All values listed above were reported and derived by Behrens and Grier.[47]

Figure 3.9b shows the dependence of V_λ on the corresponding pH values, and the computed values of σ from the Behrens and Grier model. As the pH decreases from 5.5 to 4.9, the surface charge density decreases from 9.5 to 2.9 mC/m^2. Electro-osmotic flow in the nanopore is dominated by electric forces generated by the charged surface at the nanopore orifice, as shown in Figure 3.1 and, for the purpose of analytical sensing, this region is defined as the sensing zone surface, Based on finite element simulations, we estimate this region to have an area of ~1.5 μm^2 for a 370 nm-radius nanopore (detailed in 3.5 Appendix). Thus, as the pH is lowered from 5.5 to 4.9, the computed decrease in surface charge density from 9.5 to 2.9 mC/m^2 corresponds to a decrease of ~60,000 elementary surface charges responsible for the observed shift in V_λ of 2.29 V. Assuming the ability to measure a 10 mV change in V_λ, the NDR measurement sensitivity is on the order of *~300 elementary charges.* Although approximate, this calculation suggests a future application of nanopore NDR for the detection of a very small number of analyte molecules.

3.4 Conclusions

In summary, we have reported NDR behavior in the *i-V* response of a charged glass nanopore membrane that separates two solutions containing different concentrations of KCl. NDR results from a competition between an inward (voltage-independent)

pressure-driven flow and outward (voltage-dependent) electro-osmotic flow, leading to a voltage-dependent ion distribution at the nanopore orifice. A very narrow NDR response, indicating a bistability between high conductivity and low conductivity states, was achieved by adjusting the relative concentrations of KCl in the external and internal solutions. The narrow NDR switch between conduction states was shown to result from positive feedback between electro-osmotic flow and the surface potential of the nanopore. The switching potential where NDR occurs (V_λ) was shown to be very sensitive to the surface charge density by finite element simulations and experimentally demonstrated by measurement of the dependence of V_λ on pH and Ca^{2+} concentration. The high sensitivity of V_λ on surface charge suggests possible applications of NDR in chemical sensing.

3.5 Appendix

In this Appendix, the *i-t* recording of the NDR response for a 350-nm radius nanopore is provided in Section 3.5.1. Section 3.5.2 provides the detail of the finite element simulations including parameters setting, geometry, mesh, *etc.*, as well as the simulated *i-V* responses and ion concentration profiles for a 260-nm-radius nanopore at large and small salt concentration gradients (50 mM KCl inside/1 mM KCl outside; 50 mM KCl inside/25 mM KCl outside, respectively). Section 3.5.3 shows the estimation of sensing zone surface area at the nanopore orifice.

3.5.1 *i-t* recording of NDR response and NDR curves as a function of solution pH

Figure 3.10 shows the *i-t* recording of NDR response for a 350-nm-radius pore.

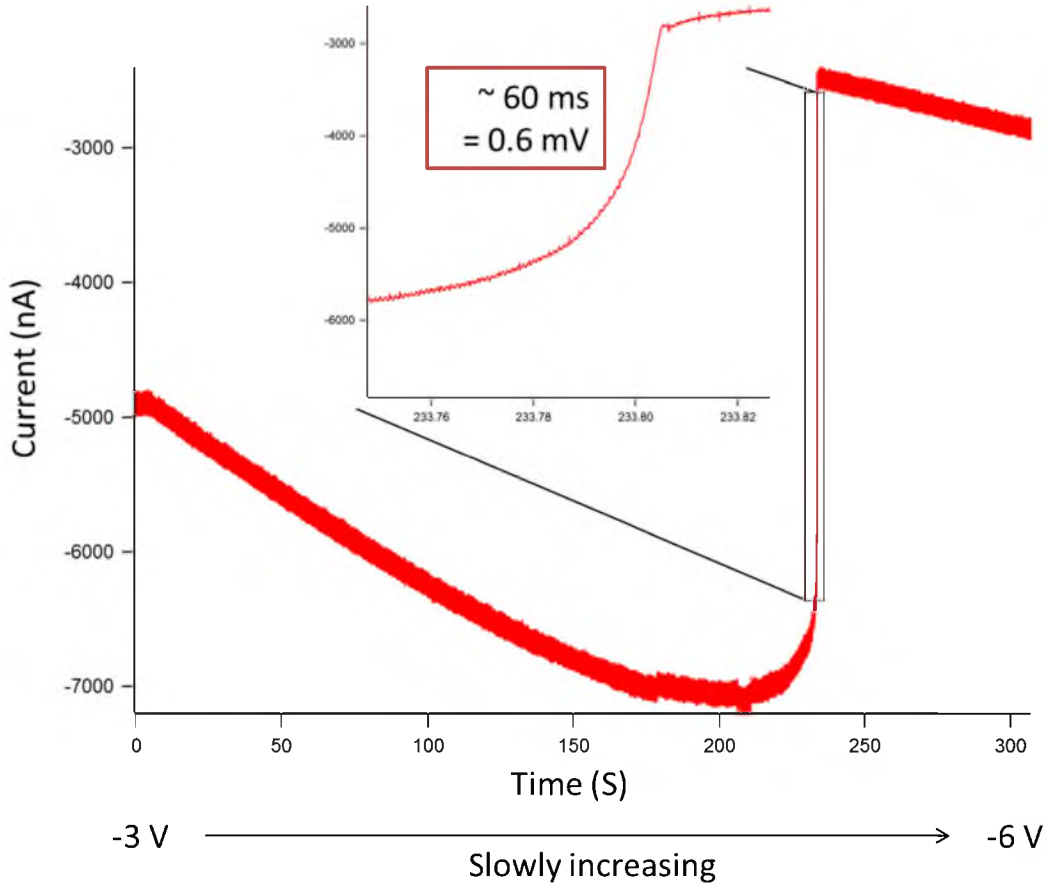

Figure 3.10. *i-t* trace recorded at a data acquisition rate of 50 kHz while scanning the voltage at 10 mV/s from -3 V to -6 V across a 350-nm-radius nanopore. The internal and external KCl solution concentrations are 1 M and 100 mM, respectively. The pressure is 80 mmHg; pH = 4.9. The insert shows switch completed within ~60 ms or ~0.6 mV. The temporal resolution of the measurement is limited by the instrumentation bandwidth of ~20 kHz.

3.5.2 Finite element simulation

Steady-state finite element simulations using COMSOL Multiphysics were performed to provide a quantitative model of the NDR response. A description of ion and solvent transport in the nanopore begins with the Navier-Stokes equation to describe pressure and electric force driven flow.

$$\mathbf{u}\nabla\mathbf{u} = \frac{1}{\rho}(-\nabla p + \eta\nabla^2\mathbf{u} - F(\sum_i z_i c_i)\nabla\Phi) \tag{3.4}$$

In eq 3.4, **u** and Φ are the local position-dependent fluid velocity and potential, ρ and η are the density and viscosity of the fluid, respectively, c_i and z_i are concentration and charge of the species i in solution, p is the pressure and F is the Faraday's constant. For computational simplicity, we assume a constant value for ρ of 1000 kg/m^3 and η of 0.001 Pa•s. The ion fluxes are described by the Nernst-Planck equation.

$$\mathbf{J}_i = -D_i\nabla c_i - \frac{Fz_i}{RT}D_i c_i\nabla\Phi + c_i\mathbf{u} \tag{3.5}$$

In eq 3.5, $\mathbf{J}_i$ and D_i, are, respectively, the ion flux vector and the diffusion coefficient of species i in solution, and T is the absolute temperature. D_{K^+} = 1.957 x 10^{-9} m^2/s and D_{Cl^-} = 2.03 x 10^{-9} m^2/s.[23] The absolute temperature T = 298 K, and the gas constant R = 8.314 J/K. The relationship between the local ion distribution and potential is described by Poisson's equation, eq 3.6

$$\nabla^2\Phi = -\frac{F}{\varepsilon}\sum_i z_i c_i \tag{3.6}$$

where ε is the permittivity of the solution. Simultaneously solving eqs 3.4 to 3.6 by finite element method yields the ion distribution, potential distribution, velocity field, and the total flux of ions. The current resulting from the ion fluxes was computed by integrating the ion fluxes over a cross-sectional area of the pore. Simulations were performed at different applied voltages to obtain a simulated *i-V* response. Figure 3.11 shows the details of the simulation geometry and boundary conditions.

Based on the model described above, Figure 3.12 shows the simulated *i-V* response and the corresponding total ion concentration profiles near the nanopore orifice as a function of voltage for 25 mM (external) and 50 mM (internal) KCl solutions. No NDR occurs due to the small concentration gradient not being able to achieve significant change in the conductivity as voltage increases. In the case of 1 mM (external) and 50 mM (internal) KCl solution, the expected NDR switching does not occur, but rather a slightly curved *i-V* response is observed. Experimentally, we observed this latter behavior for the majority of the time; occasionally a NDR switch was observed. The reason why NDR does not always occur at very low *external* KCl concentration remains unclear; one possible explanation is that electro-osmotic flow in the center of the nanopore increases as the voltage increases, driving the higher concentration salt solution out of the nanopore orifice.[23] Therefore, a negative feedback is established that results in increased outflow as the voltage increases. This outward flow prevents the external low concentration from flowing into the orifice to create a low conductivity state. Figure 3.13 shows the simulated results.

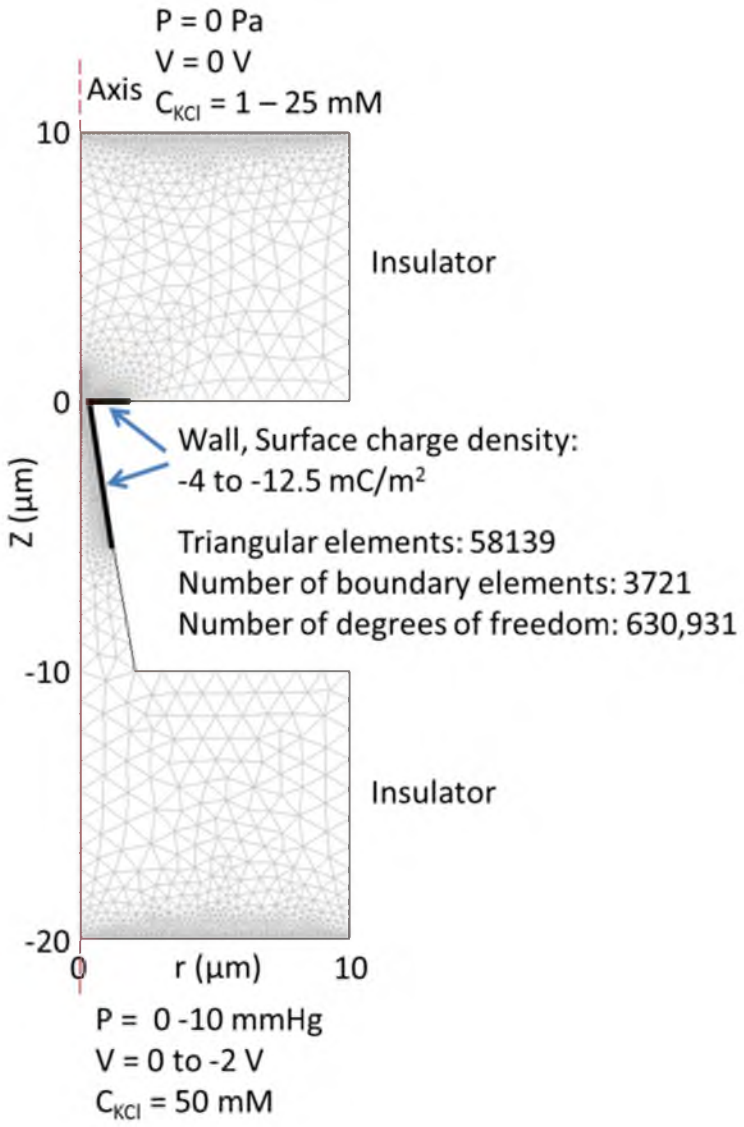

Figure 3.11. The 2D axial-symmetric geometry of the glass nanopore with a radius of 260 nm and the mesh used for the finite-element simulation (the red dash line corresponds to the axis of symmetry). The surface charge density was varied to match the experimental results (Figure 3.3 and Figure 3.4) for a 260-nm-radius glass nanopore (-12.5 mC/m^2). The initial concentration of KCl within the solution domain was set to 50 mM. Pressure, concentration, and voltage boundary conditions, corresponding to the bulk values of the internal and external solutions are shown in the figure.

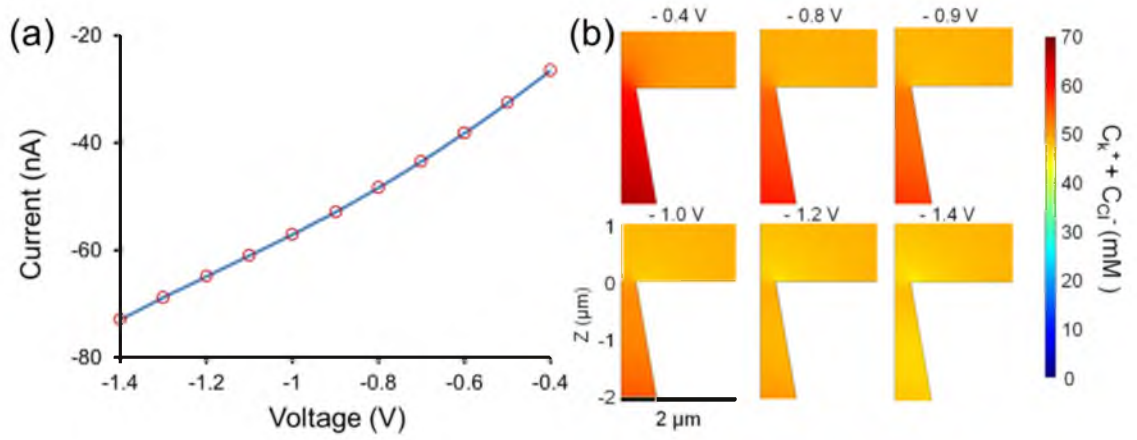

Figure 3.12. Simulation for 25 mM (external) and 50 mM (internal) KCl solutions. (a) Simulated *i-V* response for a 260 nm radius nanopore (external solution: 25 mM KCl and internal solution: 50 mM KCl; 10 mmHg). (b) Simulated total ion distribution near the nanopore orifice at voltages from -0.4 to -1.4 V.

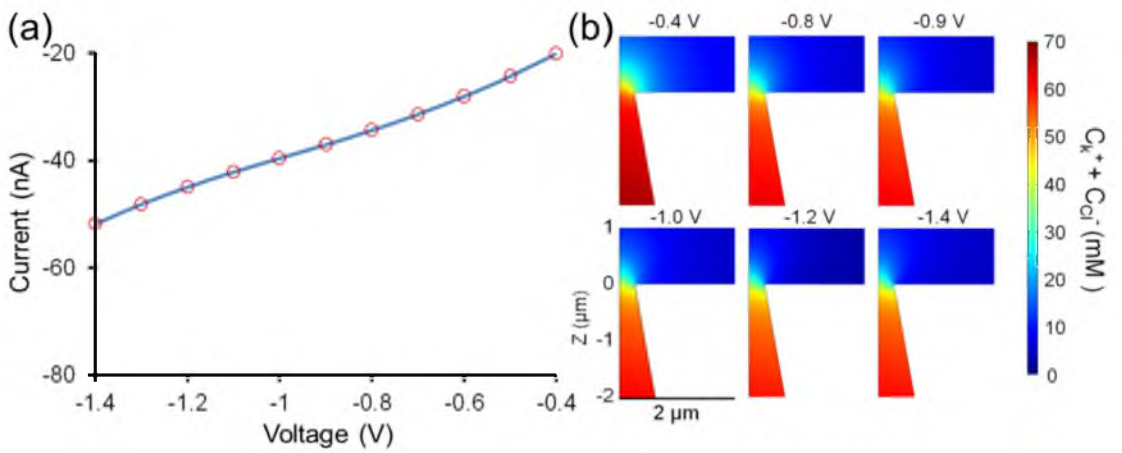

Figure 3.13. Simulation for 5 mM (external) and 50 mM (internal) KCl solutions. (a) Simulated *i-V* response for a 260 nm radius nanopore (external solution: 1 mM KCl and internal solution: 50 mM KCl; 10 mmHg). (b) Simulated total ion distribution near the nanopore orifice at voltages from -0.4 to -1.4 V.

3.5.3 Estimation of sensing zone surface area

A change in the surface charge density near the nanopore orifice, such as that due to Ca^{2+} binding, will dominate the NDR switching potential. This sensitivity to the orifice region is due to the conical shape of the nanopore which focuses the ion transport and fluid flow resistances at the orifice. We refer to this region as the "sensing zone." Changes in the surface charge density outside of this region have a weak influence on the electro-osmotic flow and thus a minimal impact on the NDR behavior. Here, we estimate the area of the sensing zone in order to estimate the absolute change in the amount of surface charge required to give a measurable shift in the NDR switching potential. This electrical charge, which can be detected by measuring the switching potential, corresponds to the number of analyte ions that bind to the surface within the sensing zone. The sensing zone surface includes two parts, as shown in Figure 3.14. The first surface is the exterior of the nanopore orifice (red line, corresponding to a ring of width a). The second surface is the interior of the nanopore (black line, represented by the length b). Simulations were conducted to estimate the dimension of the sensing zone surface by computing the electro-osmotic velocity (v) across the nanopore orifice (blue dashed line, Figure 3.14) as a function of both a and b. The electro-osmotic velocity profiles were calculated for a 370 nm radius pore with a half cone angle of 10 degrees, a surface charge density of -12.5 mC/m^2, a voltage of -0.5 V (internal *vs.* external) and in the absence of an applied external pressure. Internal/external KCl solutions of 50 mM/5 mM were used in the simulation, instead of 1 M/100 mM KCl used in the experiment, because the double layer region in the higher salt concentration solution requires a much finer mesh and a correspondingly heavier computational load. This difference in electrolyte

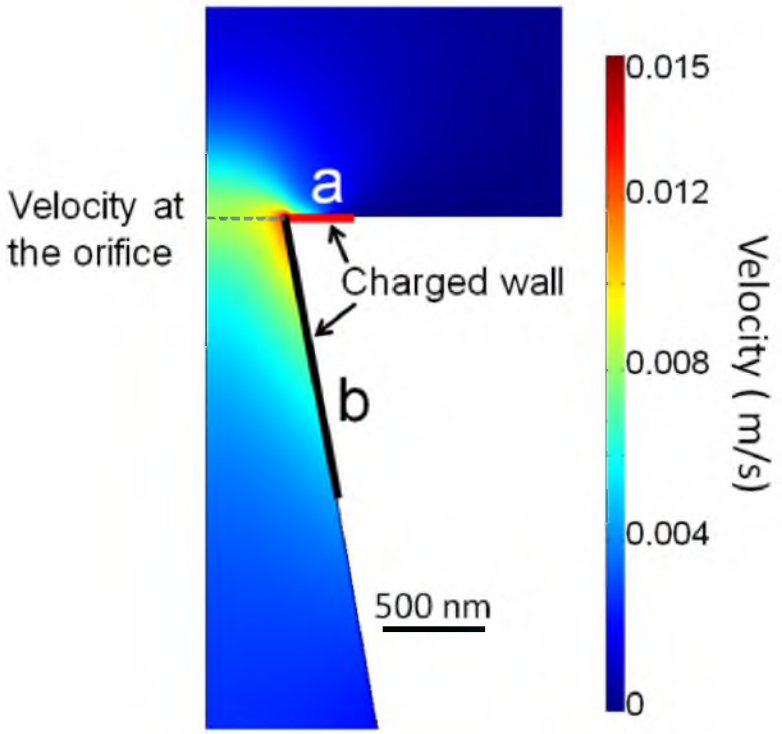

Figure 3.14. Schematic representation of the sensing zone surface for a 370-nm-radius glass nanopore. (The bold lines *a* and *b* are not drawn to scale.) The colored surface is the simulated electro-osmotic velocity profile for a = 185 nm and b = 5077 nm. The simulation shows that the influence of analyte binding on electro-osmotic velocity is largest within a small region near the nanopore orifice. The area of this region ("sensing zone") is approximately defined by the lengths *a* and *b*.

concentration yields a value of v different from that in the experiment, but still allows an estimation of the sensing zone area.

Figure 3.15a shows the dependence of v on the exterior surface ring width, a, for values between 25 and 890 nm. The maximum v (v_{max}) is also plotted in Figure 3.15b as a function of a. The length of a has a weak influence on the electro-osmotic flow rate when a is greater than 185 nm (equal to approximately half of the nanopore orifice radius), as seen in Figure 3.15b. In contrast, the length b influences the velocity more significantly as shown in Figure 3.16a and b. Although v_{max} decreases for $b > \sim 200$ nm, b was chosen as 370 nm (the radius of the nanopore) for simplicity.

Using $a = 185$ (half of the nanopore radius) and $b = 370$ nm (the nanopore radius), the overall sensing zone surface area can be calculated by summing the two parts and is equal to ~1.5 μm^2. Multiplication of this area by the surface charge density associated with analyte binding yields a rough estimate of the absolute number of analyte molecules that cause a shift in the NDR switching potential.

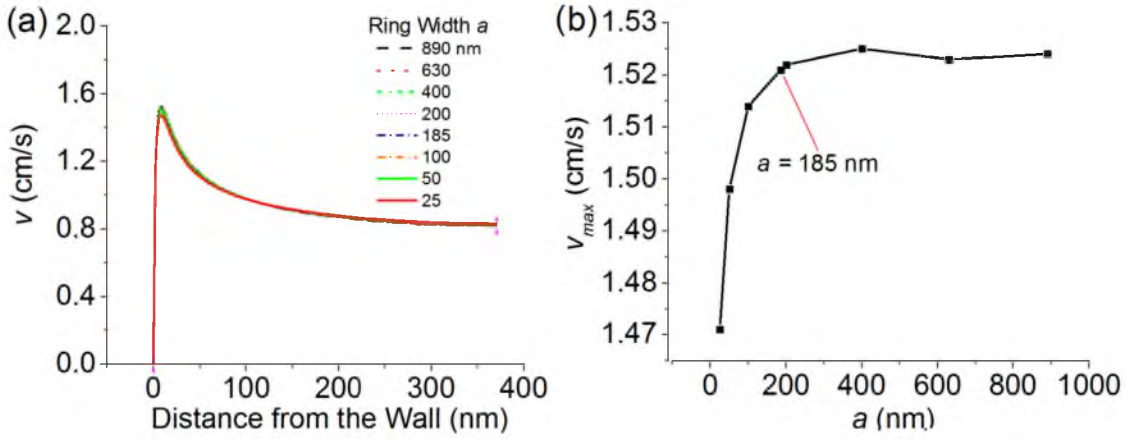

Figure 3.15. Simulation of the dependence of v at the nanopore orifice on a. (a) Simulated electro-osmotic flow rate v at the nanopore orifice at various ring width a. (b) the maximum v (v_{max}) in (a) as a function of a. See Figure 3.14 for definition of the parameter a. The calculations correspond to a 370-nm-radius glass nanopore.

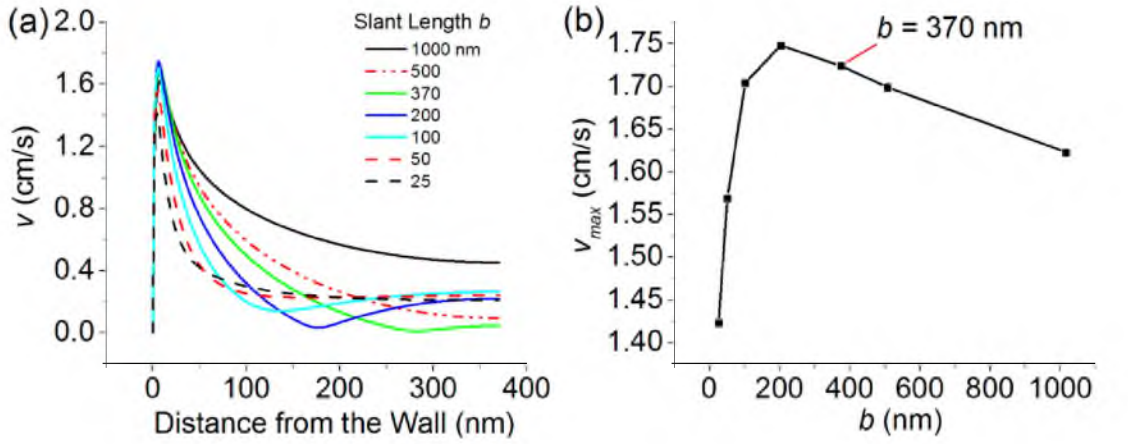

Figure 3.16. Simulation of the dependence of v at the nanopore orifice on b. (a) Simulated electro-osmotic flow rate v at the nanopore orifice at various length b. (b) The maximum v (v_{max}) in (a) as a function of b. See Figure 3.14 for definition of parameter b. The calculations correspond to a 370-nm-radius glass nanopore.

3.6 References

(1) Esaki, L. *Phys. Rev.* **1958**, 603-604.

(2) Wei, C.; Bard, A. J.; Feldberg, S. W. *Anal. Chem.*, **1997**, *69*, 4627–4633.

(3) Vlassiouk, I.; Kozel, T. R.; Siwy, Z. S. *J. Am. Chem. Soc.* **2009**,*131*, 8211-8220.

(4) He, Y.; Gillespie, D.; Boda, D.; Vlassiouk, I.; Eisenberg, R. S.; Siwy, Z. S. *J. Am. Chem. Soc.* **2009**, *131*, 5194-5202.

(5) Hou, X.; Guo, W.; Jiang, L. *Chem. Soc. Rev.*, **2011**, *40*, 2385-2401.

(6) Cheng, L.; Guo, L. J. *Chem. Soc. Rev.*, **2010**, *39*, 923-938.

(7) Perry, J. M.; Zhou, K.; Harms, Z. D.; Jacobson, S. C. *ACS Nano* **2010**, *4*, 3897-3902.

(8) Kovarik, M. L.; Zhou, K.; Jacobson, S. C. *J. Phys. Chem. B* **2009**, *113*, 15960-15966.

(9) Jin, P.; Mukaibo, H.; Horne, L. P.; Bishop, G. W.; Martin, C. R. *J. Am. Chem. Soc.* **2010**, *132*, 2118-2119.

(10) Siwy, Z. S. *Adv. Funct. Mater.* **2006**, *16*, 735-746.

(11) Siwy, Z.; Heins, E.; Harrell, C. C.; Kohli, P.; Martin, C. R. *J. Am. Chem. Soc.* **2004**, *126,* 10850-10851.

(12) Vlassiouk, I.; Siwy, Z. S. *Nano Lett.* **2007**, 7, 552-556.

(13) Yameen, B.; Ali, M.; Neumann, R.; Ensinger, W.; Knoll, W.; Azzaroni, O. *J. Am. Chem. Soc.* **2009**, *131*, 2070-2071.

(14) Ali, M.; Yameen, B.; Cervera, J.; Ramirez, P.; Neumann, R.; Ensinger, W.; Knoll, W.; Azzaroni, O. *J. Am. Chem. Soc.* **2010**, *132*, 8338-8348.

(15) Guerrette, J. P.; Zhang, B. *J. Am. Chem. Soc.* **2010**, *132*, 17088-17091.

(16) Sa, N. Y.; Baker, L. A. *J. Am. Chem. Soc.* **2011**,*133*, 10398-10401.

(17) Sa, N. Y.; Fu, Y. Q.; Baker, L. A. *Anal. Chem.* **2010**, *82*, 9963-9966.

(18) Sa, N. Y.; Lan, W. J.; Shi, W. Q.; Baker, L. A. *ACS Nano*, **2013**, *7*, 11272-11282.

(19) Zhao, S.; Zheng, Y. B.; Cai, S. L.; Weng, Y. H.; Cao, S. H.; Yang, L. J.; Li, Y. Q. *Electrochem. Commun.* **2013**, *36*, 71-74.

(20) Zhang, L. X.; Cai, S. L.; Zheng, Y. B.; Cao, X. H.; Li, Y. Q. *Adv. Funct. Mater.* **2011**, *21*, 2103–2107.

(21) Cao, L. X.; Guo, W.; Wang, Y. G.; Jiang, L. *Langmuir* **2012**, *28*, 2194-2199.

(22) Ai, Y.; Zhang, M.; Joo, S. W.; Cheney, M. A.; Qian, S. *J. Phys. Chem. C* **2010**, *114*, 3883-3890.

(23) Lan, W. J.; Holden, D. A.; White, H. S. *J. Am. Chem. Soc.* **2011**, *133*, 13300-13303.

(24) White, H. S.; Bund, A. *Langmuir* **2008**, *24*, 2212-2218.

(25) Yusko, E. C.; An, R.; Mayer, M. *ACS Nano* **2010**, *4*, 477-487.

(26) Firnkes, M.; Pedone, D.; Knezevic, J.; Doblinger, M.; Rant, U. *Nano Lett.* **2010**, *10*, 2162- 2167.

(27) Paik, K.; Liu, Y; Tabard-Cossa, V.; Waugh, M. J.; Huber, D. E.; Provine, J.; Howe, R. T.; Dutton, R. W.; Davis, R. W. *ACS Nano* **2012**, *6*, 6767-6775.

(28) Davenport, M.; Healy, K.; Pevarnik, M.; Teslich, N.; Cabrini, S.; Morrison, A. P.; Siwy, Z. S.; Le´tant, S.E. *ACS Nano* **2012**, *6*, 8366-8380.

(29) He, Y. H.; Tsutsui, M.; Fan, C.; Taniguchi, M.; Kawai, T. *ACS Nano* **2011**, *5*, 5509-5518.

(30) He, Y. H.; Tsutsui, M.; Fan, C.; Taniguchi, M.; Kawai, T. *ACS Nano* **2011**, *5*, 8391- 8397.

(31) Ai, Y.; Liu, J.; Zhang, B. K.; Qian, S. *Anal. Chem.* **2010**, 82, 8217-8225.

(32) Lan, W. J.; Holden, D. A.; Liu, J.; White, H. S. *J. Phys. Chem. C* **2011**, *115*, 18445-18452.

(33) Lan, W. J.; Holden, D. A.; Zhang, B.; White, H. S. *Anal. Chem.* **2011**, *83*, 3840-3847.

(34) Lan, W. J.; White, H. S. *ACS Nano* **2012**, *6*, 1757-1765.

(35) Luo, L.; Holden, D. A.; Lan, W.J.; White, H.S. *ACS Nano*, **2012**, *6*, 6507-6514.

(36) Siwy, Z. S.; Powell, M. R.; Kalman, E.; Astumian, R. D.; Eisenberg, R. S. *Nano Lett.* **2006**, *6*, 473-477.

(37) Siwy, Z. S.; Powell, M. R.; Petrov, A.; Kalman, E.; Trautmann, C.; Eisenberg, R. S. *Nano Lett.*, **2006**, *6*, 1729–1734.

(38) Zhang, B.; Galusha, J.; Shiozawa, P. G.; Wang, G.; Bergren, A. J.;Jones, R. M.; White, R. J.; Ervin, E. N.; Cauley, C. C.; White, H. S. *Anal. Chem.* **2007**, *79*, 4778-4787.

(39) Grahame, D. C. *J. Chem. Phys.***1953**, *21,*1054-1060.

(40) Probstein, R. F. Physicochemical hydrodynamics: An introduction, Second Edition; John Wiley & Sons, Inc.: New York **1994.**

(41) Datta, S.; Conlisk, A.T.; Li, H. F.; Yoda, M. *Mech. Research Comm.* **2009**, *36,* 65-74.

(42) Remillar, P.A.; Mass, L.; Amorelli, M. C.; Danville, N.H. Lock-in Amplifier. *U.S. Patent* 5,210,484, May 11, **1993**.

(43) Scofield, J. H. *Am. J. Phys.* **1994**, *62,* 129-133.

(44) Dixon, P. K.; Wu, L. *Rev. Sci. Instrum.* **1989**, *60*, 3329-3336.

(45) Probst, P. A.; Collet, B. *Rev. Sci. Instrum.* **1985**, *56*, 466-470.

(46) Temple, P.A. *Am. J. Phys.* **1975,** *43*, 801-807.

(47) Behrens, S. H.; Grier, D. G. *J. Chem. Phys.* **2001**, *115*, 6716-6721.

CHAPTER 4

CONTROLLING NANOPARTICLE DYNAMICS IN CONICAL NANOPORES

4.1 Introduction

Characterization of the geometry, charge, and dynamic properties of individual nanoscale objects in bulk solution presents a significant challenge, particularly for objects at the lower end of the scale. Transmission electron microscopy (TEM) does not assess particles in bulk solution, and dynamic light scattering (DLS) does not provide information about individual particles. Furthermore, these techniques are prone to artifacts.[1] By contrast, resistive pulse analyses using nanopores provide a method that measures individual nanoscale particles in bulk solution as well as providing information about particle charge. Recent adaptations of the Coulter-counter technique to the nanoscale range have been used as a label-free method for studying biological molecules, especially DNA, and nanoparticles having a variety of compositions and surface charges.[2] In these techniques, an electrical potential difference is applied between the electrodes on the two sides of a nanopore. Nanoparticles passing through the pore cause a brief decrease in the electrical current plotted as a function of time. The duration, magnitude, and shape of these current-time profiles provide a wealth of information about the forces that act on the nanoparticles as they pass through the pore.[2, 3] However,

large particle velocities can limit the application of this technique to a significant portion of the nanoscale range.

Reliable detection and characterization of small nanoparticles is limited by electronic filtering, which for typical bandwidths of 10 kHz leads to an underestimation of peak heights for detectable particles and can even entirely miss particles below 40 nm for certain pore geometries.[3] Innovative attempts to overcome the problem of excessive translocation speed include chemical modification of pores[4] and variations in pore size,[5] shape,[6] salt concentration, temperature, and solution viscosity,[7] as well as employing repeated measurements of individual particles.[8, 9] By varying pH to adjust the difference in zeta potential between the particle and the pore, Firnkes *et al.* were able to manipulate the effective velocity of a single protein and to reverse the translocation driving force from electrophoretic to electro-osmotic.[10] While this method provides an important step forward in controlling particle speed, significant diffusion rates across the 10-nm wide pore reduce signal fidelity.

Cylindrical carbon nanotubes[11] and glass nanochannels[12] have been used to characterize 60-nm and 40-nm particles, respectively, but measurement of smaller particles was hindered by low signal-to-noise ratios. By contrast, focusing of the sensing zone in conical nanopores to a much smaller volume imparts many advantages including high signal-to-noise ratios and asymmetric peak shapes, which provide information about translocation direction.[3] Recently, Vogel *et al.* reported a method for characterizing the surface charge of 200-nm particles based upon resistive pulse sensing in conical nanopores under variable pressure.[13] The elastomeric pores used in these studies have the advantage that they can be dynamically varied in size; however, the hydrophobic nature

of this pore material may lead to undesirable interactions with hydrophobic analytes and solvents other than water. By contrast, the hydrophilic surfaces of silicon nitride (SiN) and glass nanopores (GNPs) are often desirable for studies involving both hydrophobic and hydrophilic analytes. SiN pores are frequently used to study nucleic acids and other large aspect ratio particles,[14] but there are far fewer studies of low aspect ratio (spherical) particles below 40nm,[15] likely due to excessive particle speeds through a short sensing zone. SiN pores have the advantage that pore size is readily measured during their production, but the process is not simple and quite expensive.

By contrast, simple and inexpensive methods exist for producing GNPs that can detect low aspect ratio molecules as small as 1.5 nm.[16, 17] In addition to hydrophilicity, GNPs have numerous advantages compared to other types of pores in terms of exceptional electrical properties for high bandwidth measurements, ability to withstand high pressure, compatibility with optical measurements, chemical stability, and the possibility to modify their surface with a variety of functional groups. Gao *et al.* reduced particle velocities sufficiently to detect 10-nm gold nanoparticles by producing GNPs near the threshold at which the particle could pass through.[16] Though inadequate for general control of particle dynamics, this approach did provide a method for determining pore size, which was not possible using electron microscopy.[16, 17] In this chapter, we further characterize the threshold condition, and demonstrate control of velocities over three orders of magnitude for 8-nm nanoparticles in GNPs. Finite element analysis (FEA) simulations are used to verify these experimental results providing further insights into pore geometry, spatial distribution of particle velocities within the pore, and the influence of both the particle and pore surface charge densities. We provide a rationale for how

particle dynamics are controlled by balancing the pressure, electrophoretic (EPF), and electro-osmotic (EOF) forces (Figure 4.1). This balance of three forces provides previously unattainable control over particle dynamics in a conical pore.

This work was completed through collaboration with Revalesio Corporation and our laboratory at the University of Utah; the experimental part was conducted at a Revalesio facility while the theoretical investigation was accomplished at the University of Utah.

4.2 Experimental section

4.2.1 Chemicals and materials

Spherical gold nanoparticles (diameter: 8 nm ± 7%, SD, measured by TEM) conjugated with carboxy methyl polymer were purchased from Nanopartz, Inc. (Loveland, CO). Zeta (ζ) potentials were measured as -51 mV and -15 mV (Nanopartz) and as -52 mV and -22 mV (Particle Characterization Laboratories, Inc., Novato, CA) in deionized water, and as -38 mV and -12 mV in 0.1 NaCl PBS pH 7.4 plus 0.1% Triton X-100 (Particle Characterization Laboratories, Inc.). Attempts to measure zeta potentials at higher salt concentrations yielded irreproducible values. The particles are denoted as -51 mV and -15 mV in the text even though ζ values are lower in salt solutions. Other materials included borosilicate glass micropipettes (OD: 1.5 mm, ID: 0.86 mm, length: 10 cm, Sutter Instruments), hydrofluoric acid (48%), ammonium fluoride solution (~40%), ammonium fluoride etching mixture (AF 875-125, Sigma), pH 7.4 phosphate buffered saline (PBS) 10X (Invitrogen), 3M 12 micron Lapping Film (Ted Pella), Triton-X100 (Amresco), 0.25 mm Ag wire (World Precision Instruments), household bleach (5%

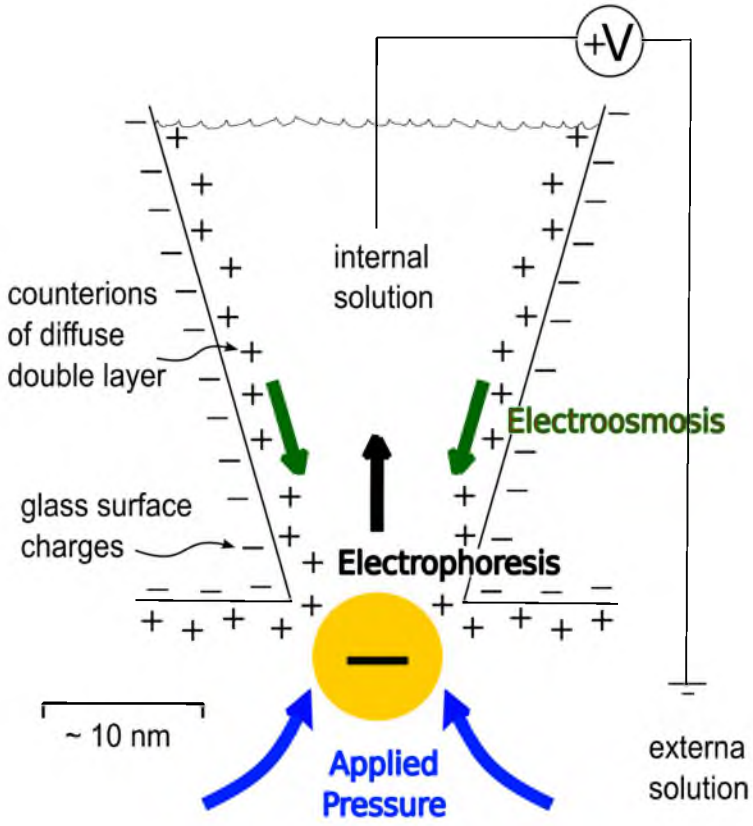

Figure 4.1.Driving forces acting on a particle in a conical nanopore. During translocation experiments, positive potentials applied to an electrode within the pipette and negative pressures applied within the pipette both tend to draw negatively charged particles inward from the external solution. The applied potential also induces a counteracting electro-osmotic force that tends to drive particles out of the pipette into the external solution. The summation of these different forces determines the particle velocity and translocation timescale.

hyprochorite) and sodium bicarbonate (Costco). Solutions were filtered through Millex-GP, 0.22 μm, polyethersulfone filters (Millipore).

4.2.2 Pipettes

Pipettes were pulled with a Model P-1000 Flaming/Brown micropipette puller (Sutter Instruments) to an ~1 μm opening. Pulled pipette tips were then melted with a butane hand torch (flame tip positioned ~5 mm from the tip) for ~130 ms as the pipettes rotated on a turntable at 3.5 cm/s. Sanding of the resulting terminal bulb was carried out by hand prior to microforge heating, which involved placing the pipette tip within a Ω-shaped platinum-iridium alloy filament (5 mm by 5 mm) heating element made from a 5-mm wide platinum/iridium strip for ~400 ms. Pipette tips were initially imaged using an inverted Olympus IX50 microscope, and then a few were selected for SEM imaging with a FEI Helios Nanolab 600 Dual-Beam FIB.

4.2.3 Glass nanopore fabrication

Borosilicate glass micropipettes were heated at 600°C for 12 h and then immediately sealed at both ends. After being pulled to an ~1 μm opening, they were kept under a stream of dry nitrogen until the sharp tip was melted. The terminal bulb inclosing a conical cavity was then sanded to a flattened tip using fine sandpaper followed by microforge heating. Just prior to etching, the other end of the pipette was opened, fire polished, and back-filled with 1.0 M NaCl. Ag/AgCl electrodes where prepared by immersing an Ag wire in bleach for ~15 min prior to experiments, and were placed inside multiple pipettes connected in parallel as well as the etchant solution (a 1:2 dilution of 48%

hydrofluoric acid in a ~40% ammonium fluoride solution). Pore formation was indicated by a jump in current measured using a Princeton Applied Research 2273 PARSTAT potentiostat operating in current *vs.* time mode with 250 mV applied potential. Pipette tips were immediately dipped into 3 M KOH for 10 s and transferred to a 1.0 M NaCl solution for current measurements. Pores having resistances between 100 and 200 MΩ were routinely made in this way, etched to larger sizes as needed by dipping briefly (15 s) into a 1:20 dilution of Ammonium fluoride etching mixture (AF 875-125), and repeating the etching process until threshold translocations no longer occurred.

4.2.4 Resistive pulse sensing measurements and data analysis

Pipettes were placed into a BNC style electrode holder that allowed for application of pressure within the pipette (Warner Instruments), and current measurements made using a HEKA EPC-10 amplifier at a cutoff frequency of 3 kHz applied with a three-pole Bessel low-pass filter. PatchMaster data acquisition software was used to initially analyze and export current-time traces. A custom VBA Excel program was used to determine translocation peak parameters such as peak position, height, and width at half-height as a function of applied voltage. Each peak was inspected manually to ensure accurate measurements; in general, resistive pulses having a signal-to-noise ratio of less than 7:1 and/or a base width of less than 1 ms were excluded.

4.2.5 Finite element simulations

The finite-element simulations were performed to analyze the particle veliocity in the nanopores using COMSOL Multiphysics 3.5 (Comsol, Inc.).

4.3 Results and discussion

4.3.1 Detecting nanoparticles at the threshold of the pore size

Micropipette GNPs were prepared by a modification of the method described by Gao *et al.*[16] (Figure 4.2). Determining the size of a micropipette GNP is not simple, and others have reported being unable to obtain SEM images of the pore.[16, 17] Here, we report SEM images of a micropipette GNP used to measure 8-nm diameter gold nanoparticles (Figure 4.3). Although the diameter of the pore was found to be 37 nm at the surface, the pore may narrow just below the surface due to the etching procedure. Based on the microscopy images (Figure 4.2a and b) and the characteristic asymmetric translocation profiles and FEA simulations, *vide infra*, we believe that the inner pore geometry is conical with a ~2° cone angle.[18] A subsequent report concerning the inner pore geometry is in preparation.

Identifying the size of a particle at the threshold of passing through the pore provides an alternative to SEM imaging for sizing micropipette-based GNPs. We performed experiments to detect nanoparticle translocations using 8-nm diameter carboxy methyl polymer-coated Au nanoparticles having small standard deviation in size (± 0.6 nm), and at a typical concentration of 200 nM in a 1.0 M NaCl solution. Current *vs.* time (*i-t*) traces were recorded while a positive potential was applied to an Ag/AgCl wire electrode within the micropipette relative to the external solution. We first produced the smallest pores possible (having a resistance between 100 and 200 MΩ, measured in 1.0 M NaCl), and repeatedly widened them with dilute etchant until we detected pressure driven nanoparticle translocations. This approach enabled us to detect cases in which square blocks were terminated with a sharp resistive pulse as illustrated by the 17 pA

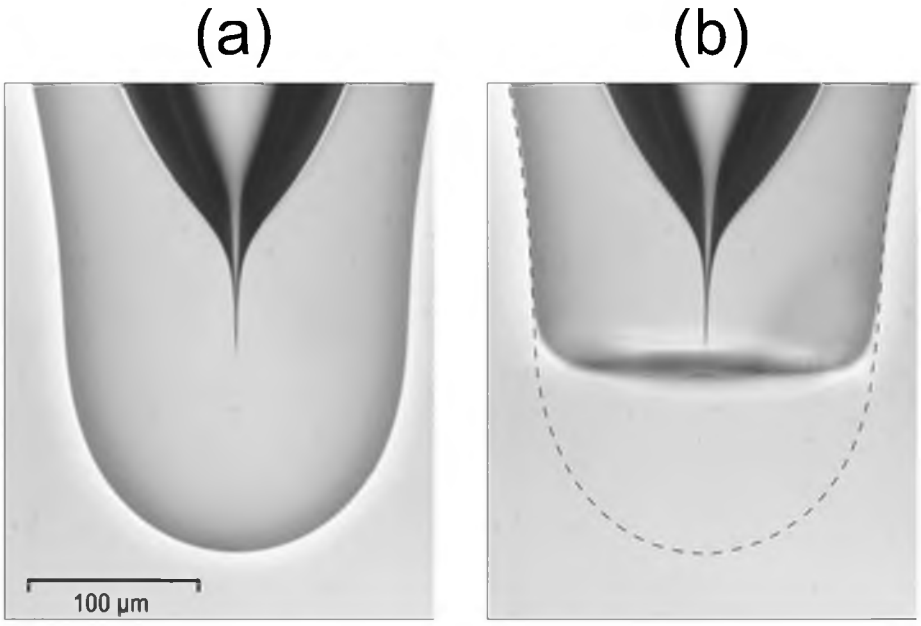

Figure 4.2. Optical images of a micropipette before and after chemical etching. (a) A programmable micropipette puller was used to form a narrow opening (1 µm) that was melted into a terminal bulb enclosing a cone-shaped cavity. (b) The terminal bulb was then sanded and briefly melted with a microforge to form a flattened geometry (dashed lines delineate the outlines of the original bulb shown in (a)). Ag/AgCl electrodes were placed across the unopened pore and hydrofluoric acid etchant was used as the external solution to form a nano-scale pore in the sanded and remelted tip. A spike in the current indicated pore formation.

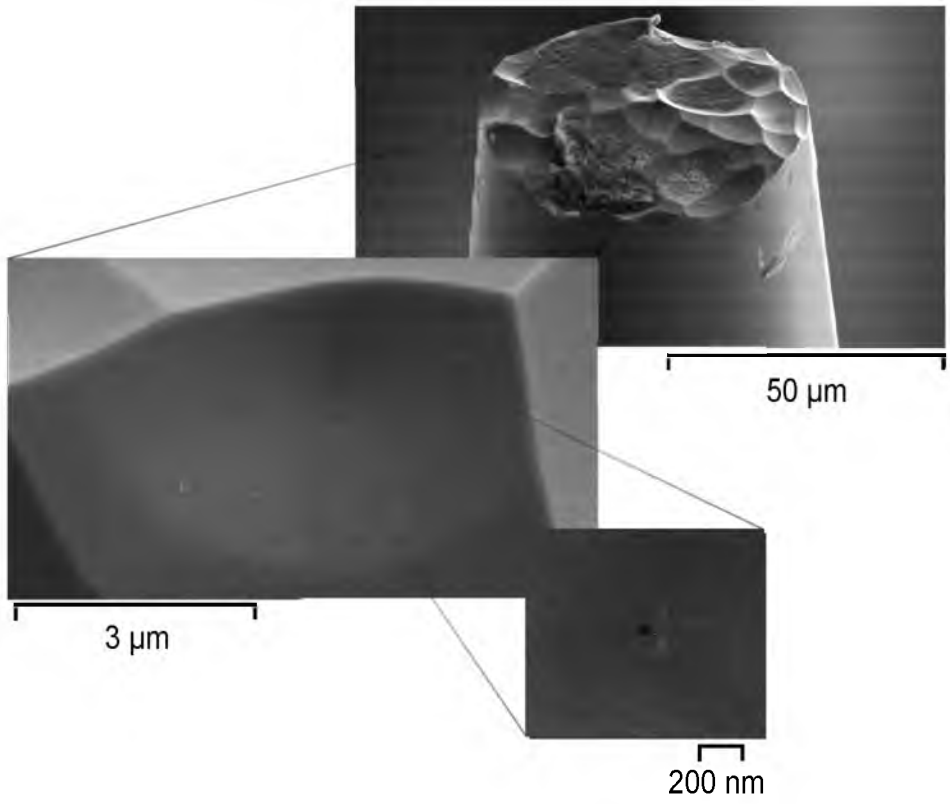

Figure 4.3. Scanning electron microscope (SEM) images of a nanopore in a micropipette tip that had been used to detect 8-nm nanoparticles. Prior to imaging, this nanopore was rinsed with deionized water, allowed to dry, and then sputtered with a ~2 nm thick layer of gold. The opening located at the center of the pipet tip has a diameter of 37 nm at the surface.

current block in Figure 4.4b, which ends with a 70 pA peak before returning to the base current. Since this terminal spike is large and has the asymmetric triangular shape typical of a particle translocation through a conical pore, we believe it represents a particle passing through the pore after an initial partial blockade of the opening. Vercoutere *et al.* observed similar long shallow blockades caused by individual hairpin DNA molecules prior to a rapid deep blockade, indicating translocation of the DNA through an α-hemolysin pore.[19] Though the geometrical considerations for gold nanoparticles are much simpler, it is possible that the particle coating requires time to compress in order for the particle to fit through the pore at the threshold size. Gao *et al.*, also used the threshold condition to estimate the size of their pores using DNA, 10-nm Au nanoparticles, and even single molecules of β-cyclodextrin, based on simple square-shaped blocks lacking a terminal spike.[16] Based upon repeated observations of this kind, we conclude that the occurrence of square blockages without a sharp spike at the end (Figure 4.4a) represents transient blockages of the nanopore orifice by the Au nanoparticles without translocation through the pore.

4.3.2 Particle capture and release

Applying pressure within the pipette offers considerable control over particle translocation, including the ability to draw individual particles into the pore and to push them out again repeatedly, as illustrated in 4.5 Appendix. Because the quasitriangular peak shape depends on the direction of translocation, these experiments provide confirmation that our pores are conically shaped and open inwardly. Similar observations of particle reversal with application of pressure have been used to measure the size of

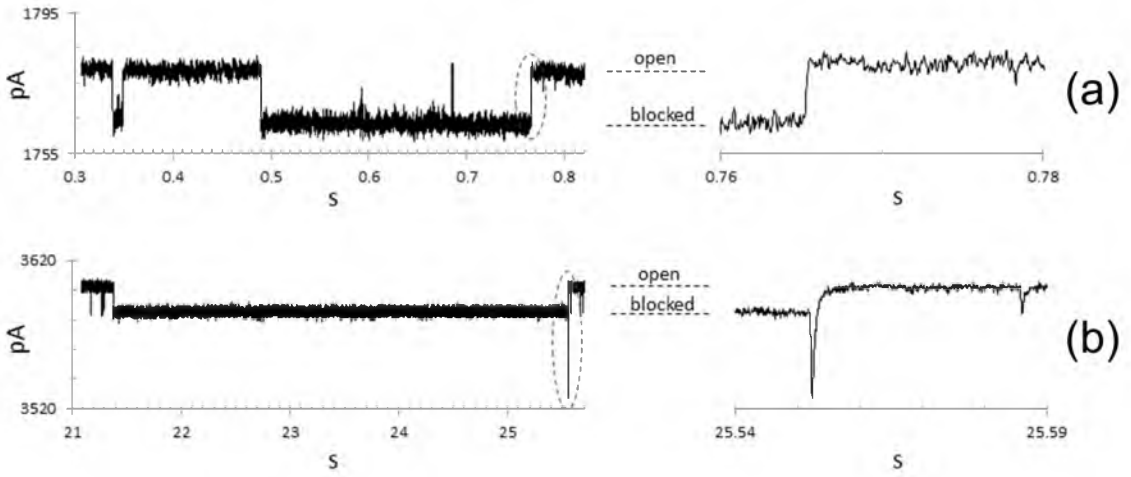

Figure 4.4. *i-t* traces used to determine when the pore size exceeds or is just at the threshold of the Au nanoparticle size. In these experiments, 8-nm Au nanoparticles (ζ = -51 mV) were placed in the external solution, and a pressure of ~0.5 atm and voltage of 250 mV were applied to drive the particles into the nanopore. (a) Square-shaped blockades of widely varying duration are observed when the pore size is smaller than the particle size. The current within these blocks sometimes increases briefly, as seen at 0.59 s and 0.68 s, but eventually returns to the base current level as seen in the dashed oval in (a) (the trace on the right is an expansion of this region). (b) Passage of a particle through another pore at the threshold of the particle size accompanied by a large current spike (dashed oval in (b)). Note that this current spike (expanded on the right) has the asymmetric shape characteristic of a typical translocation through a conical pore. The 1.0 M NaCl solution was buffered at pH 7.4 with 7 mM Na_2HPO_4, 21 mM KH_2PO_4, and contained 0.1% Triton X-100.

individual particles depending upon their recapture probability.[20] The distinct differences seen in translocation shape for individual particles in 4.5 Appendix reflect the acute sensitivity of this technique to monitor subtle nanopore/nanoparticle characteristics that are most likely based on geometrical and charge interactions.

Figure 4.5 demonstrates that varying the applied potential can also be used to drive particles into and out of a pore repeatedly. In the experimental results shown in Figure 4.5a, b, no pressure was applied to the pipette, but instead the particle motion followed a 10 Hz square wave varying between +1.0 V and -1.0 V. The four occasions of a particle going into and out of the pore were preceded and followed by several seconds without any particle translocations, suggesting that we observed the repeated translocations of a single particle. Similar voltage switching experiments have been used to recapture individual DNA strands.[9] Reversing voltage polarity is not required for particle capture and release if pressure is applied additionally. This is illustrated in Figure 4.5c, d, where a square wave oscillating between +225 mV and +525 mV is sufficient to drive particles into and out of a pore as a constant negative pressure of ~0.05 atm is applied.

4.3.3 Controlling nanoparticle dynamics by applied pressure and applied potential

Either electrophoresis or applied pressure alone has typically been used as the single driving force for moving particles through a nanopore, as demonstrated in the previous section. Decreasing the particle translocation velocity by lowering voltage has limitations, however, because the signal-to-noise ratio is reduced dramatically as the

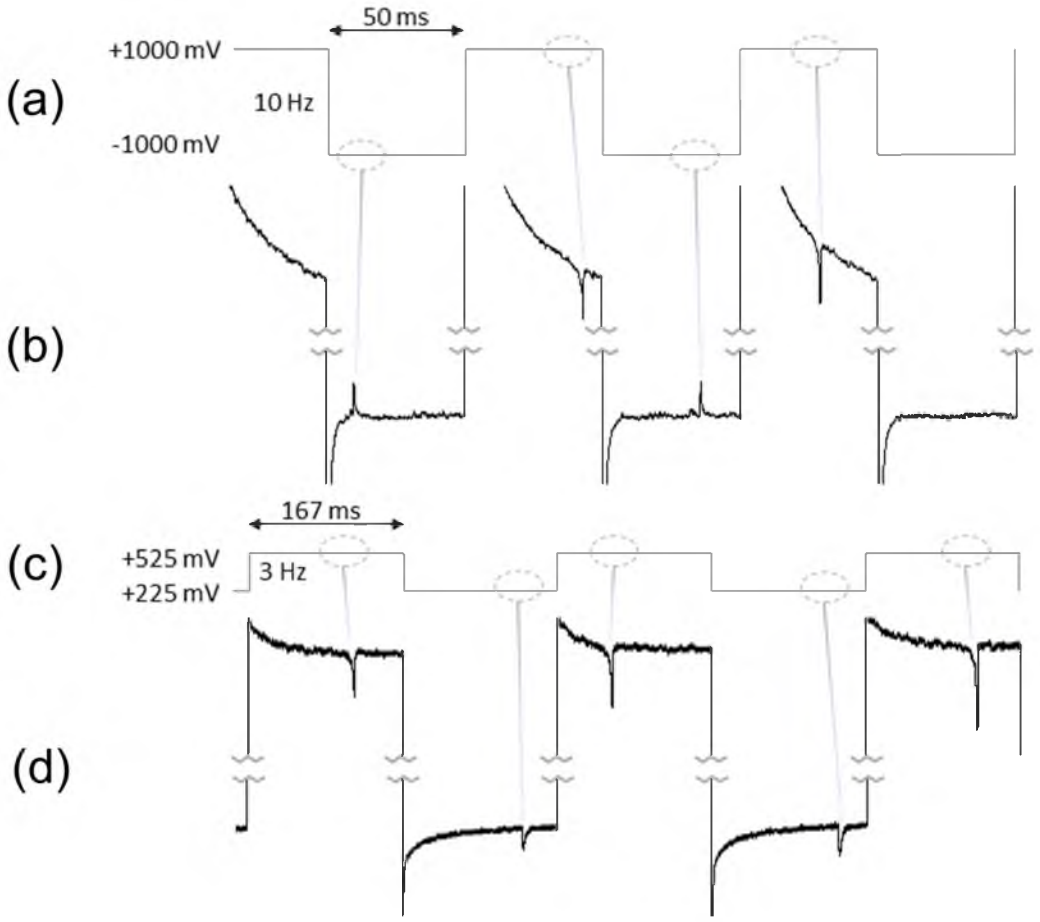

Figure 4.5. *i-t* traces showing a single nanoparticle passing back and forth through the nanopore orifice as the applied potential is reversed. (a) A 10-Hz voltage square wave between +1000 and -1000 mV results in resistive pulses in the *i-t* trace shown in (b). The *i-t* traces in (b) are clipped to show just the relevant 50-ms portions of the square wave where translocations occur. (c) A 3-Hz square wave between only +525 and +225 mV also results in a single nanoparticle passing back and forth through the pore orifice. Both solutions contained 8-nm Au nanoparticles (ζ = -51 mV) in 1.0 M NaCl PBS pH 7.4 plus 0.1% Triton X-100. Particle concentration in (b) equals 50 nM, and in (d) equals 320 nM.

voltage decreases. Here, we report fine control of particle velocities by taking advantage of electro-osmosis and by applying a constant pressure to shift the zero velocity point to a potential with acceptable signal-to-noise ratio (Figure 4.6). In this experiment, translocation velocities were assumed to be proportional to the inverse of the peak width at half height, with positive values indicating translocations into the pipette. Negative pressures indicate fluid flow into the pipette; positive voltages are measured relative to the external solution (see Figure 4.1). At the outset of the experiment, the majority of 8-nm gold particles were outside of the pipette, except for a small number of particles that had been pulled into the pipette under pressure just prior. The pipette was then subjected to a constant negative pressure (-0.047 atm in Figure 4.6a and -0.35 atm in Figure 4.6b) and +500 mV. Both of these forces should act to drive negatively charged particles into the pipette, and yet the particle translocation profiles clearly indicated that nanoparticles were expelled from the pipette. This is explained by the presence of a large electro-osmotic flow that overpowers both the applied pressure and the electrophoretic forces acting on the particles under these conditions (Figure 4.1).[10] For the experiments in Figure 4.6, the contributions to the effective velocity made by applied pressure, electrophoresis, and electro-osmosis are schematically illustrated in Figure 4.7. As the potential was ramped down to +100 mV over the course of five minutes, the EOF decreased at a faster rate than the EPF, and the driving forces acting on the particle were balanced at a characteristic transition voltage that was determined by the zeta potential of the particles. Particle velocities were markedly reduced at this transition. Of the 1,890 translocations shown in Figure 4.6, thirteen had peak widths greater than 20 ms and two were as large as ~200 ms. For the slowest translocations, the negation of all particle

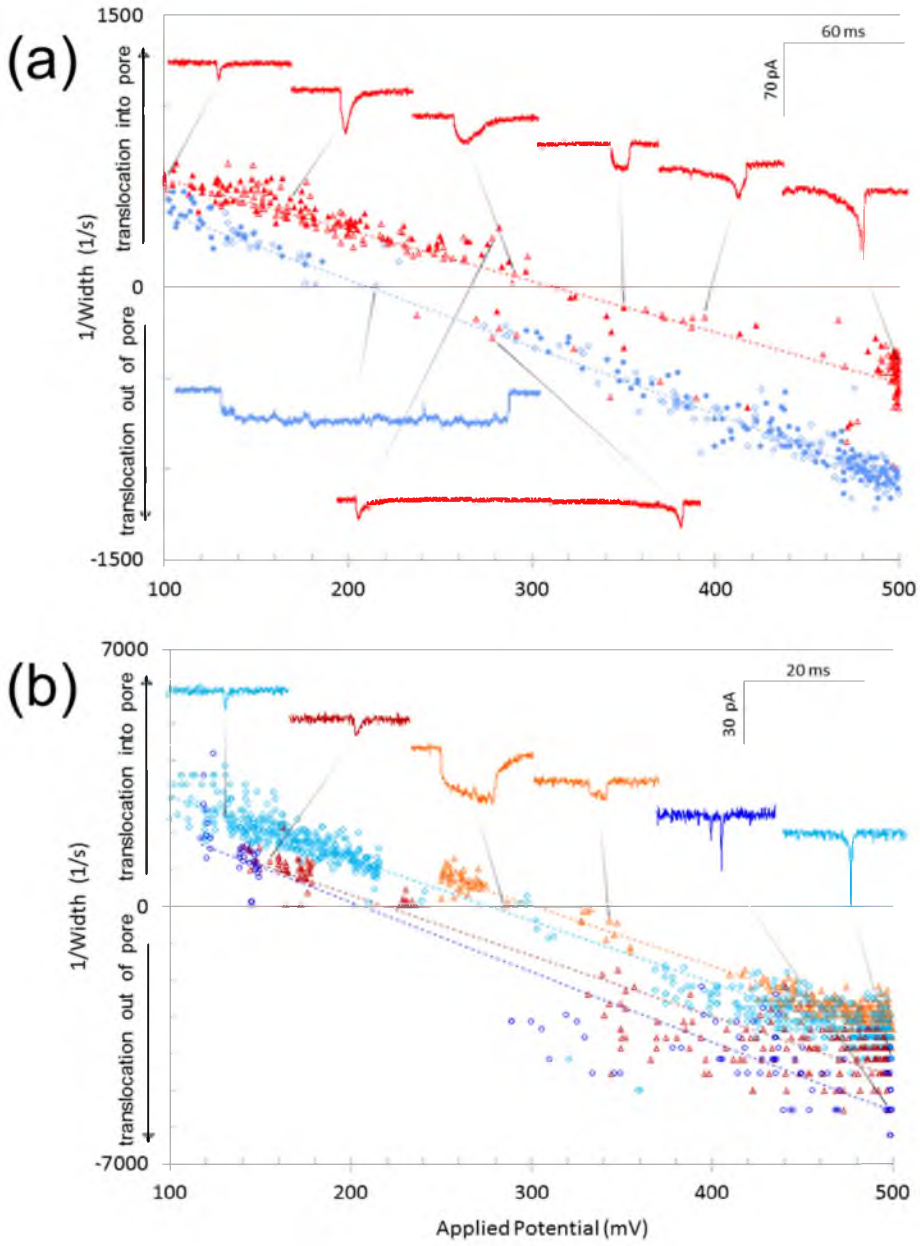

Figure 4.6. Nanoparticle translocation velocity *vs.* applied voltage at a pressure of (a) -0.047 atm and (b) -0.35 atm. The solution conditions are for (a): 1.0 M NaCl, △,▲ (ζ = -51 mV) and ○,● (ζ = -15 mV), and for (b): 0.2 M NaCl: △ (ζ = -51 mV) and ○ (ζ = -15 mV); 0.1 M NaCl: △ (ζ=-51 mV) and ○ (ζ=-15 mV). All solutions were buffered at pH 7.4 with 7 mM Na_2HPO_4, 21 mM KH_2PO_4, and contained 0.1% TritonX-100. The filled and open symbols in (a) represent two consecutive sets of data collected under identical conditions. Dashed lines through data points represent linear least squares fits. Representative *i-t* traces for particular translocations at different voltages are shown.

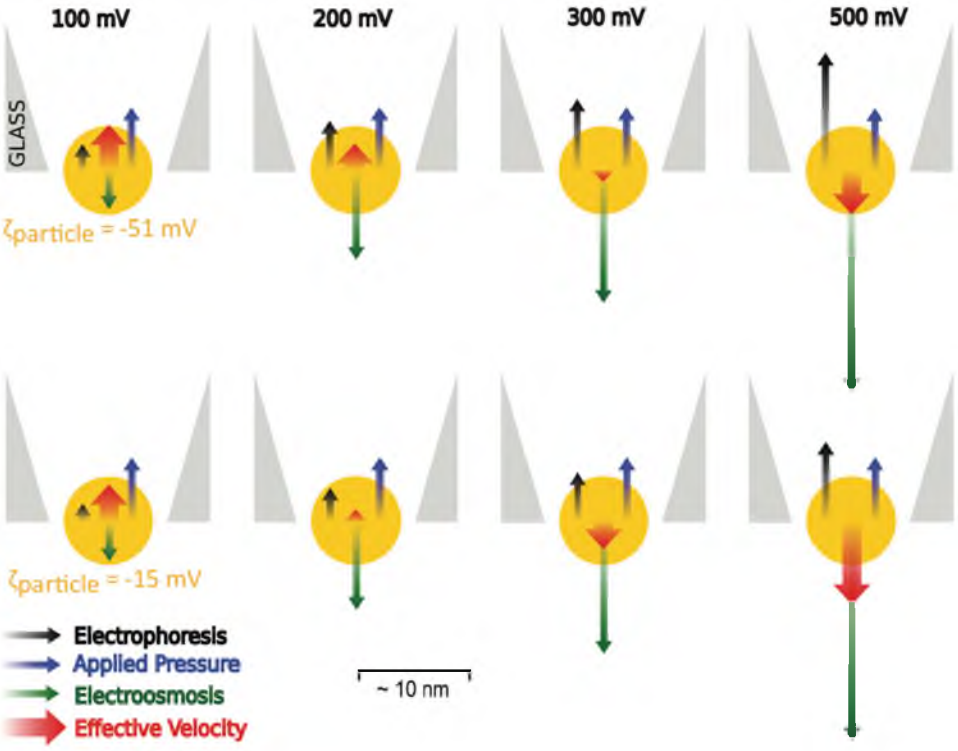

Figure 4.7. Schematic depicting control of nanoparticle velocity in conical nanopores. The voltage-dependent peak widths presented in Figure 4.6 result from the summed contributions of different forces acting on the charged nanoparticle. The applied pressure (-0.047 atm) remains constant throughout all measurements, but the *particle-dependent* electrophoretic and *particle-independent* electro-osmotic forces change at different rates with varying voltage. As a result, the more highly charged particles (ζ = -51 mV) obtain a minimum velocity at ~300 mV, while the less charged particles (ζ = -15 mV) obtain a minimum velocity at ~200 mV.

driving forces allowed us to see the effects of Brownian motion as the particle flickered in and around the sensing zone (blue trace inset in Figure 4.6a). This is in sharp contrast to the *i-t* traces recorded near the voltage limits where peak widths were $\leq$ 0.2 ms, representing an increase in particle velocity of three orders of magnitude. The limited number of translocations near 200 – 300 mV is a consequence of the diminishing particle rate of entry near the transition voltage, and of the small number of particles that initially is inside the pipette; the particles were eventually exhausted as the potential was decreased from 500 mV to the transition voltage. Below this voltage, particles were drawn into the pipette from the external solution, as the combined EPF and applied pressure force became larger than the EOF.

Although there was considerable data scatter, the general trend was reproducible across two independent experiments carried out under identical conditions (Figure 4.6a, opened and closed symbols). The experiments in Figure 4.6a were carried out with the same pipette (having a resistance of 110 MΩ at 1.0 M NaCl), and those in Figure 4.6b were all carried out with a different pipette (having a resistance of 125 MΩ at 1.0 M NaCl). Some of the data scatter at highest and lowest applied potential is based on limitations in our ability to accurately measure peak width for the fastest moving particles (thus the digitization seen on the right of Figure 4.6b). Slow moving particles also involve scatter, presumably because additional surface forces acting on the particles become significant under these conditions. The data scatter is particularly severe when the salt concentration is < 0.2 M NaCl, mostly due to the relatively poor signal-to-noise. The experiments under low salt conditions (0.1 - 0.2 M NaCl) were done with a pore within 10 MΩ (measured at 1.0 M NaCl) of the threshold size in order to maximize the

amplitude of the resistive pulses, particularly near 100 mV. The observation of several near zero velocity events that do not fall in line with the data trend likely indicates particles that have interacted strongly with the pore wall, because fluid flow was not fast enough to deter physisorption.

One additional source of apparent data scatter is cross contamination between experiments. For example, the ζ = -15 mV data shown in Figure 4.6a were collected prior to the ζ = -51 mV data shown in the same figure, and despite efforts to thoroughly rinse the pipette between experiments, the red triangles falling in line with the ζ = -15 mV data likely indicate the presence of residual ζ = -15 mV particles. This assumption is supported by the fact that the signals show the opposite peak symmetry at the transition voltage of the ζ = -51 mV particles. This is demonstrated by the lowest red inset in Figure 4.6a, which suggests that two particles, one with ζ = -15 mV and one with ζ = -51 mV, are crossing the pore in different directions at the same applied potential.

4.3.4 Factors governing particle velocity

In resistive pulse sensing, particle velocities are governed by the relative strengths of the EPF, EOF, and applied pressure. While the EPF is a function of the charge of the particle, the EOF is only dependent upon the charge of the pore, and therefore the two forces increase with the applied voltage at different rates. Furthermore, these forces have different dependencies on pore geometry. Increasing the channel-like character of conical pores spreads the electric field over a larger sensing zone, which would be expected to reduce EPF. By contrast, increased pore channel length has been observed to increase the EOF.[10, 21] Although the geometry of the GNPs used in this study is conical, these GNPs

have significant channel-like character due to the small cone angle (~ 2^{o}), and this may be a key to achieving the delicate balance of the forces controlling particle dynamics.

Without applied pressure, the minimum particle velocity occurs at zero voltage, but with suitable pressure we are able to shift the minimum velocity point to a voltage range that is convenient for measurements. Thus, for a particular pipette we applied a pressure necessary to place the transition voltage in this range; that is, the voltage at which particle velocities are minimized due to equivalence of the forces drawing particles into the pore (primarily the EPF and fluid flow caused by applied pressure) and those driving particles out of the pore (primarily the EOF). Firnkes *et al.* were able to balance the EPF and EOF by finding a pH at which the zeta potential of the pore and of the molecule studied were equal.[10] However, simply eliminating the driving force does not allow for general control of particle dynamics. For the conical pores used in this study, the EOF appears to increase with voltage at a greater rate than the EPF, and we observed translocations in the opposite direction of electrophoresis under atmospheric conditions. Zhang *et al.* also demonstrated DNA translocating in the opposite direction of electrophoresis and attributed this to a large EOF.[12] In the experiments in Figure 4.6, we took advantage of the large change in EOF with respect to voltage, and were able to control the entire range of particle velocities from near zero to the limit of the electronic bandwidth filtering of the amplifier (10 kHz), in both the inward and outward direction and between +100 and +500mV.

4.3.5 Finite element simulations

Finite element simulations using COMSOL Multiphysics were performed to provide a more quantitative description of the experimental results at each of the salt concentrations studied. We used a quasisteady method which assumes that the fluid and particle are in equilibrium.[22-24] Based on the assumption that the sum of the hydrodynamic drag and electrokinetic forces, which were contributed by pressure-driven flow and electro-osmosis flow, on the nanoparticle are zero, the velocity of the particle may be iteratively determined using the Newton-Raphson method to solve the following equations from an appropriate initial guess. Details of the simulation geometry and boundary conditions are provided in 4.5 Appendix.

A quasisteady force balance is expressed as:

$$\mathbf{F}_{\text{total}} = \mathbf{F}_{\text{H}} + \mathbf{F}_{\text{E}} = 0 \tag{4.1}$$

where $\mathbf{F}_{\text{H}}$ and $\mathbf{F}_{\text{E}}$ are hydrodynamic force and electrokinetic force exerted on the particle, respectively. These forces are given by eqs 4.2 and 4.3:

$$\mathbf{F}_{\text{H}} = \int (\mathbf{T}_{\text{H}} \bullet \mathbf{n}) dS \tag{4.2}$$

$$\mathbf{F}_{\text{E}} = \int (\mathbf{T}_{\text{E}} \bullet \mathbf{n}) dS \tag{4.3}$$

where $\mathbf{T}_{\text{H}}$ and $\mathbf{T}_{\text{E}}$ are the hydrodynamic stress tensor and the Maxwell stress tensor, respectively, $\mathbf{n}$ is the unit normal vector, and S represents the surface of the nanoparticle.

The Navier-Stokes equation describes the laminar flow of the incompressible fluid.

$$\mathbf{u}\nabla\mathbf{u} = \frac{1}{\rho}(-\nabla p + \eta\nabla^2\mathbf{u} - F(\sum_i z_i c_i)\nabla\Phi) \tag{4.4}$$

In eq 4.4, the body force component $-\frac{F}{\rho}(\sum_i z_i c_i)\nabla\Phi$ originates from the electro-osmosis. $\mathbf{u}$ and Φ are the local position-dependent fluid velocity and potential, c_i and z_i are concentration and charge of species i in solution, p is the pressure and F is Faraday's constant. The solution density ρ = 1000 kg/m^3 and the dynamic viscosity η = 0.001 Pa•s, respectively, correspond approximately to the aqueous solution. The particle velocity $\mathbf{u}$ corresponds to the boundary velocity between the particle surface and surrounding fluid, eq 4.4.

The ion distribution and potential profile in the system are modeled by the Nernst-Planck-Poisson equations as below:

$$\mathbf{J}_i = -D_i\nabla c_i - \frac{Fz_i}{RT}D_i c_i\nabla\Phi + c_i\mathbf{u} \tag{4.5}$$

$$\nabla^2\Phi = -\frac{F}{\varepsilon}\sum_i z_i c_i \tag{4.6}$$

In eq 4.5, $\mathbf{J}_i$ and D_i are the ion flux vector and diffusion coefficient of species i in solution, respectively. D_{Na^+} = 1.33 × 10^{-9} m^2/s and D_{Cl^-} = 2.03 × 10^{-9} m^2/s. The absolute temperature T = 298 K, and the gas constant R = 8.314 J/K. ε is the dielectric constant of

78. Figure 4.8 presents results of the FEA simulations corresponding to the experiments in Figure 4.6. Figure 4.8a shows velocity profiles and streamlines along the pore axis corresponding to the experimental conditions (ζ = -15 mV, 0.2 M NaCl and 0.35 atm external pressure) in Figure 4.6b (turquoise line). Using a cone angle of 1.87°, the general trends seen in the experiment were reproduced, with particles entering the pore at 100 mV, exiting the pore at 500 mV, and a crossover point occurring at ~200 mV (simulated) and ~250 mV (experimental). In Figure 4.8b and c, simulation parameters were varied to reproduce the velocity trends seen in Figure 4.6a and b, respectively, for the differently charged particles at varying salt concentrations. A better quantitative match with experimental results is seen at the lower salt concentrations (Figure 4.8c). Specifically, the same velocity trends are seen as particle charge and the ionic strength of the solution are varied, with velocity reversal occurring in the 100 – 500 mV range. At higher salt concentration (Figure 4.8b) the agreement with the experimental measurements is weaker, but still qualitatively captures the trend in the experimental results. Given the approximations in the modeling parameters and the uncertainty in the nanopore geometry, the governing equations employed in the FEA simulations provide a very satisfactory description of the particle motion.

4.3.6 The effects of salt concentration and particle charge on nanoparticle dynamics

Experiments in 0.1 M and 0.2 M NaCl solutions required a much larger applied pressure (-0.35 atm) than those in 1.0 M NaCl (-0.047 atm); the data are presented on a separate graph to accommodate a sufficiently wide range of particle velocities (Figure

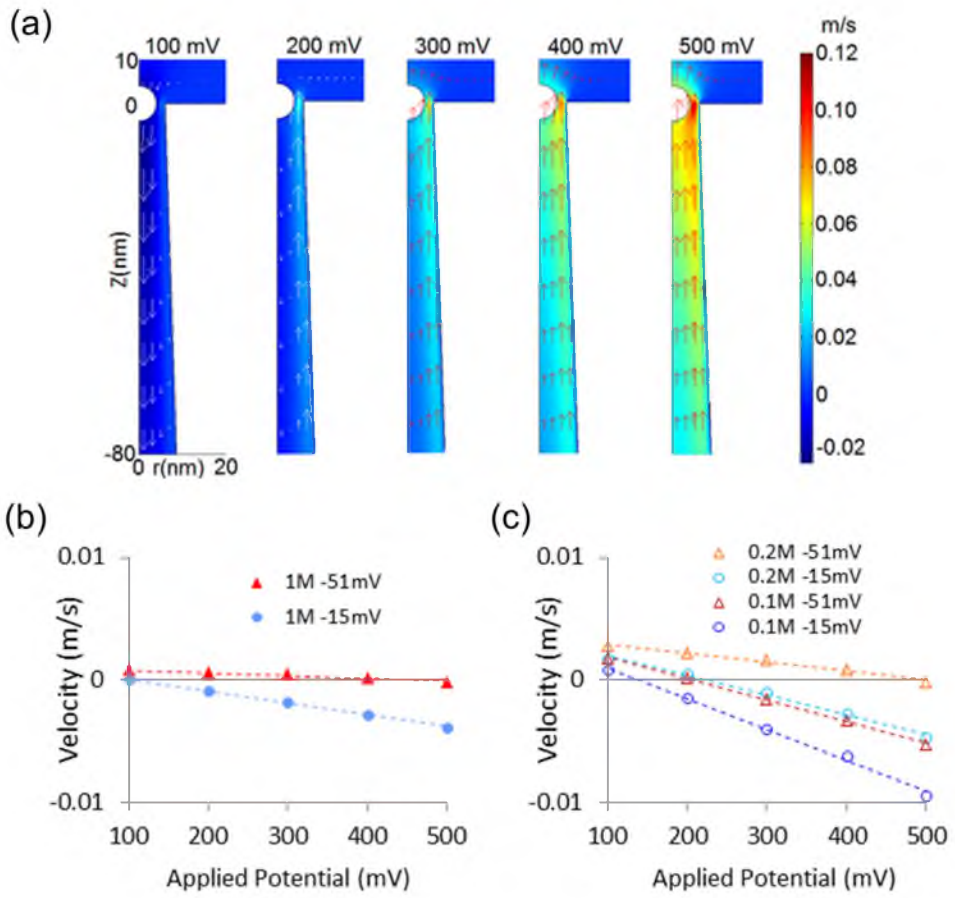

Figure 4.8. Simulations of nanoparticle velocities at the pore orifice. (a) Simulated velocity profile for a nanoparticle (ζ= -15 mV) in a 0.2 M NaCl solution, at 0.35 atm pressure and applied voltages between 100 and 500 mV corresponding to the turquoise lines in Figure 4.6b and Figure 4.8c. (b) and (c) are plots of particle velocities corresponding to the data in Figure 4.6a and b, respectively. The data point colors and symbols follow the same scheme used to plot experimental data in Figure 4.6. Parameters and other details of the finite element simulation are presented in 4.5 Appendix.

4.6b). The need for higher pressure would be expected from the increased Debye lengths at lower salt concentrations, which generate larger EOFs along the pore surface. Since the EOF at the transition voltage is larger than the applied pressure, we can say that pressures greater than 0.3 atm are generated in 0.2 M NaCl at 300 mV, and in 0.1 M NaCl comparable pressures are generated at 200 mV. By contrast, Takamura *et al.* reported the fabrication of "extremely high pressure" electro-osmotic pumps of 0.05 atm for 120 nm × 100 μm channels subjected to 40 volts.[25]

Examining the velocities of differently charged particles at a particular combination of salt concentration and applied voltage reveals the effect of particle charge. Under these conditions, the applied pressure and EOF are identical, and therefore the remaining electrophoretic force decreases the velocity of negative particles moving out of the pore and increases their velocities as they move in. This explains why the velocity trend lines for the more highly charged (ζ = -51 mV) particles were always above those for the less highly charged (ζ = -15 mV) particles (Figure 4.6). It should be noted that the 0.1 M NaCl velocities fall below the 0.2 M NaCl due to an increased EOF and not because of charge effects.

4.3.7 Factors affecting resistive pulse peak shape

It is well known that the path of a particle through a conical nanopore determines the shape of a resistive pulse event. Inhomogeneity of the electric field within the sensing zone due to a stronger field near pore walls has been shown to cause as much as a 15% deviation in peak amplitude for particles that do not travel straight through the center of the pore (off-axial translocations).[26] Interaction of particles with pore walls can also

lengthen translocation times, a factor that must be taken into account for analysis based upon peak widths.[9] The ability to slow particle velocity to the degree achieved in our experiments allows a closer examination of the factors that affect translocation kinetics. This is illustrated by the insets in Figure 4.6, which demonstrate clear peak shape differences during the course of translocations. In particular, we have observed the steep side of a typical asymmetric translocation exhibiting biphasic character to differing degrees (compare the rightmost inset translocation with both the second and the fifth translocation from right). These stages of resistance change may be explained by contributions from an inhomogeneous electric field, pore wall interactions, diffusion, and/or possibly a second EOF that arises from the double layer associated with the particle itself. An additional complicating factor could stem from the possibility that our pores were not entirely smooth throughout the sensing zone, although the observation of numerous "ideally shaped" translocations[27] argues against this possibility.

4.4 Conclusion

In summary, we have demonstrated that the dynamics of 8-nm nanoparticle translocations through micropipette GNPs can be controlled, and we have gathered important information about the interplay of electrophoretic, electro-osmotic, and pressure forces by studying translocation velocity as a function of particle charge, salt concentration, and applied pressure. Detection and characterization of nanoparticles has a growing number of applications across different disciplines, from research and diagnostics to drug delivery, detection of nanoparticle waste released by industrial nanotechnology applications, and biosensing. Overcoming the problem of excessive

particle velocities through appropriate choice of nanopores and observation parameters is an important step toward better understanding and applying these technologies. Controlling nanoparticle dynamics allows nanopore sensing to advance from mere *detection* of nanoparticles into the realm of nanoparticle *characterization* in a previously unattainable range.

4.5 Appendix

Pressure controlled reversal of particle translocation, calculation of Au nanoparticle charge density, and details of the finite-element simulations used to compute nanoparticle velocities are shown in Figure 4.9 to Figure 4.12.

4.5.1 Nanoparticle dynamics control by applied pressure

Figure 4.9 shows the nanoparticle *i-t* traces at different applied pressures.

4.5.2 Surface charge density of the Au nanoparticle estimated from the zeta potential in an extremely diluted electrolyte solution

The effective surface charge of the Au nanoparticles was estimated by finite-element simulation, assuming that the simulated surface potential is equal to the measured zeta potential. Experimentally, the zeta potential of nanoparticles were measured in deionized (DI) water which contains ~10^{-7} M hydroxide (OH^-) and hydronium ion (H_3O^+) due to water's self-dissociation. Considering trace ions remain in the DI water, the electrolyte was set as 10^{-6} M KCl in the simulation. An arbitrary surface charge density was initially set on the Au nanoparticle surface, and then Poisson and

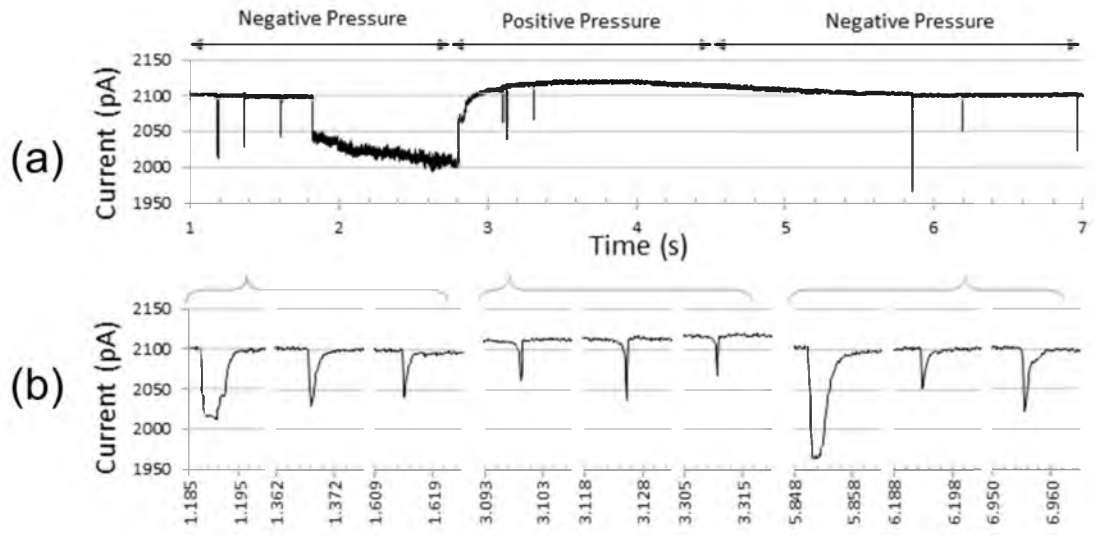

Figure 4.9. Forward and reverse translocation of three nanoparticles as a function of the applied pressure. A nanopore having a resistance of 117 MΩ measured in 1.0 M NaCl was used to observe 8-nm diameter Au nanoparticles at constant applied potential (250 mV). In (a), three particles enter the pore between 1.2 and 1.6 s as negative pressure (-0.25 atm) is applied to the pipette. A pore block between 1.8 and 2.8 s is removed by applying a positive pressure (0.5 atm), pushing the three particles out of the pipette between 3.1 and 3.3 s. A negative pressure (-0.25 atm) is then applied at 4.5 s to draw the three particles back through the nanopore between 5 s and 7 s. Although the standard deviation in the particle size distribution was only ± 0.6 nm, distinct peak shapes seen in the *i-t* expansions shown in (b) reflect subtle differences in the particle sizes, and allow identification of individual particles. The applied positive pressure was greater than the applied negative pressures, resulting in increased translocation velocity and therefore narrower peak widths.

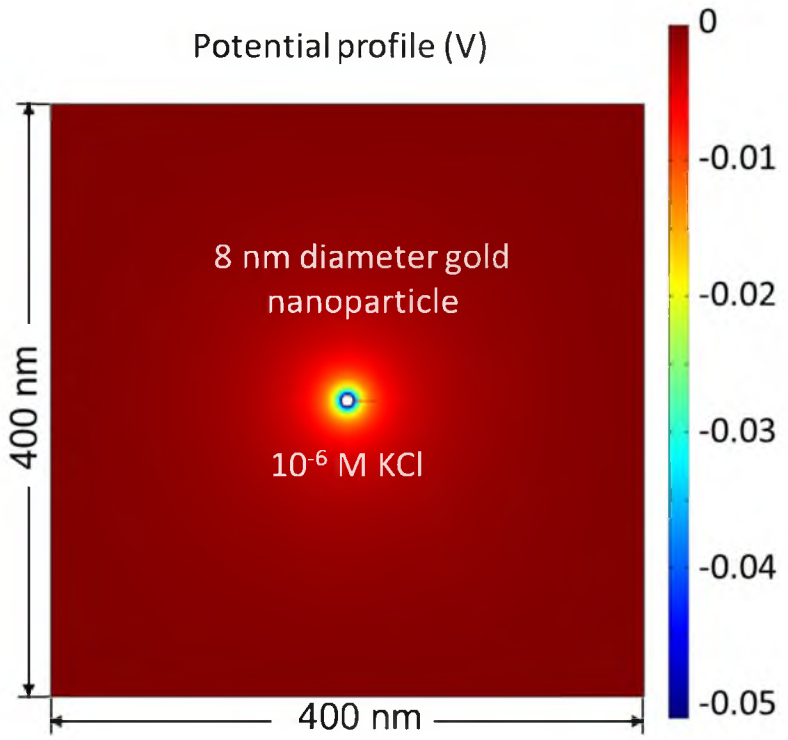

Figure 4.10. Simulated potential profile generated by a -9 mC/m^2 charged Au nanoparticle with a diameter of 8 nm.

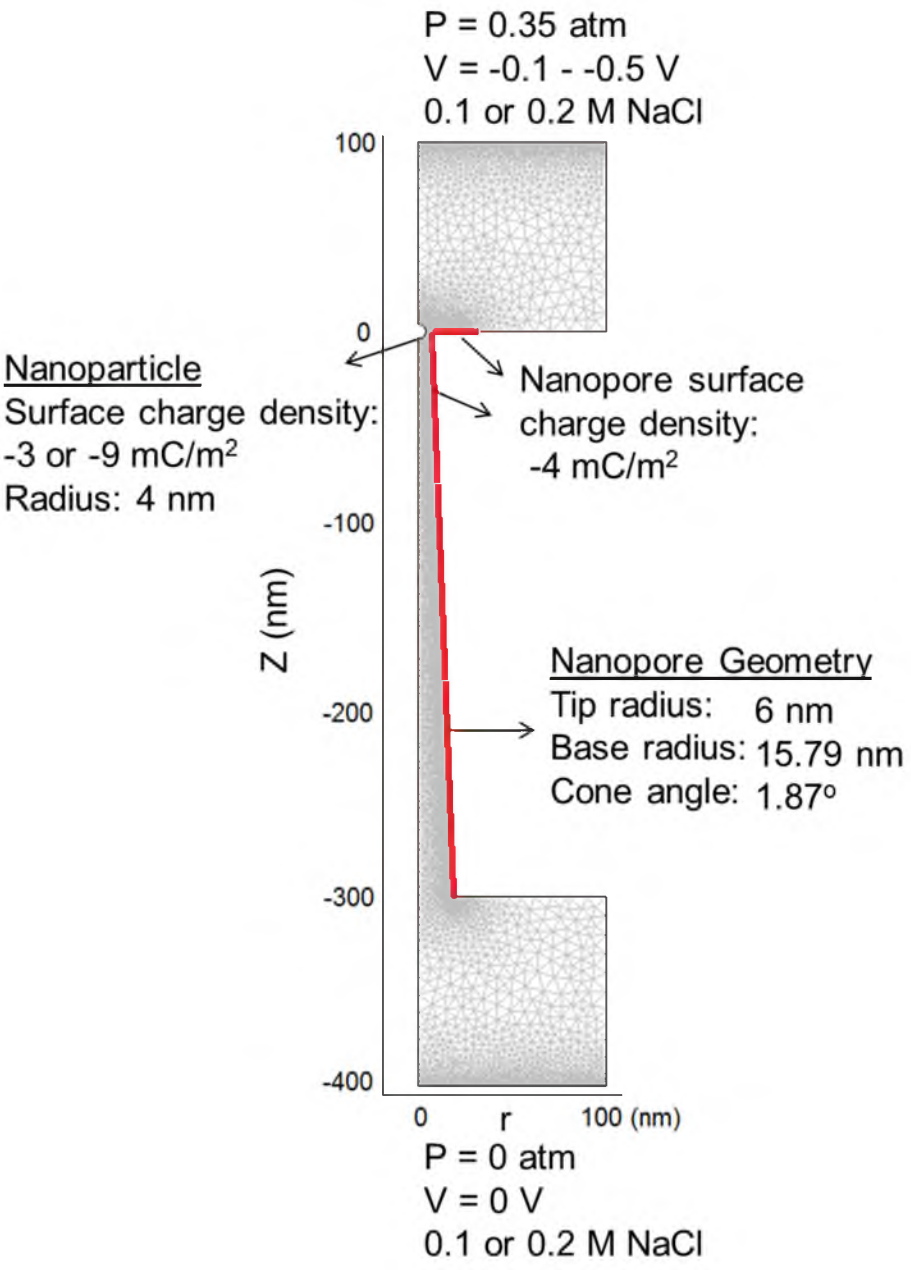

Figure 4.11. Geometry and boundary conditions for the finite-element simulation in a 100 mM or 200 mM NaCl solution and P = 0.35 atm.

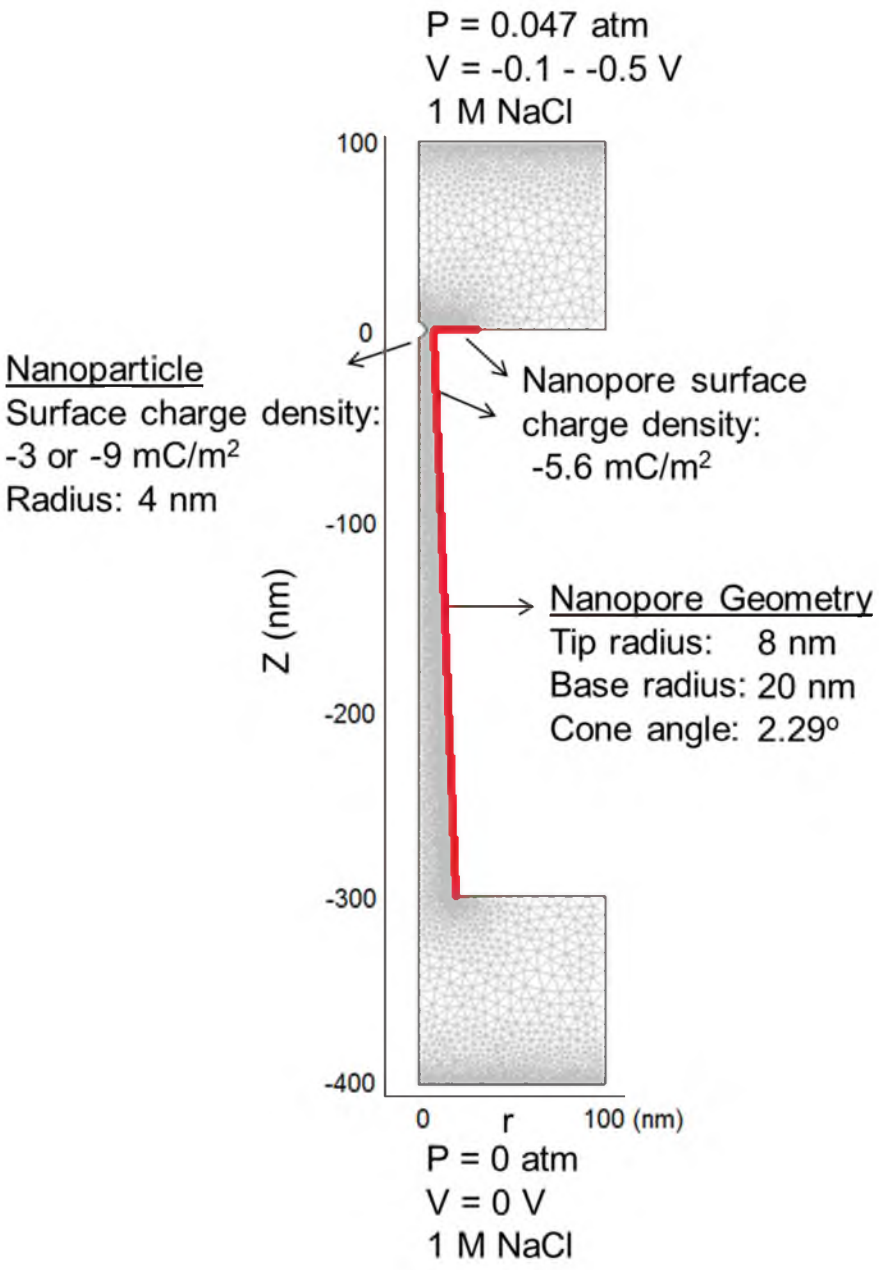

Figure 4.12. Geometry and boundary conditions for the finite-element simulation in a 1.0 M NaCl solution with P = 0.047 atm.

Nernst-Planck equations were iteratively solved to obtain a surface charge density value, which yields a surface potential within 10% of the measured zeta potential. Surface charge densities of -3 mC/m^2 and -9 mC/m^2 were obtained which produce simulated surface potentials of -17 mV and -51 mV, respectively, compared with measured ζ = -15 mV and -51 mV. Figure 4.10 shows the simulated potential profile generated by a -9 mC/m^2 charged gold nanoparticle with a diameter of 8 nm.

4.5.3 The geometry and boundary conditions for a simulation of the particle velocity in 100 mM and 200 mM NaCl solutions

In the simulation, an 8-nm diameter gold nanoparticle with a surface charge density of -3 mC/m^2 or -9 mC/m^2 (corresponding to ζ = -15 mV or -51 mV) was placed at the nanopore orifice, $z = 0$ and $r = 0$, as 0.35 atm and -100 mV to -500 mV were applied across the nanopore. A mesh size < 0.5 nm was used at the nanopore's charged surface (red line highlighted) as well as the nanoparticle surface, which is sufficient to resolve the electrical double layer.

The nanopore surface charge density and geometry were estimated based on the nanopore ion current and ion current rectification ratio, defined as the ratio of currents at -500 mV and 500 mV (inside *vs.* outside nanopore). In 100 mM NaCl, a nanopore surface charge density of -4 mC/m^2 produces a simulated rectification ratio of ~1.13 while the experimental value is ~1.2; the simulated current at 500 mV is 550 pA, while the experimental value is 600 pA. Figure 4.11 shows the geometry, mesh and boundary conditions used in the simulation.

4.5.4 The geometry and boundary conditions for a simulation of the particle velocity in 1.0 M NaCl solution

The boundary conditions and mesh setting were the same as in Figure 4.11, except that the pressure was decreased to 0.047 atm and the bulk salt concentration was increased to 1.0 M, corresponding to experimental parameters. Because 1.0 M NaCl screens the surface charge and almost eliminates ion current rectification, a different method was used to determine nanopore geometry and surface charge. A larger tip radius (8 nm) was used since the nanopore employed had a lower resistance (110 MΩ *vs.* 125 MΩ at 1.0 M NaCl), and the amplitude of resistive pulse blockages in Figure 4.6a (~70 pA) were only ~2-fold larger than those in Figure 4.6b, in contrast to the ~5 to 10-fold increase expected (see inset scales in Figure 4.6). An increased surface charge density of -5.6 mC/m^2 was used since more highly concentrated salt solutions enhance the dissociation of surface silanol groups. Figure 4.12 shows the geometry, mesh, and boundary conditions used in the simulation.

4.5.5 Considerations on the polarization of the nanoparticle surface charge

The simulations above assume that the nanoparticle is an insulator. Since the nanoparticles used are conductors having an organic polymer coating, further simulations were carried out to determine whether surface polarization of the particle could be significant. When the simulation was redone assuming a conductive particle, the surface charge density (~ -10^{-2} C/m^2) changed by less than 0.1%.

4.6 References

(1) Domingos, R.; Baalousha, M.; Ju-Nam, Y.; Reid, M.; Tufenkji, N.; Lead, J.; Leppard, G.; Wilkinson, K. *Environ. Sci. Technol.* **2009**, *43*, 7277.

(2) DeBlois, R. W.; Bean, C. P.; Wesley, R. K. A. *Journal of Colloid and Interface Science* **1977**, *61*, 323–335.

(3) Lan, W.-J.; Holden, D. A.; Zhang, B.; White, H. S. *Anal. Chem.* **2011**, *83*, 3840–3847.

(4) Wu, H.-C.; Astier, Y.; Maglia, G.; Mikhailova, E.; Bayley, H. *J. Am. Chem. Soc.* **2007**, *129*, 16142–16148.

(5) Wanunu, M.; Sutin, J.; Ben McNally; Chow, A.; Meller, A. *Biophysical Journal* **2008**, *95*, 4716–4725.

(6) Wanunu, M.; Dadosh, T.; Ray, V.; Jin, J.; McReynolds, L.; Drndić, M. *Nature Nanotech.* **2010**, *5*, 807–814.

(7) Fologea, D.; Uplinger, J.; Thomas, B.; McNabb, D. S.; Li, J. *Nano Lett.* **2005**, *5*, 1734–1737.

(8) Berge, L. I.; Feder, J.; Jossang, T. *Review of Scientific Instruments* **1989**, *60*, 2756.

(9) Gershow, M.; Golovchenko, J. A. *Nature Nanotech.* **2007**, *2*, 775–779.

(10) Firnkes, M.; Pedone, D.; Knezevic, J.; Döblinger, M.; Rant, U. *Nano Lett.* **2010**, *10*, 2162–2167.

(11) Ito, T.; Sun, L.; Crooks, R. M. *Anal. Chem.* **2003**, *75*, 2399–2406.

(12) Zhang, B.; Wood, M.; Lee, H. *Anal. Chem.* **2009**, *81*, 5541–5548.

(13) Vogel, R.; Anderson, W.; Eldridge, J.; Glossop, B.; Willmott, G. *Anal. Chem.* **2012**, *84*, 3125–3131.

(14) Venkatesan, B. M.; Bashir, R. *Nature Nanotech.* **2011**, *6*, 615–624.

(15) Howorka, S.; Siwy, Z. *Chem. Soc. Rev.* **2009**, *38*, 2360.

(16) Gao, C.; Ding, S.; Tan, Q.; Gu, L.-Q. *Anal. Chem.* **2009**, *81*, 80–86.

(17) Li, G.-X.; Zhang, Z.-X.; Lin, X.-Q. *Chinese Journal of Analytical Chemistry* **2010**, *38*, 1698–1702.

(18) White, H. S.; Bund, A. *Langmuir* **2008**, *24*, 2212–2218.

(19) Vercoutere, W.; Winters-Hilt, S.; Olsen, H.; Deamer, D.; Haussler, D.; Akeson, M. *Nature Biotech.* **2001**, *19*, 248–252.

(20) Lan, W.-J.; White, H. S. *ACS Nano* **2012**, *6*, 1757–1765.

(21) Yusko, E. C.; An, R.; Mayer, M. *ACS Nano* **2010**, *4*, 477–487.

(22) Ye, C.; Sinton, D.; Erickson, D.; Li, D. *Langmuir* **2002**, *18*, 9095–9101.

(23) Yalcin, S. E.; Lee, S. Y.; Joo, S. W.; Baysal, O.; Qian, S. *J. Phys. Chem. B* **2010**, *114*, 4082–4093.

(24) Jubery, T. Z.; Prabhu, A. S.; Kim, M. J.; Dutta, P. *Electrophoresis* **2012**, *33*, 325–333.

(25) Takamura, Y.; Onoda, H.; Inokuchi, H.; Adachi, S.; Oki, A.; Horiike, Y. *Electrophoresis* **2003**, *24*, 185–192.

(26) Kozak, D.; Anderson, W.; Vogel, R.; Trau, M. *Nano Today* **2011**, *6*, 531–545.

(27) Lan, W. J.; Holden, D. A.; Liu, J.; White, H. S. *J Phys. Chem.* **2011**, *115*, 18445–18452.

CHAPTER 5

ELECTROGENERATION OF SINGLE NANOBUBBLES AT SUB-50 NM RADIUS PLATINUM NANODISK ELECTRODES

5.1 Introduction

Research on interfacial nanobubbles has greatly advanced during the past decade, including the development of new methods of generating[1-4] and detecting nanobubbles,[5-16] as well as the development of the theory and mechanism of nanobubble formation and stabilization.[17-21] At present, it is possible to generate large ensembles of nanobubbles of different gas types at hydrophobic surfaces (*e.g.*, perfluorodecyltrichlorosilane (PFDTS) and highly orientated hydrophobic pyrolytic graphite (HOPG)) using the solvent exchange technique[5] or by the electrolysis of water[1]. Interfacial nanobubbles have been observed and characterized by tapping mode atomic force microscopy (TMAFM).[4-13] In recent experimental reports, interfacial nanobubbles were found to exist for hours or days, in contrast to the expected short lifetime due to rapid gas dissolution.[22] Several mechanisms have been proposed to explain the observed long lifetime of nanobubbles, including the role of impurities at the interface,[18, 23, 24] dynamic steady-state,[3,18] and contact line pinning,[17,21] but still no general agreement has been yet reached on the actual mechanism. Not only is the stabilization mechanism under debate, but the mechanism of nanobubble formation also remains unclear. It has been proposed that interfacial

nanobubbles result from a supersaturation of gas at the interface.[17,25] A quartz crystal microbalance study by Zhang *et al.* suggests that this process occurs in less ~1 min.[26] However, Seddon *et al.*[27] and Dong *et al.*[28] recently reported the formation of surface nanobubbles in solutions that were not supersaturated by the corresponding gas. How nanobubbles form at the interface and why they remain stable are still open questions.

In this chapter, we present a new approach for investigating the formation and stability of a nanobubble. Instead of generating a large ensemble of nanobubbles at a macroscopic surface, a Pt nanodisk electrode is used to electrochemically generate a single H_2 nanobubble by reducing protons in a strong sulfuric acid solution, Figure 5.1. The nanoscale dimension of the nanoelectrode itself provides exquisite sensitivity for detecting small changes near or at the electrode surface,[29-32] while fast electrochemical measurements allow study of the dynamics of nanobubble formation. High spatial and time resolutions make the nanodisk electrode a powerful platform to study the formation and stabilization of nanobubbles. As detailed below, the formation of a single nanobubble at the Pt nanodisk electrode can be readily detected from the current drop in the reduction of H^+ caused by the blockage of the electrode surface. Our results suggest that a critical H_2 concentration profile near the nanoelectrode surface is required to initiate nanobubble formation. Additionally, rapid *i-t* recording of the current drop provides insight into the dynamics of nanobubble formation, while measurement of the residual current after the formation of a nanobubble provides insight into the mechanism by which a nanobubble remains stable. We demonstrate that a residual current of several hundred pA, corresponding to H_2 electrogeneration at the Pt/gas/liquid interface, balances the rate of H_2 dissolution from the nanobubble.

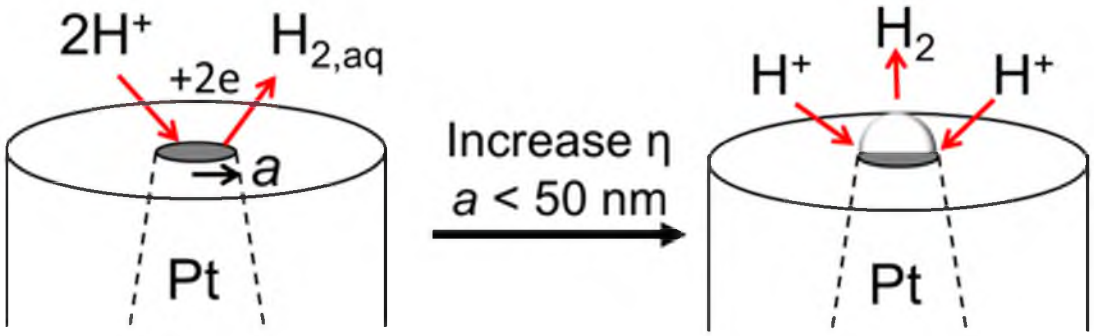

Figure 5.1. Schematic representation of the electrochemical formation of an individual nanobubble at a Pt nanodisk electrode with a radius a < 50 nm. The Pt nanodisk is shrouded in glass. The hemispherical shape of the nanobubble is drawn here for schematic purposes and is unlikely to represent the actual shape.

5.2 Experimental section

5.2.1 Chemicals

Sulfuric acid (98%, ACS grade, EMD) was used as received. All aqueous solutions were prepared, using water (18 MΩ·cm) from a Barnstead E-pure water purification system.

5.2.2 Nanodisk electrode fabrication and characterization

Platinum nanodisk electrodes were fabricated according to previously reported procedures from our laboratory.[33] Briefly, a Pt wire attached to a tungsten rod was electrochemically sharpened in a NaCN solution and then sealed in a glass capillary (Dagan Corp., Prism glass capillaries, SB16, 1.65 mm outer diameter, 0.75 mm inner diameter, softening point 700 °C) using a H_2/air flame. The capillary was then polished with silicon carbide polishing papers (400 grit/p800 - 1200 grit/p4000) until a Pt nanodisk was exposed, as indicated by the use of an electronic feedback circuit.[33] The radii of the resulting nanodisks, a, were determined from the voltammetric steady-state diffusion-limited current, i_d, for the oxidation of 5 mM ferrocene (Fc) dissolved in acetonitrile containing 0.1 M tetrabutylammonium hexafluorophosphate ($TBAPF_6$). The radii were calculated using the equation

$$i_d = 4nFDC^*a \tag{5.1}$$

where a is the radius of the nanodisk electrode, D (2.5×10^{-5} cm^2/s[33]) and C^* are the diffusion coefficient and the bulk concentration of Fc, respectively, and n is the number

of electrons transferred per molecule (in this case equal to 1). The experimental steady-state voltammograms used to measure the electrode radii are presented in 5.5 Appendix.

5.2.3 Electrochemical apparatus

A Dagan Cornerstone Chem-Clamp potentiostat and a Pine RDE4 (used as the waveform generator) were interfaced to a computer through a PCI data acquisition board (National Instruments) to collect the *i-V* and *i-t* data. The current from the Dagan potentiostat was passed through a 10 kHz low-pass filter. For currents > 100 nA using larger Pt disk electrodes, the Pine RDE 4 was used alone as the potentiostat/programmer. *i-V* curves were recorded by virtual instrumentation written in LabVIEW (National Instruments) at a data acquisition rate of 150 kHz. A Ag/AgCl (3 M NaCl) electrode was used as the counter/reference electrode.

5.2.4 Finite element simulation

The finite element simulations were performed to study the nanobubble formation and stabilization mechanism using COMSOL Multiphysics 3.5 (Comsol, Inc.) on a high performance desktop PC. The details about the simulation geometry, mesh, and boundary conditions are provided in 5.5 Appendix.

5.3 Results and discussion

5.3.1 Electrochemical formation of a single nanobubble

Figure 5.2a shows a typical cyclic voltammogram (CV) recorded at a 27-nm-radius Pt nanodisk electrode immersed in *deoxygenated* 0.5 M H_2SO_4 (scan rate = 100

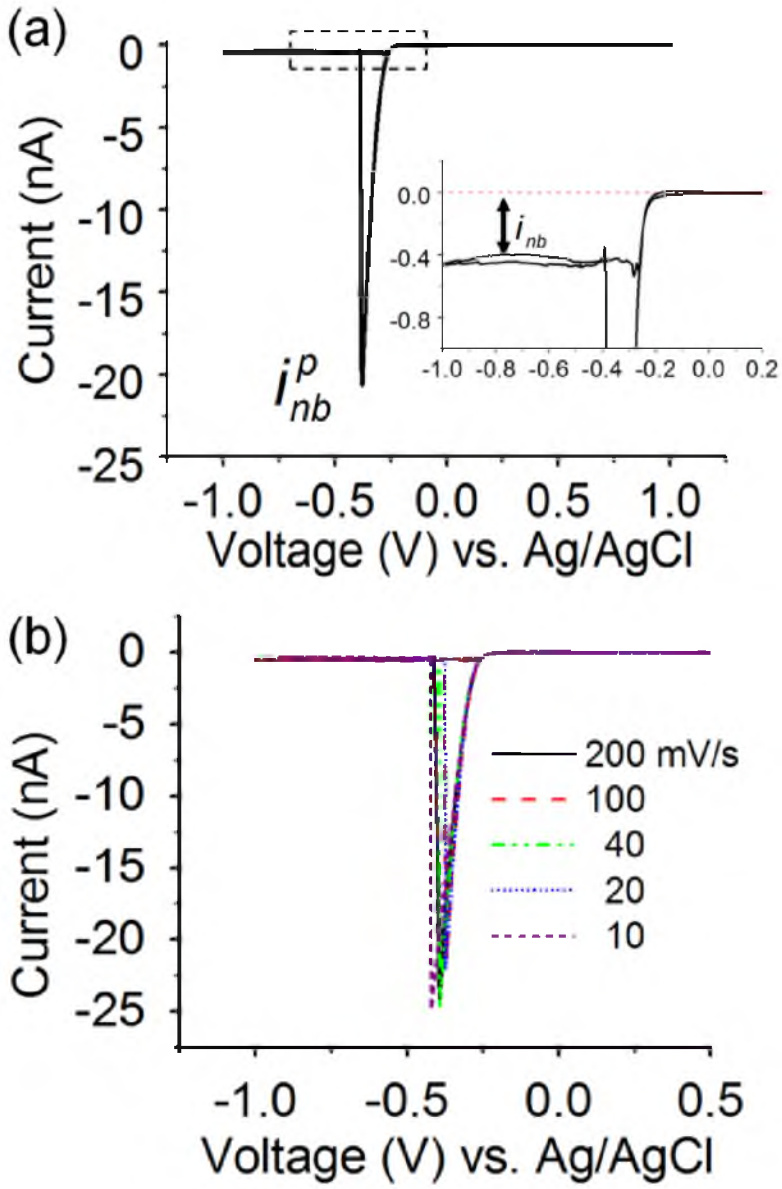

Figure 5.2. Cyclic voltammograms of hydrogen nanobubble formation at a nanoelectrode. (a) Cyclic voltammogram recorded at a 27-nm-radius Pt electrode immersed in a deoxygenated 0.5 M H_2SO_4 solution (scan rate = 100 mV/s). The transport-limited current associated with the transport-limited electroreduction of H^+ drops suddenly at ~-0.4 V *vs* Ag/AgCl due to the nucleation and rapid growth of a H_2 nanobubble. The peak current at which nanobubble formation occurs is labeled as i_{nb}^{p}. The insert shows a residual current i_{nb} of -0.4 nA after the formation of a nanobubble. (b) Cyclic voltammetric response for the same 27-nm-radius Pt electrode recorded at scan rates ranging from 10 to 200 mV/s.

mV/s). The H_2SO_4 solution was deoxygenated by bubbling the solution with N_2 for about half an hour. At potentials positive of -0.25 V *vs.* Ag/AgCl, the voltammogram displays very small currents (< 10 pA) resulting from the double layer capacitance and the absorption/desorption of hydrogen and oxygen species at the Pt surface.[34,35] As the voltage is scanned negative of -0.25 V, corresponding to the thermodynamic potential for the reduction of protons ($E^0_{(H^+/H_2)}$), the current increases rapidly until it reaches a peak value, i^p_{nb}, at ~-0.4 V *vs.* Ag/AgCl. Within this range, the *i-V* response is smooth and continuous, indicating no bubble formation. For the 27-nm-radius electrode, the i^p_{nb} of ~ -21 nA (negative sign denotes a cathodic current) is approximately 20% of the predicted proton-diffusion-limited current, i_d = -97 nA (eq 5.1, using a = 27 nm, D_{H^+} = 9.3 × 10^{-5} cm^2/s,[36] and C^* = 1 M). After passing through the peak current, the current decreases to a residual current value i_{nb} of ~-450 pA. We interpret this voltammetric response as corresponding to the formation of a single nanobubble at the 27-nm-radius Pt disk which blocks a large fraction (> 95%) of the active electrode surface. The inset of Figure 5.2 shows an enlargement of the residual current following nanobubble formation. The observation of a residual current for H^+ reduction suggests that the nanobubble at the electrode is at a *dynamic equilibrium,* in which electrolytically generated H_2 flows into the nanobubble and balances the diffusion of H_2 at the nanobubble/liquid interface.

On the reverse voltammetric scan from -1.0 V towards positive potentials (at scan rates up to 1 V/s) we did not observe an anodic peak at potentials positive of $E^0_{(H^+/H_2)}$ corresponding to the oxidation of the H_2 nanobubble or H_2 dissolved in the solution. This result suggests that the H_2 bubble dissolves rapidly on the voltammetric time scale as

soon as H^+ is no longer being reduced. Diffusion of dissolved H_2 away from a 27 nm-radius electrode is too rapid to allow its detection at the scan rates used in this study.

Figure 5.2b shows that the cyclic voltammogram, including the value of the peak current, i_{nb}^{p}, are essentially independent of scan rate between 10 and 200 mV/s. Prior to nanobubble formation, the current is limited by a combination of H^+ transport and reduction kinetics at the nanoelectrode.[37, 38] When the current reaches the critical value of ~-21 nA, it drops rapidly, indicating a fast nanobubble formation process. The *i-V* response of an 11-nm-radius nanodisk electrode exhibits a very similar scan-rate independent response with i_{nb}^{p} ~-10 nA (5.5 Appendix).Voltammograms corresponding to the formation of H_2 nanobubbles were reproducible over multiple scans between 1 to -1 V *vs.* Ag/AgCl, suggesting that bubble formation did not readily damage the Pt surface.

To investigate the dynamics of nanobubble formation, we recorded the *i-t* of the 27-nm-radius Pt nanodisk while scanning the electrode potential from 1 V to -1 V at a scan rate of 100 mV/s, Figure 5.3. The expansion of the *i-t* trace, Figure 5.3b, clearly shows that the *i-t* response is described by two time constants, with more than 50% of the current decrease occurring during the first 200 μs and then a slower decay (to the steady-state value of ~-1 nA) occurring in a few milliseconds. This response suggests a two-step mechanism of nanobubble formation. Note that the potentiostat temporal resolution is limited by 10 kHz low-pass filter (see Experimental section); thus, the time constant for the first step is probably shorter than the ~100 μs timescale observed in the measurement.

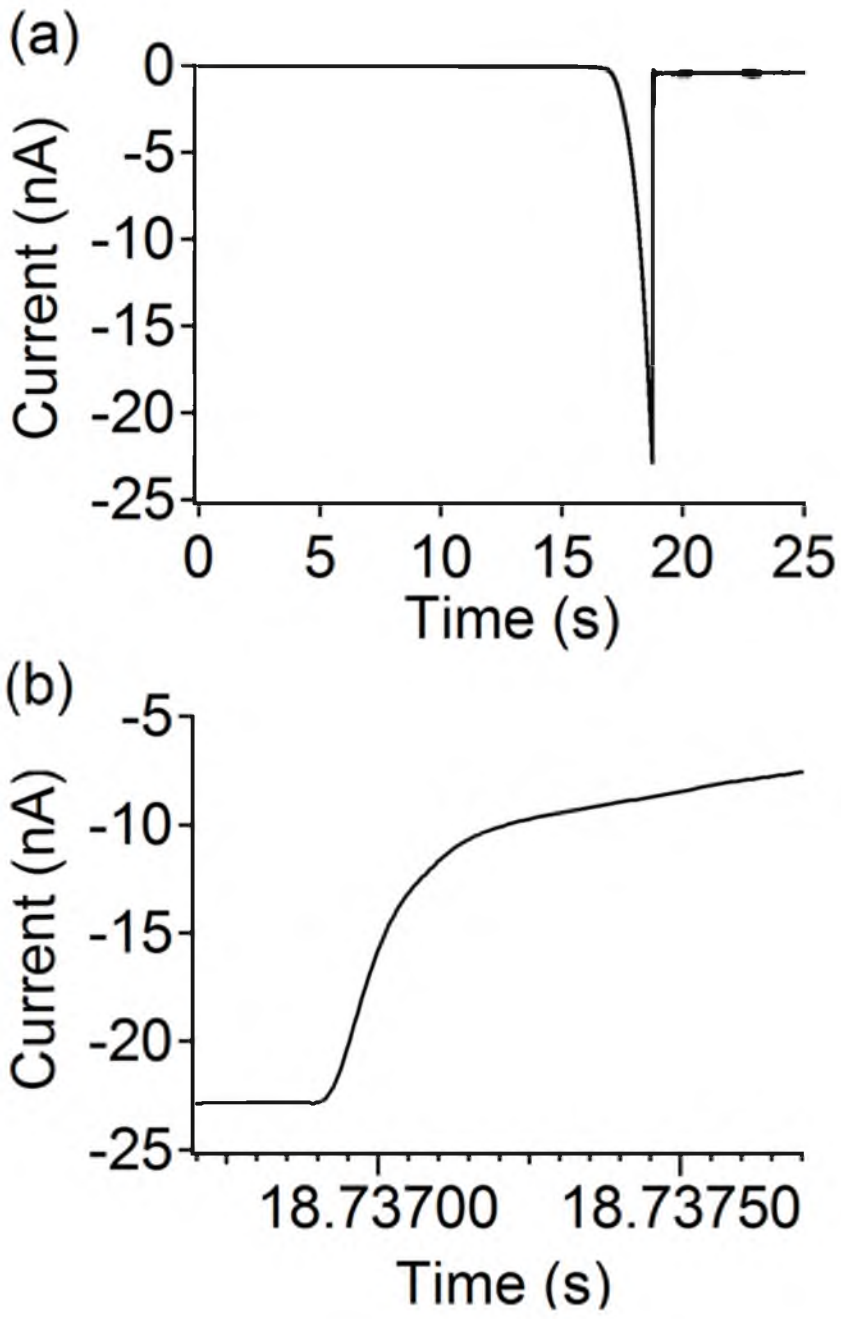

Figure 5.3. A typical *i-t* trace during nanobubble formation. (a) *i-t* trace recorded while scanning the voltage at 100 mV/s from 1 V to -1 V at the 27-nm-radius Pt nanodisk immersed in 0.5 M H_2SO_4. (b) Expansion of (a) shows that the formation of a nanobubble is described in a two-step mechanism, with the initial step occurring on a time scale of a few hundred microseconds, followed by a slower growth process on the time scale of a few milliseconds. In this particular example, the current reaches the steady-state residual value, i_{nb}, is ~3 ms. The temporal resolution of the measurement is limited by the instrumental10 kHz bandwidth.

5.3.2 Possible mechanism of electrochemical nanobubble formation

The *i-t* responses suggest a two-step formation of a nanobubble when the current reaches i_{nb}^{p}. We hypothesize that the H_2 concentration at the nanoelectrode surface is sufficiently high to nucleate a nanobubble at the Pt nanodisk surface when the current reaches i_{nb}^{p}, representing the first step. After the nucleation step, the nanobubble grows more slowly to nearly completely cover the Pt nanodisk, leading to a further decrease in current. The finding that the current for H^+ reduction does not completely vanish indicates that the Pt nanodisk is not completely covered by the nanobubble.

To test this hypothesis, we performed finite element simulations to obtain the concentration profile of electrochemically generated H_2 at the critical current i_{nb}^{p}. Assuming the system is at a steady state, the flux of H_2 ($\mathbf{J}_{out,H_2}$) away from the nanodisk should be equal to half of the electron transfer flux at the nanodisk electrode (the latter is equal to the influx of H^+ to the nanodisk electrode). The integral of the electron flux over the nanodisk surface is recorded as the critical current i_{nb}^{p}, eq 5.2, and $\mathbf{J}_{out,H_2}$ is governed by Fick's first law (eq 5.3). Finite element simulation using the Newton-Raphson method was employed to solve the following two equations from an appropriate initial guess. Details including mesh, geometry and boundary conditions are given in 5.5 Appendix.

$$i_{nb}^{p} = 2F \int \mathbf{J}_{out,H_2} \cdot \mathbf{n} \, ds \tag{5.2}$$

$$\mathbf{J}_{out,H_2} = -D_{H_2} \nabla C_{H_2} \tag{5.3}$$

Figure 5.4 shows the simulated H_2 distribution near a 27-nm-radius nanodisk electrode at the critical current i_{nb}^{p} of -21 nA. The concentration of H_2 near the electrode greatly exceeds the saturation concentration of H_2 at 1 atm and room temperature (~0.8 mM[39]). The black line corresponds to the 0.1 M H_2 contour line, within which the concentration of H_2 is sufficiently large to be in equilibrium (via Henry's law, eq 5.5) with a *20-nm-diameter* spherical nanobubble sitting on the electrode. More specifically, the Young-Laplace equation (eq 5.4) correlates the internal pressure of a nanobubble (p_{nb}) with its radius (r_{nb}) while Henry's law (eq 5.5) provides the equilibrium concentration ($C_{H_2}^{s}$) at the nanobubble/liquid interface at that pressure.

$$\Delta p = p_{nb} - p_{out} = \frac{2\gamma}{r_{nb}} \tag{5.4}$$

$$\Delta p = p_{nb} - p_{out} = kC_{H_2}^{s} \tag{5.5}$$

The Henry's law constant k = 1.43 atm/mM is taken from the experimental results from Wiebe *et al.*[40] γ is the surface tension of the sulfuric acid solution (0.073 N/m) [41] and p_{out} is the pressure of the bulk solution. Thus, for a 20-nm-diameter spherical nanobubble, the inner pressure, $p_{nb,}$ is calculated to be ~144 atm and $C_{H_2}^{s}$ is calculated to ~0.10 M.

After nucleation of a nanobubble, the nanobubble grows and is pinned at the circumference between the Pt and glass due to the difference in hydrophobicity of these two materials. As demonstrated below, the observation that the residual current is as low as a few hundred pA suggests that the H_2 nanobubble covers the majority of the active

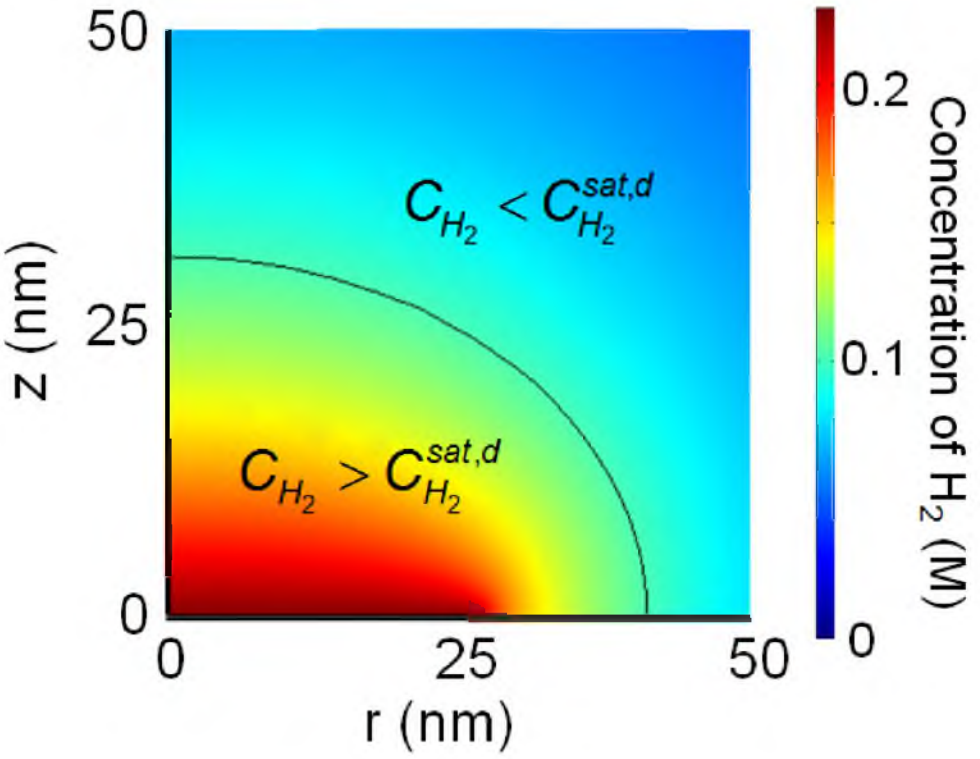

Figure 5.4. Simulated H_2 distribution (surface) near a 27-nm-radius Pt nanodisk at the experimentally measured critical current i_{nb}^{p} of -21 nA. The black line is the 0.1 M H_2 contour line, within which the concentration of H_2 (C_{H_2}) is higher than the saturation concentration $C_{H_2}^{sat,d}$ (~0.10 M, see text) required to form a spherical nanobubble with a diameter of 20 nm.

electrode surface. A clean Pt surface has been reported by Woods *et al.* to be hydrophilic in sulphate media (Na_2SO_4) at all potentials between hydrogen and oxygen evolution.[42] However, the hydrophilicity of Pt is sensitive to surface crystallography [43] and absorbed molecules.[44] In the absence of extensive cleaning, contact angles on Pt electrodes generally indicate a hydrophobic surface.[44]

In summary, we believe that the nucleation and formation of a nanobubble occurs when the H_2 generated by reduction of H^+ exceeds a saturation H_2 concentration that corresponds to a bubble of size equal to the dimension of the nanodisk electrode. This is also supported by the finding that i_{nb}^p ~-10 nA at a 11-nm-radius electrode, corresponding to a H_2 concentration of ~0.27 M at the electrode surface, is sufficiently high to form a *10-nm-diameter* spherical nanobubble.

5.3.3 Concentration dependence

According to the above-proposed mechanism, nanobubble formation occurs from a supersaturation of H_2 when the current reaches sufficiently large current, i_{nb}^p. Since the maximum available current at a nanoelectrode in the absence of the nanobubble formation is limited by the diffusive flux of protons, we further tested our proposed mechanism by varying the H_2SO_4 concentration and, thus, the maximum available current, eq 5.1.

Figure 5.5 shows the cyclic voltammetric responses at a 27-nm-radius Pt nanodisk as a function of H_2SO_4 concentration: (a) 0.01 to 0.05 M and (b) 0.1 to 0.5 M. The shape of the *i-V* response transforms gradually from sigmoidal-shaped wave to a peak-shape response as the concentration is increased from 0.01 to 0.5 M. A mixture of sigmoidal

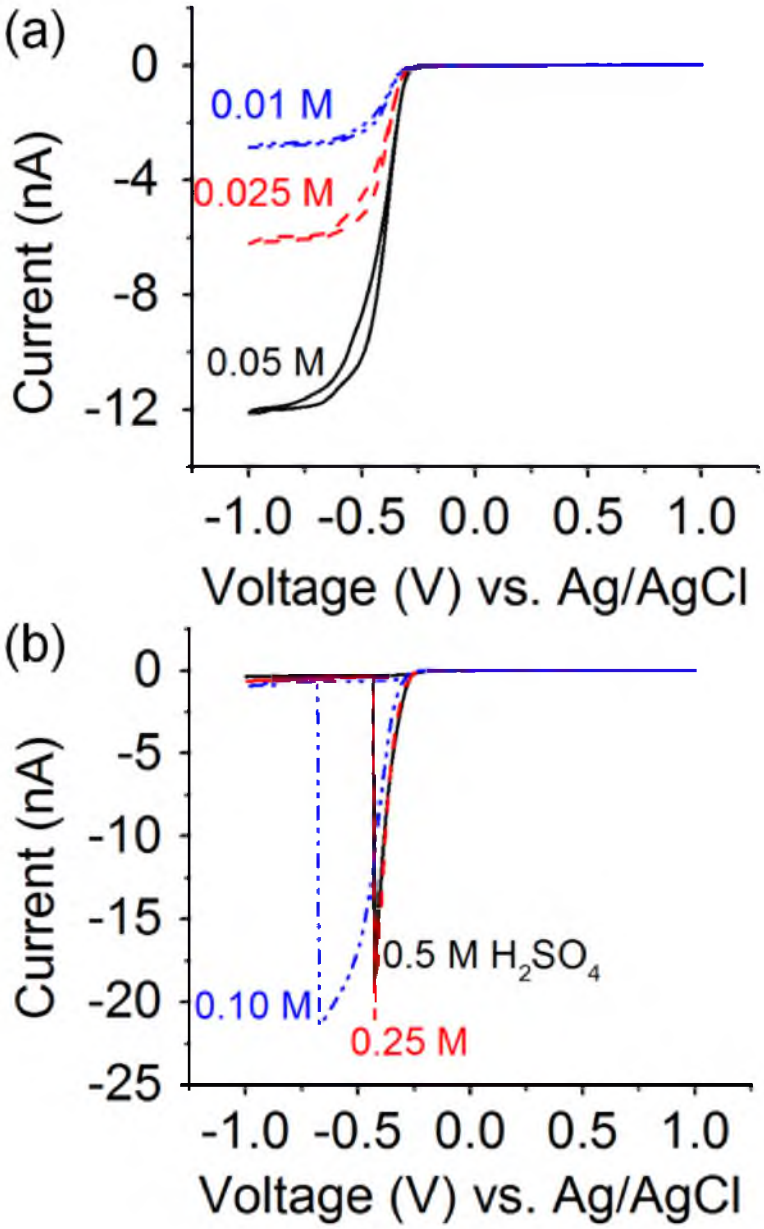

Figure 5.5. Cyclic voltammetric response at a 27-nm-radius Pt nanodisk as a function of H_2SO_4 solution concentration: (a) 0.01 to 0.05 M and (b) 0.1 to 0.5 M. Scan rate = 100 mV/s. The drop in current due to single nanobubble formation occurs in solutions containing greater than ~0.1 M H_2SO_4.

and peak features is present at 0.1 M, where the theoretical proton-diffusion-limited current is ~-19.4 nA, slightly smaller than the critical current i_{nb}^{p} of ~-21 nA. When the H_2SO_4 concentration is greater than ~0.1 M, a peak shape response with a *concentration-independent* i_{nb}^{p} is observed, indicating a critical concentration profile. In contrast, for H_2SO_4 concentrations < 0.1 M, the conventional diffusion-limited sigmoidal response at a nanodisk electrode was observed due to the failure to achieve the supersaturation of H_2. Similar behavior is observed at an 11-nm-radius Pt nanodisk electrode, see 5.5 Appendix.

5.3.4 Size dependence

Figure 5.6 shows the cyclic voltammetric response as a function of Pt nanodisk radius in a 0.5 M H_2SO_4. For nanodisks with radii < 50 nm, a peak shape voltammetric response is observed similar to that detailed above, while for radii > 50 nm the voltammetric response is sigmoidal shaped with a significant hysteresis on the forward and reverse scans. The maximum current of the sigmoidal-like response is close to the diffusion-limited current. For example, a 226-nm-radius nanodisk yielded a maximum current of -770 nA, in good agreement with the calculated proton-diffusion-limited current of -810 nA (eq 5.1). Using a similar finite element simulation method as described above, the concentration profile of H_2 for the 226 nm radius nanodisk at the maximum current was computed (5.5 Appendix). The resulting profile shows that the H_2 concentration near the surface is as high as 0.6 - 0.8 M and, according to Henry's law (eq 5.5) and the Young-Laplace equation (eq 5.4), such a concentration is able to support formation of spherical bubbles with radii between 1 and 2 nm. The possible explanation for not seeing a drop of current is that the nanobubbles are too small to significantly

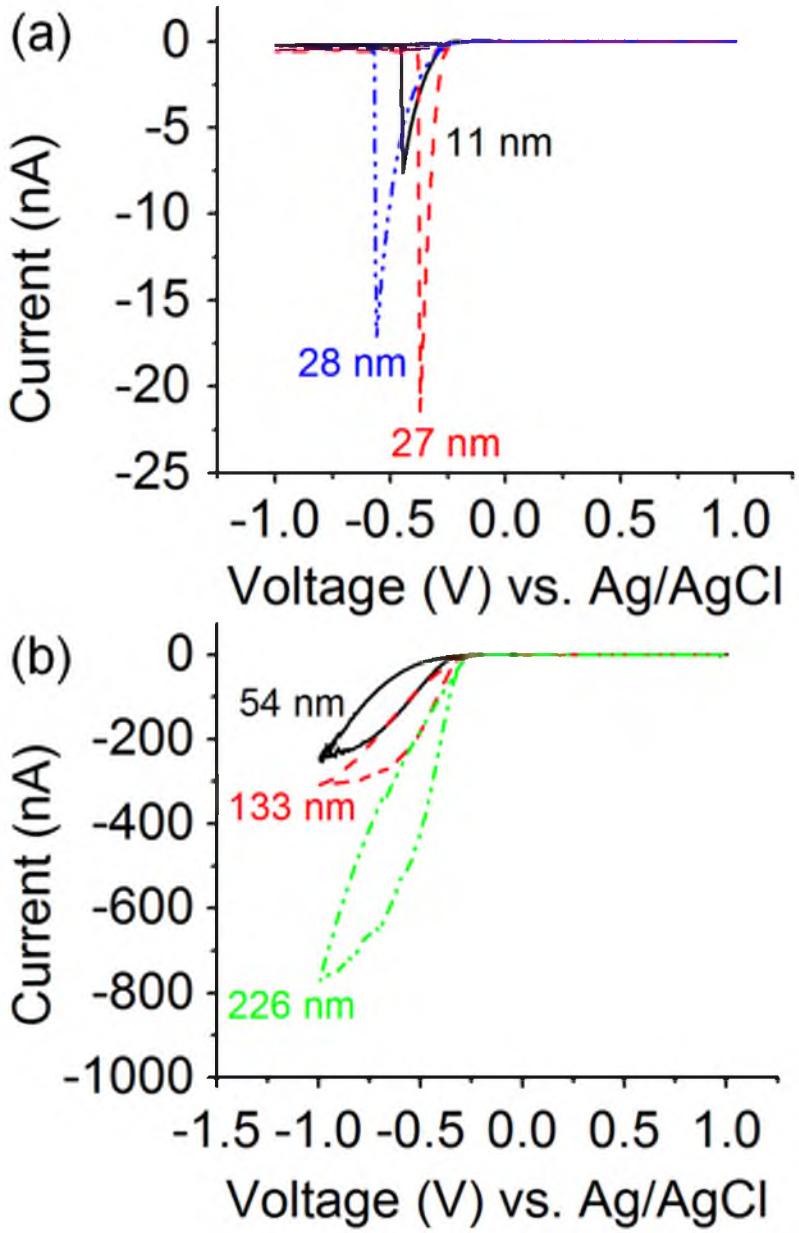

Figure 5.6. Cyclic voltammetric response as a function of the radius of the Pt nanodisk in a 0.5 M H_2SO_4 solution. Scan rate = 100 mV/s. Nanodisk radii are (a) from 11 to 28 nm and (b) from 54 to 226 nm.

interfere with the faradic current. However, continuous formation of such small nanobubbles, which may coalesce and reduce the active electrode surface area, causes the hysteresis in the forward and reverse voltammetric scans at larger electrodes. Based on the present results, it is impossible to determine the size of nanobubbles formed at the larger Pt nanodisks (> 50 nm) that exhibit the sigmoidal response. However, the voltammetric responses clearly indicate that nanobubbles are not large enough to cover the whole electrode surface.

5.3.5 Residual current i_{nb}

After the formation of a nanobubble at the Pt nanodisk electrode, the current decreases to a residual current, i_{nb}, Figure 5.2a. We believe this current, corresponding to the generation of H_2, is required to balance the diffusive outflux of H_2 through the nanobubble/liquid interface, resulting in a stable nanobubble**.** At steady state, the diffusive flux of H_2 ($\mathbf{J}_{H_2,d}$) through the nanobubble/liquid interface can be estimated using Fick's first law (eq 5.6). To simplify the calculation, the nanobubble at the electrode is assumed hemispherical and $\mathbf{J}_{H_2,d}$ is written as

$$\mathbf{J}_{H_2,d} = -D_{H_2}\frac{dC}{dx} = -D_{H_2}\frac{C^*_{H_2} - C^s_{H_2}}{r_{nb}} \tag{5.6}$$

where D_{H_2} is the diffusion coefficient of H_2 (4.5×10^{-5} cm^2/s[45]), $C^*_{H_2}$ and $C^s_{H_2}$ are the H_2 concentrations of the bulk solution and at the nanobubble/liquid interface, respectively. r_{nb} is the radius of the nanobubble, which we assume is the same as the Pt

nanodisk radius (27 nm) for reasons outlined above. $C^{s}_{H_2}$ is estimated to be ~0.037 M from the nanobubble radius r_{nb} using Henry's Law (eq 5.5) combined with the Young-Laplace equation (eq 5.4) and $\mathbf{J}_{H_2,d}$ is ~6.2 mol/(m^2•s). Hence, the integral of $\mathbf{J}_{H_2,d}$ over the hemispherical interface is ~2.82 × 10^{-14} mol/s, requiring a faradic current of ~-5.4 nA, which is ~10 fold larger than the measured residual current i_{nb} of -450 pA. The discrepancy may result from the variation of the nanobubble shape; for example, a flatter nanobubble with a larger radius of curvature has a significantly reduced inner pressure p_{nb} and, thus, a lower $C^{s}_{H_2}$ at the interface along with a reduced interfacial area. The lower $C^{s}_{H_2}$ and bubble surface area would result in a decrease of the total diffusive flux $\mathbf{J}_{H_2,d}$ and, correspondingly, a smaller faradic residual current i_{nb}. (Note: based on AFM images,[14] nanobubbles at the interface are typically flat instead of hemispheric both on hydrophobic and hydrophilic.) Using a similar calculation, a residual current of ~-367 pA is calculated to be required to support a flat nanobubble with a curvature of 135 nm radius which fully covers the 27-nm-radius nanodisk electrode. Additionally, Lohse *et al.*[18, 46] proposed the cycling of the diffusive outflux of H_2 back to the nanobubble due to the gas attraction by the solid surface. This cycling mechanism would potentially reduce i_{nb}.

The residual current i_{nb} is provided by the electrochemical reduction of H^+. Finite element simulation was employed to investigate the transport of protons to the fraction of Pt electrode surface not covered by the nanobubble. For simplicity, we again assume that a hemispherical nanobubble of radius r_{nb} covers the electrode leaving just a thin ring of Pt with width of (a - r_{nb}) exposed at the circumference of nanodisk electrode. Figure 5.7a and b illustrate a hemispherical nanobubble on a 27-nm-radius Pt nanodisk at steady state,

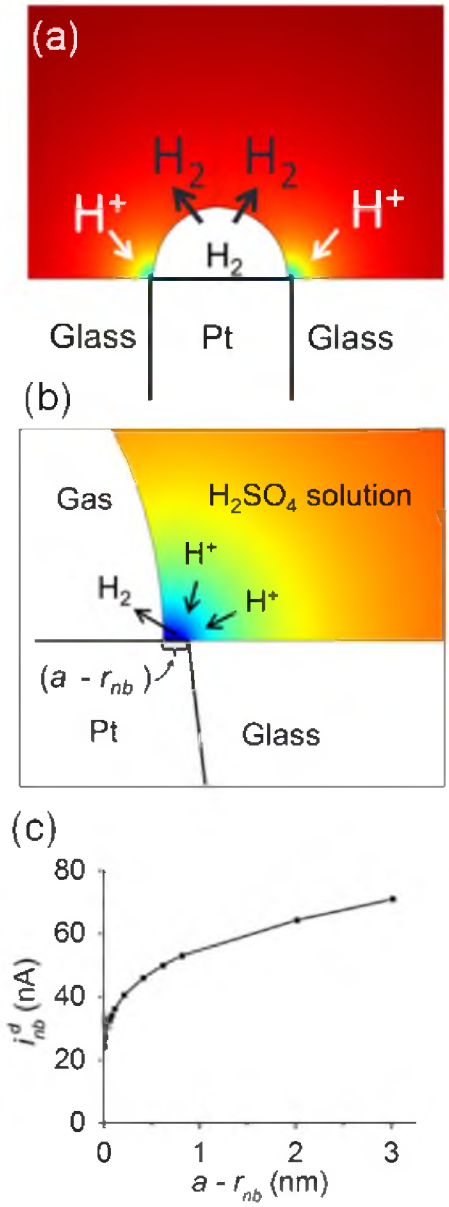

Figure 5.7. Simulation of diffusion limited proton transfer near a nanobubble. (a) Schematic illustration of a hemispherical nanobubble at a 27-nm-radius Pt nanodisk, and the dissolution of H_2 gas into the solution balanced by the electroreduction of H^+ at the circumference of the nanobubble. The colored surface shows the distribution of H^+ at the diffusion-limited condition where the H^+ concentration is driven to zero at the Pt surface (in accordance with the Nernst equation at potentials more negative than E° for H^+/H_2 redox couple; dark red corresponds to 1 M H^+ far from the electrode surface). (b) Expanded illustration showing the 3-phase Pt/gas/solution boundary. (c) Simulated H^+ diffusion-limited current i_{nb}^d as a function of the width of uncovered Pt surface in part (b). a is the radius of the nanodisk and r_{nb} is the radius of the semispherical nanobubble. H^+ reduction occurs at the circumference of the Pt nanoelectrode on the exposed region of Pt defined by a ring of width ($a - r_{nb}$).

where the H^+ diffuses to the Pt ring and is reduced to H_2 which enters the nanobubble at the Pt/gas/solution interface. This influx of H_2 is balanced by the outflux of H_2 at the nanobubble/liquid interface. The proton-diffusion-limited current i_{nb}^d is computed from the overall diffusive flux of H^+ to exposed area on the nanodisk where the H^+ concentration is set to 0 M. Figure 5.7c shows the relation between the simulated proton-diffusion-limited current i_{nb}^d and $(a - r_{nb})$. Generally, i_{nb}^d decreases as the uncovered Pt ring width decreases due to a reduced electrode surface. However, for ring thickness as small as 10 pm, approximately 6% of the size of a single Pt atom (= 175 pm[47]), the diffusion-limited current is still 24 nA, ~50 fold higher than the experimental value or ~5 fold higher than the required current estimated to balance the diffusive outflux of H_2. Therefore, it is unlikely that diffusion of H^+ is the rate-limiting step in determining i_{nb}. Given that the diffusive flux is so large to the ring electrode, it is more likely that the current is instead limited by the adsorption and electron-transfer steps associated with H^+ reduction. It has also been reported that the current at nanoband electrodes < 5 nm in width is limited by geometrical constraints associated with the comparable size of the redox species relative and the electrode.[48, 49] Thus, we arrive at the conclusion that while a steady-state residual current for H^+ reduction is essential to maintain the nanobubble, the rate of this electrochemical reaction is limited by the adsorption and electron-transfer kinetics instead of the diffusion of the reactant (H^+).

5.4 Conclusion

This preliminary study demonstrates that the electrochemical reduction of protons in sulfuric acid solutions, using Pt electrodes of radius less than ~50 nm, results in the

formation of a single H_2 nanobubble. These individual nanobubbles are indefinitely stable as long as the electrode potential is poised sufficiently negative of the thermodynamic potential of H^+ reduction, necessary to balance H_2 dissolution from the nanobubble by H_2 electrogeneration at the Pt/gas/solution interface. While electrochemical methods using Pt nanodisk electrodes appear to provide a powerful method to study individual nanobubbles, these studies raise numerous questions about the shape of the nanobubble, the relationship between the local H_2 distribution and bubble nucleation, and the role of the electrode surface properties, as well as role of the electrode/glass interface. Preliminary studies in our laboratory indicate that individual O_2 nanobubbles can also be formed at the Pt nanodisks through the electro-oxidation of water, although this process is more complicated due to the sluggish kinetics of water oxidation. We are currently pursuing imaging of individual nanobubbles under electrochemical control, as well as using significantly faster electrochemical instrumentation to study the dynamics of bubble nucleation. These studies will be the focus of future reports.

5.5 Appendix

In this appendix, the characterization of Pt nanodisk electrodes, cyclic voltammetric responses of an 11-nm-radius nanodisk electrode as a function of scan rate and H_2SO_4 concentration, the conditions in finite element simulation of H_2 profile at the critical current i_{nb}^{p}, and simulated H_2 concentration profile for a 226-nm-radius nanodisk electrode at i_{nb}^{p} are given in Figure 5.8 to Figure 5.12.

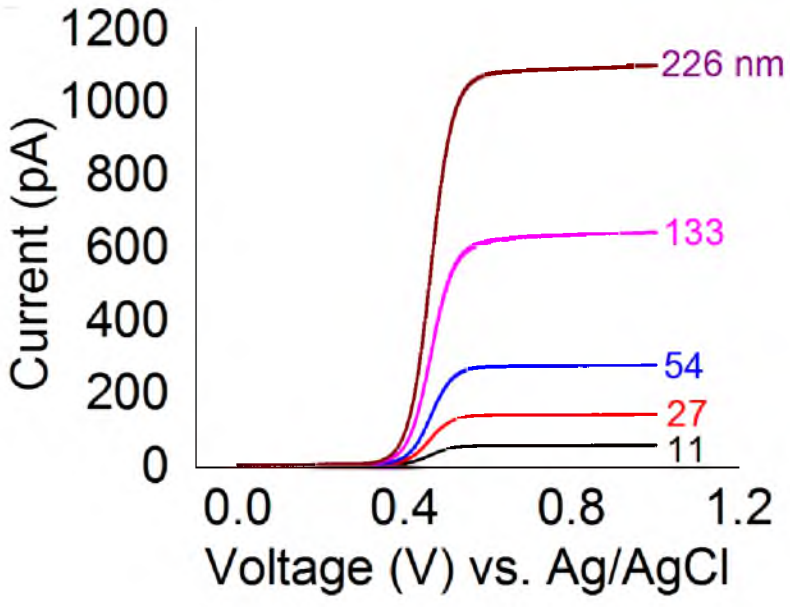

Figure 5.8. The steady-state voltammetric response of Pt nanodisk electrodes with various radii immersed in a 5.0 mM ferrocene (Fc) in acetonitrile (supporting electrolyte 0.1 M $TBAPF_6$; scan rate = 10 mV/s). The electrode radii, a, were calculated from the limiting current, i_{lim}, using the expression $i_{lim} = 4nFDC^*a$, where D and C^* are the diffusivity and bulk concentration of Fc and $n = 1$. The curves show the forward and reverse scans. See main text for other details.

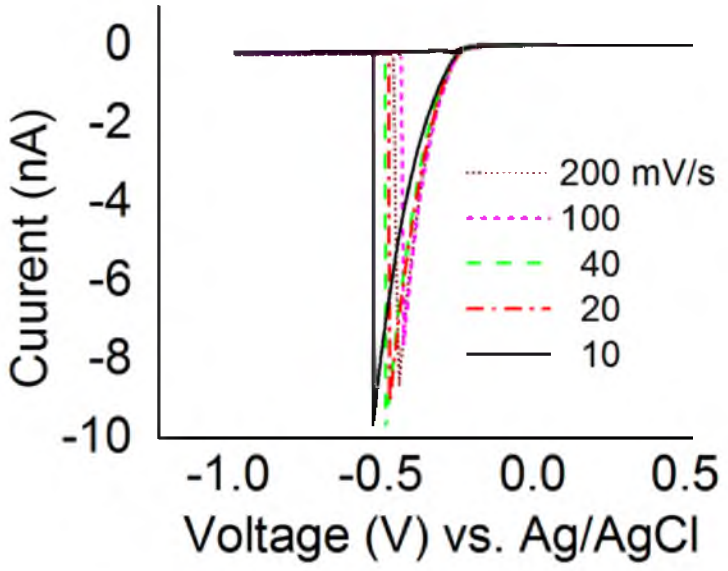

Figure 5.9. Cyclic voltammetric response for an 11-nm-radius Pt nanodisk in a 0.5 M H_2SO_4 solution recorded at scan rates between 10 and 200 mV/s.

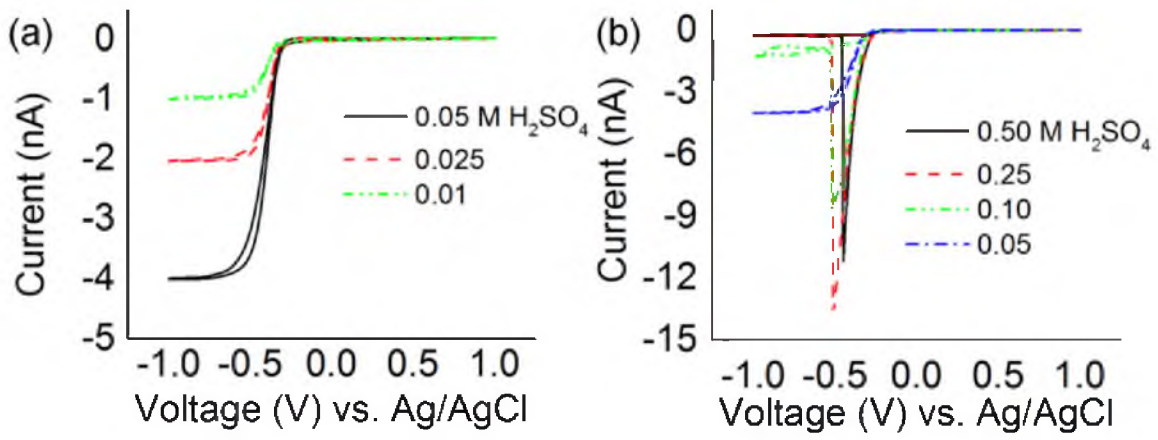

Figure 5.10. Cyclic voltammetric response at an 11-nm-radius Pt nanodisk as a function of H_2SO_4 solution concentration: (a) 0.01 to 0.05 M and (b) 0.1 to 0.5 M. Scan rate = 100 mV/s.

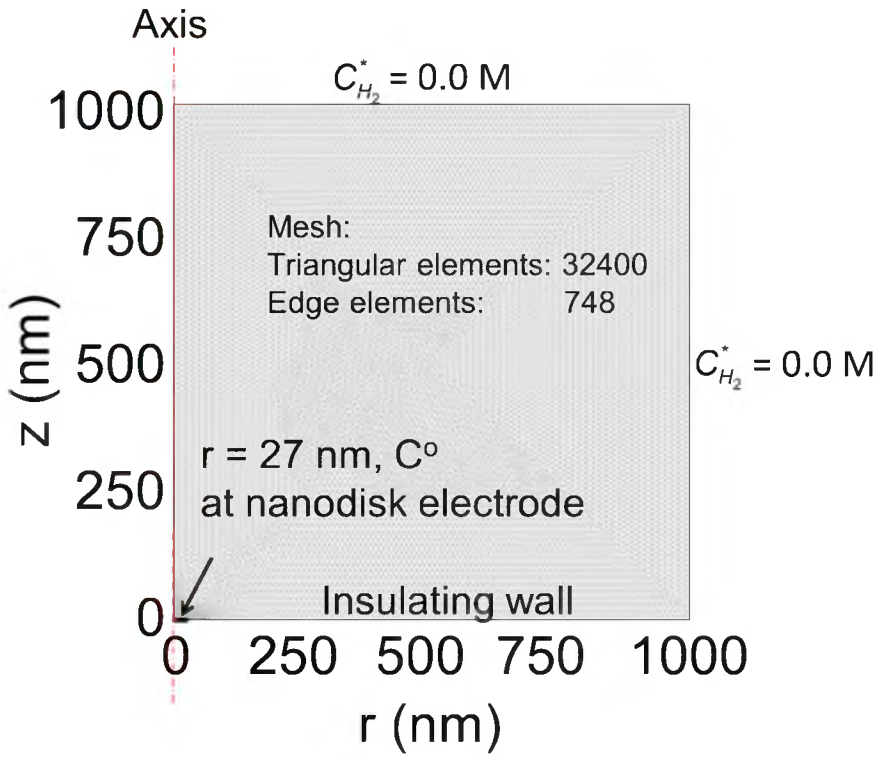

Figure 5.11. The 2D axial-symmetric geometry of the nanodisk electrode embedded in glass and the mesh for the finite-element simulation (red dash line: the symmetry axis).

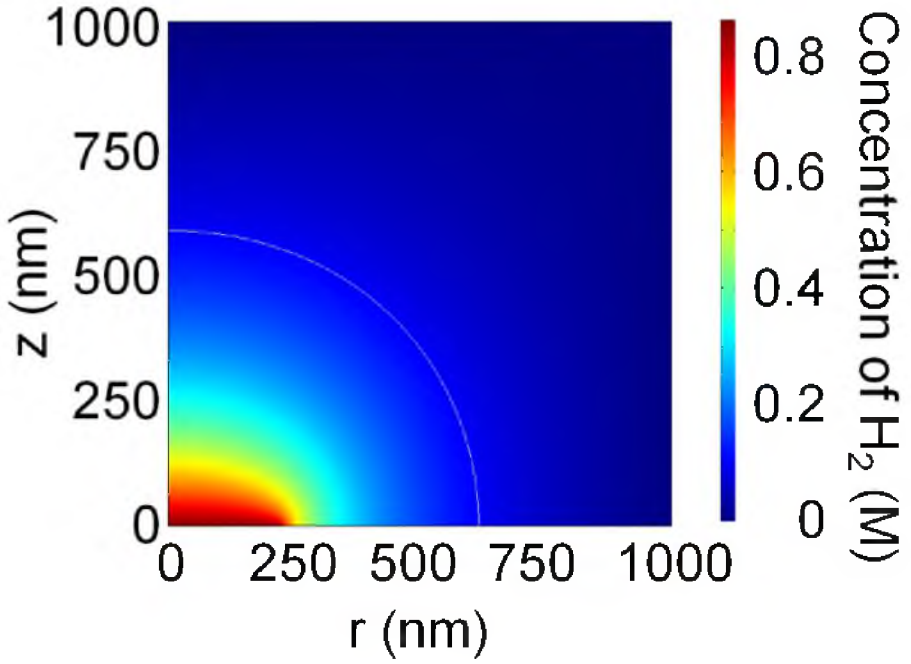

Figure 5.12. Simulated H_2 distribution near a 226-nm-radius Pt nanodisk at the experimental critical current i_{nb}^{p} of 770 nA. The white line is the 0.1 M H_2 contour line, within which the concentration of H_2 is greater than the saturation concentration (0.102 M) to form a spherical nanobubble with a diameter of 20 nm. See main text for discussions of the H_2 saturation concentration and simulation.

5.6 References

(1) Zhang, L. J.; Zhang, Y.; Zhang, X. H.; Li, Z. X.; Shen, G. X.; Ye, M.; Fan, C. H.; Fang; H. P.; Hu, J. *Langmuir* **2006**, *22*, 8109-8113.

(2) Liu, G. M.; Wu, Z. H.; Craig, V. S. J. *J. Phys. Chem. C*, **2008**, *112*, 16748-16753.

(3) Yang, S. J.; Tsai, P. C.; Kooij, E. S.; Prosperetti, A.; Zandvliet, H. J. W.; Lohse, D. L*angmuir*, **2013**, *29* , 5937–5937.

(4) Yang, S. J.; Tsai, P. C.; Kooij, E. S.; Prosperetti, A.; Zandvliet, H. J. W.; Lohse, D. *Langmuir* **2009**, *25*, 1466-1474.

(5) Lou, S. T.; Ouyang, Z. Q.; Zhang, Y.; Li, X. J.; Hu, J.; Li M. Q.; Yang, F. J. *J. Vac. Sci. Technol., B*, **2000**, *18*, 2573-2575.

(6) Lou, S. T.; Gao, J. X.; Xiao, X. D.; Li, X. J.; Li, G. L.; Zhang, Y.; Li, M. Q.; Sun, J. L.; Li,X. H.; Hu, J. *Mater. Charact.*, **2002**, *48*, 211-214.

(7) Yang, J. W.; Duan, J. M.; Fornasiero. D.; Ralston, J. *J. Phys. Chem. B*, **2003**, *107*, 6139-6147.

(8) Zhang, X. H.; Maeda, N.; Craig, V. S. J. *Langmuir*, **2006**, *22*, 5025-5035.

(9) Switkes, M.; Ruberti, J. W. *Appl. Phys. Lett.*, **2004**, *84*, 4759-4761.

(10) Zhang, J.; Yoon, R.-H.; Mao, M.; Ducker, W. A. *Langmuir*, **2005**, *21*, 5831-5841.

(11) Zhang, X. H.; Li, G.; Maeda, N.; Hu, J. *Langmuir*, **2006**, *22*, 9238-9243.

(12) Zhang, X. H.; Zhang, X. D.; Sun, J. L.; Zhang, Z. X.; Li, G.; Fang, H. P.; Xiao, X. D.; Zeng, X. C.; Hu, J. *Langmuir*, **2007**, *23*, 1778-1783.

(13) van Limbeek, M. A. J.; Seddon, J. R. T. *Langmuir* **2011**, 27, 8694-8699.

(14) Zhang, L.; Zhang, X.; Zhang, Y.; Hu, J.; Fang, H. *Soft Matter* **2010**, *6*, 4515-4519.

(15) Zhang, X. H.; Quinn, A.; Ducker, W. A. *Langmuir* **2008**, *24*, 4756−4764.

(16) Karpitschka,S.; Dietrich, E.; Seddon, J.R.T.; Zandvliet, H. J. W.;, Lohse, D.; Riegler, H.; *Phys. Rev. Lett.* **2012**, *109*, 066102.

(17) Zhang, X.; Chan, D. Y. C.; Wang, D.; Maeda, N. *Langmuir* **2013**, 29, 1017-1023.

(18) Brenner, M. P.; Lohse, D. *Phys. Rev. Lett.* **2008**, *101*, 214505.

(19) Ducker, W. A. *Langmuir* **2009**, *25*, 8907- 8910.

(20) Weijs, J. H.; Lohse, D. *Phys. Rev. Lett.* **2013**,*110*, 054501.

(21) Liu, Y.; Zhang, X. *J. Chem. Phys.* **2013**, *138*, 014706.

(22) Ljunggren, S.; Eriksson, J. C. *Colloids Surf A* **1997**, *130*, 151-155.

(23) Das, S. *Phys. Rev. E* **2011**, *83*, 066315.

(24) Das, S.; Snoeijer, J. H.; Lohse, D. *Phys. Rev. E* **2010**, 82, 056310.

(25) Craig, V. S. J. *Soft Matter* **2011**, *7*, 40-48.

(26) Zhang, X. *Phys. Chem. Chem. Phys.* **2008**, *10*, 6842–6848.

(27) Seddon, J. R. T.; Kooij, E. S.; Poelsema, B.; Zandvliet, H. J. W.; Lohse, D. *Phys. Rev. Lett.* **2011**, *106*, 056101.

(28) Guan, M.; Guo, W.; Gao, L.; Tang, Y.; Hu, J.; Dong, Y. *ChemPhysChem* **2012**,*13*, 2115–2118.

(29) Xiao, X.; Bard, A. J. *J. Am. Chem. Soc.* **2007**, *129*, 9610- 9612.

(30) Xiao, X.; Fan, F.-R. F.; Zhou, J.; Bard, A. J. *J. Am. Chem. Soc.* **2008**, *130*, 16669-16677.

(31) Kwon, S. J.; Fan, F.-R. F.; Bard, A. J. *J. Am. Chem. Soc.* **2010**, *132*, 13165-13167.

(32) Zhou, H.; Fan, F.-R. F.; Bard, A. J. *J. Phys. Chem. Lett.* **2010**, *1*, 2671-2674.

(33) Zhang, B.; Galusha, J.; Shiozama, P. G.; Wang, G.; Bergren, A. J.; Jones, R. M.; White, R. J.; Ervin, E. N.; Cauley, C. C.; White, H. S. *Anal. Chem.* **2007**, *79*, 4778-4787.

(34) Zhan, D.; Velmurugan, J.; Mirkin, M. V. *J. Am. Chem. Soc.* **2009**, *131*, 14756-14760.

(35) Li, Y. X.; Cox, J. T.; Zhang, B. *J. Am. Chem. Soc.* **2010**, *132*, 3047-3054.

(36) Cussler, E. L. *Diffusion: Mass Transfer in Fluid Systems* (2nd ed.); Cambridge University Press: New York, **1997**.

(37) Murray, R. W. *Chem. Rev.* **2008**, *108*, 2688-2720.

(38) Cox, J. T.; Zhang, B. *Annu. Rev. Anal. Chem.* **2012**, *5*, 253-272.

(39) Proch, S.; Wirth, M.; White, H. S. ; Anderson, S. L. *J. Am. Chem. Soc.*, **2013**, *135*, 3073–3086.

(40) Wiebe, R.; Gaddy, V. L.; Heins, C. *Ind. Eng. Chem.*, **1932**, *24* , 823-825.

(41) Suggitt, R. M.; Aziz, P. M.; Wetmore, F. E. W. *J. Am. Chem. Soc.* **1949**, *71*, 676–678.

(42) Gardner, J.R.; Woods, R. *J. Electroanal. Chem.* **1977**, *81,* 285–290.

(43) van der Niet, M. J. T. C.; den Dunnen, A.; Koper, M. T. M.; Juurlink, L. B. F. *Phys. Rev. Lett.* **2011**, *107*, 146103.

(44) van Der Niet, M. J. T. ; Dunnen, C. A. Den ; Juurlink, L. B. F. ; Koper, M. T. M. *Angew. Chem.* **2010**, *122*, 6722-6725.

(45) Mazarei, A.F.; Sandall, O.C. *AIChE J.* **1980**, *26*, 154-157.

(46) Seddon, J. R. T.; Zandvliet, H. J. W.; Lohse, D. *Phys. Rev. Lett.* **2011**, *107*, 116101.

(47) Bondi, A. *J. Phys. Chem.* **1964**, *68*, 441-451.

(48) Morris, R. B., Franta, D. J., White, H. S. *J. Phys. Chem.* **1987**, *91*, 3559-3564.

(49) Seibold, J. D., Scott, E. R., White, H. S. *J. Electroanal. Chem. Interfacial Electrochem.* **1989**, *264*, 281-289.